Femtosecond single-electron diffraction

Stefan Lahme

München 2014

Femtosecond single-electron diffraction

Stefan Lahme

Dissertation
an der Fakultät für Physik
der Ludwig–Maximilians–Universität
München

vorgelegt von
Stefan Lahme
aus Brilon

München, den 19.09.2014

Erstgutachter: Prof. Dr. Ferenc Krausz
Zweitgutachter: Prof. Dr. Peter Hommelhoff
Tag der mündlichen Prüfung: 12.12.2014

Zusammenfassung

Die grundlegenden Funktionsprinzipien der Natur zu verstehen, ist seit jeher Antrieb der Naturwissenschaften. Verhalten und Eigenschaften von Festkörpern werden dabei häufig von dynamischen Prozessen auf atomarer Skala ($< 10^{-10}\,\mathrm{m}$) bestimmt, welche typischerweise auf Zeitskalen im Bereich von zehn Femtosekunden ($10^{-15}\,\mathrm{s}$) bis hin zu vielen Picosekunden ($10^{-12}\,\mathrm{s}$) ablaufen. Zeitaufgelöste Elektronenbeugung an kristallinen Festkörpern ermöglicht die direkte Beobachtung solcher Prozesse in Raum und Zeit. Die bislang mit diesem Verfahren erreichte Zeitauflösung von etwa 100 fs eignet sich jedoch nicht zur Beobachtung der schnellsten Prozesse in Festkörpern. Auch die, zur zuverlässigen Auflösung von großen Elementarzellen molekularer Kristalle erforderliche, transversale Kohärenz ist unzureichend. Eine wesentliche Ursache für diese beiden Probleme liegt in der gegenseitigen Coulomb-Abstoßung der Elektronen innerhalb eines Pulses und den daraus resultierenden Veränderungen der Geschwindigkeitsverteilungen in radialer und longitudinaler Richtung. Während erstere zu verringerter transversaler Kohärenz führt, hat letztere längere Elektronenpulsdauern und damit eine begrenzte Zeitauflösung zur Folge.

In dieser Arbeit wird ein Messaufbau zur zeitaufgelösten Elektronenbeugung vorgestellt, welcher auf der Erzeugung von nur einem Elektron pro Puls basiert. Aufgrund der Vermeidung von Coulomb-Abstoßung innerhalb der Pulse ist dieser Ansatz eine vielversprechende Basis zur konzeptionell nahezu unbegrenzten Verbesserung der Zeitauflösung. Eine hier eigens entwickelte, thermisch stabilisierte Elektronenquelle garantiert einen hohen Grad an Kohärenz bei gleichzeitig hervorragender Langzeitstabilität der Photoelektronenausbeute. Insbesondere letzteres ist für zeitaufgelöste Beugungsexperimente mit Einzeleelektronen aufgrund der längeren Integrationszeit unerlässlich, konnte jedoch durch vorhergehende Quellen nicht erreicht werden. Darüber hinaus werden in dieser Arbeit die besonderen Ansprüche der Einzelelektronenbeugung an die zu untersuchenden Materialien diskutiert und Strategien zur Vermeidung von Schäden an der Probe durch akkumulierte Anregungsenergie entwickelt. Diese erfordern neue Schwerpunkte bei der Probenpräparation, welche entwickelt und diskutiert werden. Die Beobachtung der komplexen Relaxationsdynamik in Graphit-Dünnfilmen mit zeitaufgelöster Einzelelektronenbeugung demonstriert abschließend die generelle Eignung dieses Verfahrens als zuverlässige Methodik zur Untersuchung von reversibler, struktureller Dynamik in Festkörpern mit atomarer Auflösung.

Nicht-relativistische Einzelelektronenpulse können mit Hilfe von zeitabhängigen Feldern bei Mikrowellenfrequenzen bis in den 10 fs-Bereich komprimiert werden, eventuell sogar bis in den Attosekundenbereich. Die hier demonstrierte langzeitstabile und hochkohärente

Elektronenquelle, sowie die Methodiken zur Probenpräparation und zeitaufgelösten Beugung mit Einzelelektronenpulsen liefern die Basis für zukünftige Experimente dieser Art.

Abstract

The understanding of nature's fundamental processes has always been the goal of science. Often, the behavior and properties of condensed matter are determined by dynamic processes on the atomic scale ($< 10^{-10}\,\mathrm{m}$). The relevant time scales for these processes range from tens of femtoseconds ($10^{-15}\,\mathrm{s}$) to several picoseconds ($10^{-12}\,\mathrm{s}$). Time-resolved electron diffraction on crystalline solids allows the direct observation of such processes in space and time. However, the state-of-the-art temporal resolution is insufficient to observe the fastest processes in solids. The transverse coherence is insufficient to resolve large unit cells of molecular crystals. One major origin for both of these problems is that the electron within the pulse repel each other, resulting in a change of the radial and longitudinal velocity distribution. The former leads to a decrease transverse coherence while the former leads to a significant increase in electron pulse duration, limiting temporal resolution.

In this work, a setup for time-resolved electron diffraction is introduced that works with electron pulses each containing only a single electron. Circumventing Coulomb repulsion, this approach can lead to in principle nearly unlimited, improvement of temporal resolution. The novel, thermally stabilized single-electron gun developed here provides a high degree of transverse coherence and excellent long-term stability of the photoemission yield at the same time. The latter is crucial for time-resolved diffraction experiments due to the long integration times required when working with single-electron pulses and has not been achieved prior to this work. Furthermore, the special requirements of single-electron diffraction on the materials under study are discussed. Strategies for avoidance of sample damage from accumulated excitation energy are developed, requiring new emphases in sample preparation. The observation of the complex relaxation dynamics of graphite thin films using time-resolved single-electron diffraction finally demonstrates the general feasibility of this technique as a reliable methodology for investigation of reversible, structural dynamics in solids with atomic resolution.

Using time-dependent fields at microwave frequencies, non-relativistic single-electron pulses can be compressed to 10 fs and possibly even down to the attosecond regime. The long-term stable and high-coherence electron gun demonstrated here as well as the methodology developed for sample preparation and time-resolved electron diffraction using single-electron pulses provide the basis for such experiments in the future.

Contents

List of Figures

List of scientific publications

S. Lahme, C. Kealhofer, F. Krausz, and P. Baum. "Femtosecond single-electron diffraction". *Structural Dynamics* 1.3 (2014)

F. O. Kirchner, S. Lahme, F. Krausz, and P. Baum. "Coherence of femtosecond single electrons exceeds biomolecular dimensions". *New Journal of Physics* 15 (2013)

F. O. Kirchner, A. Gliserin, F. Krausz, and P. Baum. "Laser streaking of free electrons at 25 keV". *Nature Photonics* 8.1 (2014), pp. 52–57

C. Effertz, S. Lahme, P. Schulz, I. Segger, M. Wuttig, A. Classen, and C. Bolm. "Design of Novel Dielectric Surface Modifications for Perylene Thin-Film Transistors". *Advanced Functional Materials* 22.2 (2012), pp. 415–420

Chapter 1

Motivation

In the quest to understand the underlying mechanisms of nature, mankind has taken immense efforts to explore the inner structure of matter; from biological cells to molecules and atoms down to elementary particles. Beyond the mere structure of matter, it is also the dynamics of interactions and transitions which define its properties. A physical understanding of fundamental electronic, atomic and molecular processes is required as they determine and limit the functionality of our daily technology and biology. Conspicuous examples include the dynamics of photo-induced phase transformations in strongly correlated materials such as Mott-insulators [5, 6] and spin-Peierls materials [7, 8], the interplay between phonons and cooper pairs in high-temperature superconductors [9–11], charge-density waves [12–17], phonon-induced changes of electrical properties [18–20], molecular switches [21, 22], photo damage of DNA [23, 24] and the exploration of new functional materials such as [25, 26]. However, for a long time direct visualization of the nuclear motions underlying such processes was regarded as science fiction due to the relevant time and length scales of femtoseconds and picometers, respectively [27–31].

In general, the dynamics of any process can only be resolved if spatial and temporal resolution of the measuring device are sufficient to sample the process with sufficient signal-to-noise ratio and dynamic range. An oft-cited example is the series of time-delayed photographs called "Horse in Motion" from Eadweard J. Muybridge (1878) to determine whether a galloping horse can have all four feet off the ground. Modern high-speed photography easily achieves resolutions of 100 µm and 100 µs providing access to a variety of fast processes including animal motions [32] and complex mechanical dynamics [33]. Figure 1.1 shows an impressive example[1] of modern high-speed photography: A water droplet is falling on a man-made highly hydrophobic surface but the lotus effect prevents wetting and causes the reformation of the droplet (after Fig. 1.1c) ultimately bouncing of the surface again (Fig. 1.1f).

The requirements for visualizing atoms or electrons in motion are on a completely different scale. Promising approaches to reach picometer and femtosecond resolution simultaneously are time-resolved diffraction techniques using hard X-rays or electrons in

---

[1] Permission to reprint the images was kindly provided by Dr. Rudolf Diesel, ScienceMedia, Germany, `http://www.science-media.de` (Accessed: 9 June 2014).

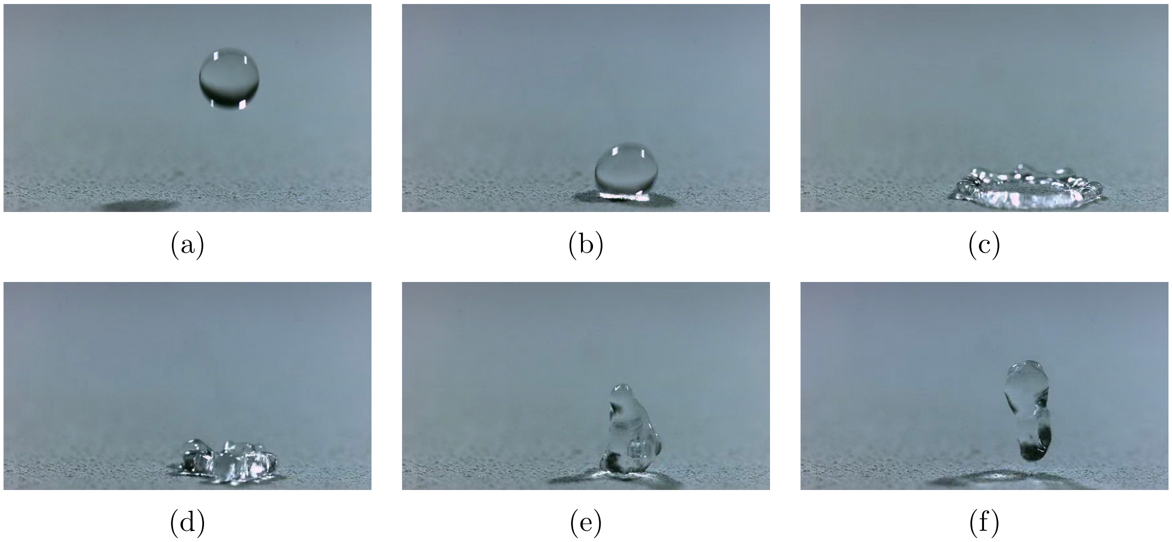
(a) (b) (c)

(d) (e) (f)

Figure 1.1: Lotus effect of water droplet falling onto a man-made, highly hydrophobic surface observed by Dr. Rudolf Diesel (ScienceMedia, Germany) using a high-speed camera. Time is increasing from (a) to (f) in arbitrary steps.

a pump-probe scheme. The desired dynamics are triggered with an optical ultrashort laser pulse (pump) and measured with a precisely delayed read out pulse (probe) which is diffracted at the sample, providing a diffraction snapshot of the process at the given time delay. With a sequence of such experiments at various time delays, the entire process then can be sampled.

In time-resolved X-ray diffraction, femtosecond temporal resolution was first demonstrated by Rischel et al. [34] in 1997 in an investigation of ultrafast heating of an organic film. During the ensuing period, the technique was for example successfully used to observe coherent acoustic pulse propagation [35], coherent phonons [36–38], laser induced strain [39], magnetic phase transitions [40], charge transfer processes in manganites [37] and molecular crystals [38].

One of the first ultrafast time-resolved electron diffraction (UED) experiments was performed by Williamson and Mourou [41, 42] in the early 1980's and investigated a phase transition in aluminum after laser excitation. Since then, the technique has been applied in different configurations. Studies in the gas phase enabled the determination of the structure of the transient C_2F_2I radical [43], and the reflection high-energy electron diffraction (RHEED) geometry [44] has proven to be very informative for studying photo-induced surface dynamics [15, 45, 46]. Femtosecond temporal resolution has been achieved in both reflection (RHEED) [5] and transmission (TEM) [47] geometries investigating a Mott-insulator transition and ultrafast melting, respectively. Further studies have successfully investigated coherent phonons [48, 49], phonon relaxation dynamics [50], ring-closing reaction [51], charge density waves [14, 52] and molecular motions in an organic salt [53], to cite some examples. Time-resolved electron microscopy has also been demonstrated, enabling the observation of dynamic processes in real space [28, 54].

Techniques based on x-ray diffraction and electron diffraction each have specific advantages and must be seen as more complementary than competing. Radiation damage from electrons, especially to organic samples, is a thousand times smaller per scattering event than for X-rays [55] and the total elastic scattering cross section is about 10^4–10^5 times higher [31]. The correspondingly nanoscale sample thicknesses in transmission electron diffraction [56] provide homogeneous pumping and inherently minimize temporal distortions caused by scattering from different parts of the sample. In contrast, X-rays require several hundred micrometer or even millimeter sized samples [56] which complicates data analysis [31] as it is necessary to deconvolve the effective sample volume and the inhomogeneous pumping profile. Ultrafast electron sources based on the well-known photoelectric effect are much simpler than synchrotron or laser plasma X-ray sources [31], and the shape of electron beams can be easily modified by applying electric and magnetic fields. However, preparation and mounting of free standing crystalline thin film samples required for UED is very challenging. Thermal damage from pumping occurs more easily as it is difficult to provide efficient heat sinks. Another major challenge working with electron probes is the limitation of temporal resolution due to pulse broadening mechanisms, such as dispersive broadening and space charge broadening. In state-of-the-art UED experiments, the latter is known to account for the lion's share and therefore is the most limiting factor for achievable electron pulse durations. Unfortunately the pulse durations reported in UED experiments so far are not sufficient for structural studies on the fastest atomic motions in solids—for example, anharmonic coupling of coherent optical phonons in graphite [19, 20], molecular dimerization in spin-Peierls materials [7], phase transitions in correlated electron materials with the perovskite structure [57], and collapse of charge-density waves [16, 17].

This work demonstrates the feasibility of an UED approach which inherently circumvents space charge broadening. The underlying physics of specific challenges emerging from this approach, such as sufficient but nondestructive sample excitation and electron yield stability, are investigated and appropriate solutions are developed. The results are promising for the realization of few-femtosecond or even attosecond temporal resolutions in UED with typical compression techniques and thereby pave the way to the observation of the fastest processes in condensed matter physics.

Chapter 2

General requirements for studying transient atomic motions

2.1 Spatial resolution

The spatial resolution required to observe transient dynamics is determined by the magnitude of change in atomic position caused by the dynamics of interest. Typical magnitudes can be estimated from the amplitudes of vibrational motions in crystals and thermal expansion. In the classical limit, the amplitude of a phonon is given as

$$u_0 = \sqrt{\frac{2E}{m\,\omega^2}} = \sqrt{\frac{2\hbar\,\tau}{\pi\,m}} \tag{2.1}$$

with $E = \hbar\omega$ the phonon energy per atom, $\omega = 2\pi/\tau$ the phonon frequency, m the reduced mass of the system, τ the phonon period and $\hbar$ the reduced Planck constant [50, 58]. Considering typical phonon periods ranging roughly from 10 fs to 1 ps (detailed estimation given in Section 2.3) and typical reduced masses in the range 5 u to 100 u, the lower limit for u_0 is approximately a few picometer. The same order of magnitude is derived for amplitudes of vibrational modes in small molecules [59] and coherent phonons in single-wall carbon nanotube [60]. With regard of typical lattice constants and bond lengths (1 Å to 10 Å [61]) this corresponds to a relative change in atomic position on the order of 10^{-2} to 10^{-3}.

2.1.1 Angular resolution

The change in diffraction angle is estimated for the aforementioned relative changes in lattice constant from Eq. (A.3) as

$$\Delta\theta \approx \frac{\lambda\,\delta}{\sqrt{4\,d_{hkl}^2 - \lambda^2}} \tag{2.2}$$

with λ the electron wavelength, d_{hkl} the lattice plane spacing and δ the relative change of d_{hkl}. As the incident angle of the electron beam does not change, $2\Delta\theta$ must be reliably resolved by the detection scheme to sufficiently track the dynamics.

Assuming a wavelength of roughly a tenth of the lattice spacing, $2\Delta\theta$ is estimated as roughly 0.005°. The spatial resolution of a detector placed at a distance of 1 m must be on the order of 10 µm.

2.1.2 Signal-to-noise

The intensity of a Bragg reflection depends on the crystal's basis described by the structure factor (see Eq. (A.5)) as well as on phonon dynamics described by the Debye-Waller effect (DWE, see Eq. (A.7)). Assuming a simple lattice with a two-atomic basis and considering the expected relative changes, few percent intensity changes can be calculated from Eqs. (A.4) and (A.5). Using Eq. (A.8), the mean square amplitude $\langle |u|^2 \rangle$ can be derived assuming the mentioned range for phonon frequencies. Taking into account typical reciprocal lattice vector lengths of $1\,\text{Å}^{-1}$ to $12\,\text{Å}^{-1}$, the DWE was calculated from Eq. (A.7) to be on the order of a few percent. Both estimations determine the the required resolution for intensity detection to approximately 1 %.

As described in Appendix A, electron diffraction patterns arise from elastic scattering events. The probability p for a single electron to be scattered elastically is given by

$$p = n\, d_s\, \sigma_\mathrm{e} \tag{2.3}$$

with n the number density of scatter centers, i.e. atoms, d_s the thickness of the sample and σ_e the total cross section for elastic scattering. The fraction p of the integrated number of incoming electrons N_in gives the total number of elastically scattered electrons which are distributed over all Bragg reflections M of a recorded diffraction pattern. The signal-to-noise ratio (SNR) of the intensity of a single Bragg reflection is defined as

$$SNR = \frac{\overline{N_B}}{\sigma_{N_B}} \tag{2.4}$$

with $\overline{N_B}$ the mean number of electrons in a Bragg spot and σ_{N_B} the standard deviation. Fundamentally, the standard deviation is limited by the shot noise σ_{SN} of the electrons,

$$\sigma_{SN} = \sqrt{\overline{N_B}}. \tag{2.5}$$

Assuming $\sigma_{N_B} = \sigma_{SN}$, the total number of incoming electrons required to achieve a given SNR in M Bragg spots can be determined from

$$N_\mathrm{in} = \frac{M\,\overline{N_B}}{p} \overset{(2.3)\ \text{to}\ (2.5)}{=} \frac{M}{n\, d_s\, \sigma_\mathrm{e}}\, SNR^2. \tag{2.6}$$

Equation (2.6) assumes equally illuminated Bragg spots, and therefore neglects intensity variations from diffraction order and the structure factor. Nevertheless, Eq. (2.6) is suitable for a rough estimation of N_in required for UED experiments.

A typical example might be diffraction of 100 keV electrons by a 20 nm aluminum thin film. The elastic scattering cross section is roughly $\sigma_\mathrm{e} \approx 10^{-22}\,\mathrm{m}^2$ [62, 63]. Assuming $M = 50$ observable Bragg reflections and requiring a SNR of 100, i.e. a resolution of 1 %, N_in is calculated from Eq. (2.6) to roughly 10^7 incoming electrons per diffraction pattern. Note that the previous estimation ignores technical noise sources in the detection scheme. Typically, 100 different pump-probe-delays must be recorded to adequately sample a dynamical process. Thus roughly 10^9 electrons are required for an entire UED study.

2.2 Transverse coherence

In diffraction, the spatial resolution is directely connected to the transverse coherence of the incoming electron beam. The required coherence length can be estimated from multi-slit interference theory where the intensity is given as

$$I_\mathrm{MS} = I_0 \frac{\sin\left[\frac{N\pi g}{\lambda}\,\sin(\phi)\right]^2}{N^2\,\sin\left[\frac{\pi g}{\lambda}\,\sin(\phi)\right]^2} \tag{2.7}$$

$$\sin(\phi) = \frac{x}{\sqrt{l^2 + x^2}} \approx \frac{x}{l} \tag{2.8}$$

with I_0 the peak intensity, g the spacing of the small slits, λ the wavelength, ϕ the angle and N the number coherently illuminated slits. In Eq. (2.8) $x \ll l$ was used with x the position on the detector and l the distance of the multi-slit to the detector. The distance between different peaks is

$$\Delta x = \frac{\lambda\, l}{g} \tag{2.9}$$

and the half width half maximum σ_x of the reflections estimated from a Taylor expansion of I_MS at $x = 0$ is

$$\sigma_x \approx \frac{\sqrt{3}\lambda\, l}{\sqrt{2}\pi\, g\,\sqrt{N^2 - 1}}\ . \tag{2.10}$$

As a criterion for accurate distinguishability of different orders, the half width half maximum σ_x of the reflections should be roughly ten times smaller than the distance Δx. Using Eqs. (2.9) and (2.10), the required number of illuminated slits is $N \approx 4$ which is in agreement with claims in literature [64].

With typical unit cell sizes of about 5 Å, the required coherence length (N times the lattice constant) is only a few nanometers at the sample. However, molecular or protein crystals have much larger lattice of 1 nm to 10 nm [7, 25, 26, 64, 65]. To be able to accurately investigate such samples with UED, coherence lengths of several tens of nanometers at the sample are required. The required global degree of coherence (transverse coherence length over beam diameter) can be calculated to roughly 10^{-3} for 50 µm beam diameter at the sample.

2.3 Temporal resolution

The temporal resolution required for observation of transient atomic motions is determined by the speed of these dynamics. From the chemical point of view, a reaction leads to changes in atomic position on the order of bond lengths, typically $\sim 1\,\text{Å}$. Taking into account characteristic nuclear velocities in solids, e.g. the speed of sound ($\sim 1\,\text{km/s}$), the duration for the nuclear motion is estimated to roughly 100 fs. However, the fastest nuclear motion, such as excited state intramolecular proton transfer (ESIPT) [65–67], occur on time scales of tens of femtoseconds. From the physical point of view, relevant changes in positions, e.g. caused by phonons, are much smaller. Taking into account typical phonon amplitudes of 5 pm (see Section 2.1) and the speed of sound, relevant time scales are on the order of 10 fs. The period of the highest phonon mode in a system is approximately $\tau_\text{D} = h/\left(k_\text{B}\,\Theta_\text{D}\right)$ with h the Planck constant, k_B the Boltzmann constant and Θ_D the Debye-Temperature. Typical values for Θ_D cover a range from 50 K to 2000 K, corresponding to periods down to roughly 20 fs. This estimate is consistent with experimental studies on coherent optical phonons where periods of less than 20 fs have been observed via pump-probe spectroscopy [19, 68]. Fast phonons play a key role in many interesting processes, e.g. the breakdown of superconductivity [9], changes of electrical properties [18], or as a probe for other ultrafast processes [6]. Going beyond nuclear motions, it has been proposed that charge density modulations from electronic dynamics could be observed with UED as well [69]. These processes are typically on the attosecond time scale [69, 70].

In summary, a temporal resolutions of roughly 10 fs or below is required to provide the observation of even the fastest transient atomic motions.

Chapter 3

Time-resolved electron diffraction – State-of-the-art

Several research groups worldwide have implemented ultrafast electron diffraction (UED) experiments with different concepts and goals [5, 14, 15, 47–53, 71–73]. A schematic of a simple UED setup is given in Fig. 3.1. Using a beam splitter (BS), a femtosecond laser pulse is split into a pump and a probe beam. The actual electron diffraction must be performed at 10^{-6} mbar or below due to the high scattering cross section of the residual gas molecules. The pump beam is ultimately focused with a lens (FL1) onto the crystalline

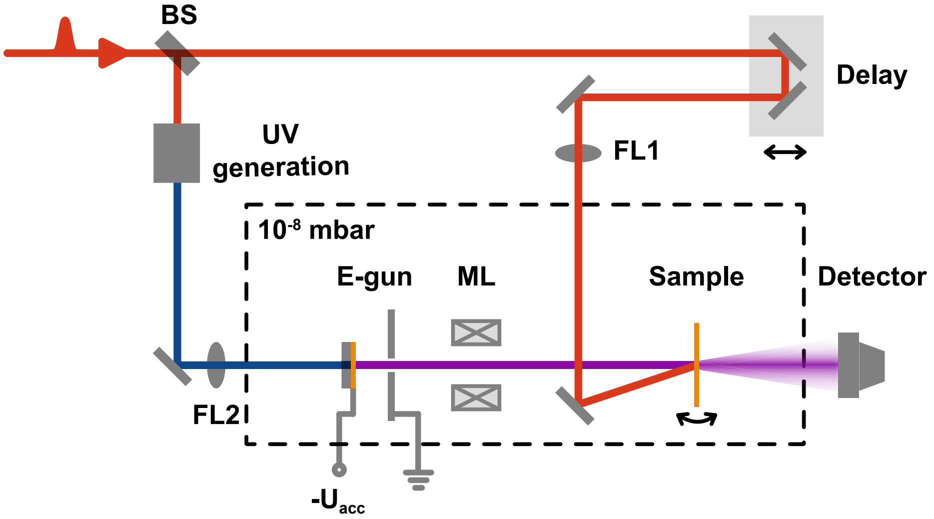

Figure 3.1: Typical setup for time-resolved electron diffraction experiments. A laser pulse is split into pump and probe beam (BS). The pump beam is focused onto the sample while the probe beam is transformed to electron pulses using a photoemission electron gun. Electrons are focused onto the sample using magnetic lenses (ML). Diffraction patterns are recorded at the detector. See text for further details.

sample, initializing the dynamics of interest. The probe pulse is usually up-converted to ultraviolet (UV) wavelength and focused with a lens (FL2) onto a metal thin film that is mounted close to a metal plate with an aperture. The metal thin film is at constant negative potential U_{acc} and the metal plate at ground potential; these are respectively the photocathode and anode. Electrons from photoelectric emission are accelerated in the static field towards the anode and additional electron optics (e.g. a magnetic lens (ML)) are used to control the electron beam size at the sample and the detector. Detection schemes are typically based on micro-channel plates or phosphor screens coupled to photosensitive cameras [74], such as charge-coupled devices (CCD) [74] or active-pixel sensors (APS) based on complementary metal–oxide–semiconductor (CMOS) technology [2]. Detector dimensions are usually on the order of a few centimeters and typical pixel dimensions are on the order of tens of microns. By recording a series of diffraction patterns for different pump-probe time delays, the dynamics of interest are sampled in structural snapshots with atomic resolution.

3.1 Spatial resolution

3.1.1 Angular resolution

The angular resolution of the detection scheme is determined by the distance between sample and detector, l_{SD}, and the spatial resolution of the detector, Δx. Assuming the detector size $x \ll l_{\mathrm{SD}}$,

$$\frac{\Delta x}{l_{\mathrm{SD}}} \approx 2\Delta\theta \overset{Eq.~(2.2)}{=} \frac{2\,\lambda\,\delta}{\sqrt{4\,d_{hkl}^2 - \lambda^2}} \tag{3.1}$$

with δ the relative change in lattice spacing d_{hkl} and λ the electron wavelength,

$$\lambda = \frac{h\,c}{\sqrt{2\,m_{\mathrm{e}}\,c^2\,E_{\mathrm{kin}} + E_{\mathrm{kin}}^2}}\ , \tag{3.2}$$

with h as Planck's constant, c the speed of light, m_{e} the electron mass and E_{kin} the kinetic electron energy.

Typically, UED experiments are "tabletop" and fit the laboratory scale which limits the distance between sample and detector l_{SD} to a range from 0.1 m to 2 m. The spatial resolution of mentioned detection schemes is usually on the order of 10 µm. Taking into account typical values for d_{hkl} (0.5 Å to 5 Å) and δ (10^{-2} to 10^{-3}), suitable values for E_{kin} are roughly 2 keV to 200 keV. Requiring that the outermost reflection ($d_{hkl} = 0.5$ Å) still fits the dimension of the detector ($x = 25$ mm), the range of suitable kinetic energies is limited further to 10 keV to 200 keV, corresponding to de Broglie wavelengths from 2.5 pm to 12 pm.

Although UED at kinetic electron energies in the MeV-range, using particle accelerators [75] and laser plasma acceleration [76, 77], has been proposed [78, 79], experiments suffer from large dimensions, decreasing scattering cross sections and large electron energy spread [77] limiting the transverse coherence (see Section 3.2). Furthermore, the beam divergence can play a major role limiting the resolution of MeV-diffraction experiments. Therefore, most of the UED experiments working with electron energies from 10 keV to 200 keV [31]. However there is a disadvantage to this energy range, which is that it requires thin samples in transmission, putting high demands on sample preparation as will be discussed in Chapter 6.

3.1.2 Signal-to-noise

The number of electrons required for a certain SNR was estimated in Section 2.1.2. However, the estimate is only a lower limit as noise sources besides shot noise were not taken into account. The achieved signal-to-noise levels from recent UED studies estimated from published data are in the range from 20 to 50 [5, 48, 51, 53, 72, 80, 81]. The best values are 70 to 100 [14, 50, 82]. No correlation with the details of the specific experiments, such as electron pulse densities, used laser systems, etc., could be found.

3.2 Transverse coherence[1]

In Section 2.2, the required coherence length at the sample was estimated to be roughly four times the lattice constant of the crystal. The lattice constant is on the order of nanometer in molecular crystals and up to 10 nm for biological samples. The transverse coherence length of an electron beam is

$$L_\perp \equiv \frac{\lambda}{2\,\pi\sigma_\theta} \overset{[2]}{=} \frac{\hbar}{m_\mathrm{e}\,\sigma_{v_\perp}} \tag{3.3}$$

with σ_θ the uncorrelated angular spread, $\sigma_{v_\perp}$ the uncorrelated transverse velocity spread and m_e the electron mass. Equation (3.3) directly indicates that due to the small de-Broglie wavelength determined in Section 3.1.1 large transverse coherence is only observed for small values of $\sigma_{v_\perp}$. Due to the fermionic nature of electron as well as intra-pulse Coulomb repulsion (discussed in detail in Section 3.3) that leads to an increase of $\sigma_{v_\perp}$ the achievable coherence length in pulses with high electron densities is limited [2, 31, 64, 83, 84]. In the absence of space charge, the global degree of coherence (GDC) ($L_\perp$ over beam diameter) is conserved and therefore a characteristic quantity. Consequently the coherence length can be increased by simply increasing the beam diameter at the cost of signal-to-noise given the limited size of the sample (typically on the order of 10 µm to 100 µm, see Chapter 6). Therefore, high GDC values are desirable. Different source types have been developed to realize high GDC. Reported values for different approaches are presented in Table 3.1. One can clearly see that typical flat emitter sources are far from the required GDC of 10^{-3} for studying molecular crystals. Especially in the case of high electron density within the pulse, space charge limits the theoretical achievable GDC to unacceptable levels.

---

[1] This section is based on the results published by Kirchner, Lahme, Krausz, and Baum [2].

Source details	$\mathbf{L_\perp}$	$\mathbf{2\,r_{\text{FWHM}}}$	**GDC**	**Ref.**
Flat emitter, $1\,e$/pulse	3 nm	350 µm	8.6×10^{-6}	[85]
Flat emitter, $6 \times 10^5\,e/\text{pulse}^\dagger$	3 nm	250 µm	1.2×10^{-5} *	[86]
Ultracold gas, $\sim 1000\,e$/pulse	- -	- -	$(3\text{–}4) \times 10^{-4}\,1$*	[87, 88]
Shaped ultracold gas, $10^5\,e$/pulse	10 nm	- -	- -	[89]
Tip emitter, field emission	- -	- -	0.01–0.2	[90, 91]
Tip emitter, laser-triggered	6 mm	19 mm	0.3	[92]

Table 3.1: Reported values for transverse coherence $L_\perp$ and beam diameter $2\,r_{\text{FWHM}}$ at the sample or rather the global degree of coherence (GDC). Starred values are measured at the sample and are not conserved due to space charge effects, dagger indicates theoretical studies.

So far, the highest values reported forces global degree of coherence are for tip-based sources [92–96]. Laser-induced photoemission from metal nano-tips with sub-wavelength radii leads to effective emission areas of only a few nanometers. The large Schottky effect due to the high fields at the surface of the tip provides tuning of the work function (detailed discussion in Section 3.3.1). The high bias field also significantly mitigates dispersive broadening (see Section 3.3.3) [93]. Electron fluences of hundreds of electrons per pulse have been reported [95]. Tip-based sources are therefore a promising source for UED [93] and dielectric laser accelerators [97, 98]. However, the curved emission from the tips causes temporal distortions that must be corrected, for example by using a magnetic lens, as proposed in Hoffrogge et al. [93]. Tip-based sources are thus extremely promising for UED, but more development work is required, for example to evaluate the tradeoffs between energy spread, effective source size, and electron yield with different emission processes and to demonstrate long-term stability.

In summary, further development of highly-coherent pulsed electron sources is required to achieve GDC values sufficient for UED on molecular samples. To reach sufficient flux and high GDC at the same time, new gun concepts have to be pursued as conventional sources are mainly limited by space charge forces within the electron pulse. A promising new concept for improving the GDC of flat emitters will be discussed in Section 5.2.

3.3 Temporal resolution

One of the major challenges in time-resolved electron diffraction is to push the temporal resolution towards the required 10 fs-regime (see Section 2.3). The temporal resolution τ_{res} of UED experiments is given by the width of the instrument response function (IRF) [27, 51, 64, 82, 99–101]. The latter is defined as the cross-correlation of the temporal intensity profiles $I_\nu(t)$ and $I_\mathrm{e}(t)$ of the pump and probe beam, respectively [99, 102], given by

$$IRF\,(\Delta t) = \int\limits_{-\infty}^{\infty} I_\nu(t)\; I_\mathrm{e}(t+\Delta t)\;\mathrm{d}t \tag{3.4}$$

with Δt the time delay between pump and probe pulses. Note that in the case of multiple repetitions of the pump-probe experiment, $I_\nu(t)$ and $I_\mathrm{e}(t+\Delta t)$ do not represent the individual pulse durations but rather effective pulse durations [103] taking into account any time-delay fluctuations during the acquisition time. Compared to the pulse durations of individual pulses, the effective pulse duration can be significantly broadened by the mechanisms discussed below. Furthermore, Eq. (3.4) considers collinear pulse propagation, which is not achieved in typical UED setups. In Section 3.3.2 different techniques are discussed that provide non-collinear pump-probe geometries without violating Eq. (3.4). Because of the advanced state of development of ultrafast optics, optical pulse durations of a few femtoseconds [104, 105] or even attoseconds [106, 107] are achievable. Hence, in typical UED experiments the duration of the pump pulse can be neglected and τ_res is dominated by the effective electron pulse duration $\tau_\mathrm{e}^\mathrm{eff}$. The following sections highlight various fundamental and technological contributions to $\tau_\mathrm{e}^\mathrm{eff}$, as well as current approaches to reduce it.

3.3.1 Random timing jitter and temporal distortion

The inherent synchronization of pump and probe beam in optical pump-probe schemes is in general not conserved in UED. In particular, timing jitter of the electron pulse generation mechanism significantly affects the synchronization leading to an increase of effective electron pulse duration. Furthermore, distortions of the electron pulse can significantly increase its effective pulse duration. In the following, different sources for jitter and distortion are discussed.

Photoemission process

In typical UED experiments, the probing electron pulses are generated by focusing a UV laser pulse onto a thin metal film, and the emitted photoelectrons are subsequently accelerated in a static electric field (see Fig. 3.1). A simplified picture of photoemission at zero temperature without acceleration field is shown in Fig. 3.2a. Photoemission can be described with the three step model of Puff [108] and Berglund et al. [109]. In the first step, a photon of energy E_ν is absorbed by an electron with a binding energy E_B which is defined as the difference between the electron energy and the vacuum energy level $E_\mathrm{vac} = 0$. Then, the electron can migrate through the metal to the surface, in the process undergoing elastic and inelastic scattering. In the third step, if the electron's energy $(E_\nu + E_\mathrm{B})$ normal to the surface is high enough to overcome the potential barrier to the vacuum it is emitted. For an electron which initially is at the highest occupied electron energy level, i.e. the Fermi level E_FL or chemical potential, the lowest value for $|E_\mathrm{B}|$ is observed. This is

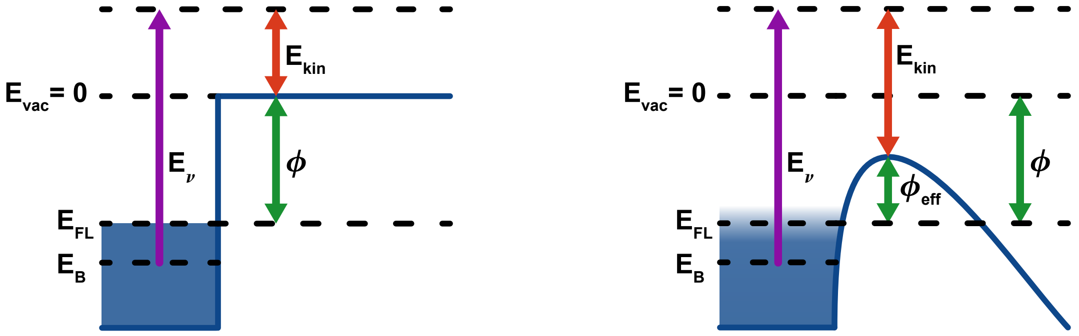

(a) (b)

Figure 3.2: Simple picture of photoemission [110]. (a) Quasi-free electrons are caught in a potential without external fields and at 0 K. The work function ϕ is defined as the minimal energy required to excite an electron to the vacuum potential E_{vac}. (b) Realistic temperature smears out the Fermi level and an applied external field reducing the work function to ϕ_{eff}.

called the work function ϕ and describes the minimum photon energy required for photoemission. Excess energy in the photoemission process is transferred to kinetic energy E_{kin}. Figure 3.2b illustrates photoemission for non-zero temperature and with an acceleration field applied. Temperature smears out the Fermi level as described by the Fermi-Dirac distribution. The applied field reduces the work function to ϕ_{eff} via the Schottky effect [110]. Therefore, the kinetic energy of a photoelectron is

$$E_{\mathrm{kin}} = E_\nu + E_{\mathrm{B}} + \phi - \phi_{\mathrm{eff}} \ . \tag{3.5}$$

For UED it is beneficial to only emit electrons that are close to the Fermi level in order to achieve $E_{\mathrm{kin}} \approx 0$. This is because of the dispersive broadening mechanism discussed in Section 3.3.3. However, the excitation of electron and possible subsequent emission is a statistical process resulting in timing jitter.

The timing jitter can be estimated from the mean free path length of an electron close to the vacuum level E_{vac} inside the photocathode. The energy E_{e} and direction of such an electron can change due to inelastic and elastic scattering events. Inelastic scattering leads to energy loss and thereby prohibits photoemission (because $E_{\mathrm{e}} < E_{\mathrm{vac}}$). Elastic scattering only changes the direction of the electron but as scattering occurs into all directions, the probability that the electron reaches the surface decreases strongly with the number of elastic scatter events. Therefore one can assume, that photoelectrons only accrue from a depth of a few times the mean free path. Taking into account this distance, the difference in arrival time can be calculated from the electron velocity at E_{e}. Note that in the previous paragraph, energies were defined with respect to the vacuum level. For the following estimate, the energies are defined with respect to the bottom of the conduction band for convenience. At low temperatures, the Fermi level can be assumed to be equal to the Fermi energy E_F and for typical field strength applied in UED $\phi_{\mathrm{eff}} \approx \phi$ [110]. The Fermi energy is given as

$$E_{\mathrm{F}} = \frac{\hbar}{2\,m_{\mathrm{e}}} \left(3\,\pi^2\,n\right)^{\frac{2}{3}} \tag{3.6}$$

with $\hbar$ the reduced Planck constant, m_{e} the electron mass and n the number density of the metal. For gold, which is a typical photocathode material, E_{F} can be calculated as 5.5 eV and the work function is known to be approximately 4 eV for thin films [85], leading to $E_{\mathrm{vac}} \approx 10\,\mathrm{eV}$. The mean free path can be determined from the so-called "universal curve" [111] to be around 1 nm to 5 nm and the resulting difference in arrival time is $\tau_{\mathrm{PE}} \approx 5\,\mathrm{fs}$, which is in agreement with literature [112, 113]. This difference in arrival time represents a random timing jitter in electron generation and increases the effective pulse duration. In principle, working with a thinner metal film could reduce the jitter from photoemission but also leads to a decrease in emission yield as the chance that a photon is absorbed is proportional with the film thickness.

An additional contribution to arrival time jitter is given by the duration of the laser pulse, as it defines the time window in which photoelectron can be generated statistically. Hence, film thicknesses of less than 10 nm are only beneficial for laser pulses with pulse durations less than τ_{PE}.

Stability of the acceleration voltage

Another source for jitter in arrival time results from technological stability limitations of the acceleration field strength. High-precision high-voltage power supplies provide voltage stabilities of 10^{-5} or better[2] [114] at several 100 kV. Solving the relativistic equation of motion, the propagation time t_{p} of the electron from photocathode to sample is

$$\mathsf{t}_{\mathrm{p}}(U_{\mathrm{acc}}) = \underbrace{\frac{l_{\mathrm{CA}}}{c}\left(1 + \frac{2\,m_{\mathrm{e}}\,c^2}{e\,U_{\mathrm{acc}}}\right)^{\frac{1}{2}}}_{\substack{\text{Acceleration}\\ \text{to anode}}} + \underbrace{\frac{l_{\mathrm{AS}}}{c}\left(1 + \frac{m_{\mathrm{e}}^2\,c^4}{2\,m_{\mathrm{e}}\,c^2\,e\,U_{\mathrm{acc}} + e^2\,U_{\mathrm{acc}}^2}\right)^{\frac{1}{2}}}_{\substack{\text{Propagation}\\ \text{to sample}}}. \tag{3.7}$$

with m_{e} the electron mass, e the electron charge, U_{acc} the applied voltage, l_{CA} the distance from photocathode to anode, and l_{AS} the distance from anode to sample. The difference in arrival time is then

$$\tau_{\mathrm{HV}} = \left| \mathsf{t}_{\mathrm{p}}\!\left(U_{\mathrm{acc}} + \frac{\Delta U_{\mathrm{acc}}}{2}\right) - \mathsf{t}_{\mathrm{p}}\!\left(U_{\mathrm{acc}} - \frac{\Delta U_{\mathrm{acc}}}{2}\right) \right| \tag{3.8}$$

with ΔU_{acc} the width of the absolute voltage fluctuation.

---

[2] E.g. PNChp-Series from Heinzinger electronic GmbH, Germany, `http://www.heinzinger.de/uploads/files/downloads/PNChp.pdf` (Accessed: 20 June 2014).

Assuming $l_{\mathrm{CA}} = 10\,\mathrm{mm}$ and a relative voltage stability of 10^{-5}, the difference in arrival time τ_{HV} at the sample for different acceleration field strength E_{acc} is

$$\begin{aligned} \tau_{\mathrm{HV}}(l_{\mathrm{AS}}) &\approx 0.5\,\mathrm{fs} + 23\,\frac{\mathrm{fs}}{\mathrm{m}} \cdot l_{\mathrm{AS}} \quad \text{for} \quad E_{\mathrm{acc}} = 10\,\frac{\mathrm{kV}}{\mathrm{mm}}, \\ \tau_{\mathrm{HV}}(l_{\mathrm{AS}}) &\approx 0.7\,\mathrm{fs} + 35\,\frac{\mathrm{fs}}{\mathrm{m}} \cdot l_{\mathrm{AS}} \quad \text{for} \quad E_{\mathrm{acc}} = 5\,\frac{\mathrm{kV}}{\mathrm{mm}}. \end{aligned} \tag{3.9}$$

Note that the arrival time jitter decreases with increasing E_{acc}.

In summary, these results are in rough agreement with reported non-relativistic estimations [31]. As achievable field strengths at ultrahigh vacuum (UHV) conditions are usually limited to approximately 10 kV/mm [115], the arrival time jitter caused by instabilities of the high-voltage power supply can be estimated to be on the order of 10 fs.

Temporal distortions from magnetic lenses

A different mechanism increasing the effective electron pulse duration is temporal distortion caused by the electron optics. In UED, solenoid lenses (see Fig. 3.1) are used to focus the electron beam. The focusing mechanism of this type of lens conserves the electron's absolute velocity and can be described as three step model [116]. First the electron enters the inhomogeneous field outside the lens which imparts an azimuthal velocity as a function of distance from the optical axis. The subsequent homogeneous field inside the solenoid produces helical trajectories, leading to periodic focusing. In the third step, the inhomogeneous field after the lens removes azimuthal velocity components, leaving the electrons with transverse velocity components proportional to their distance from the axis, which produces a focus.

Weninger et al. [117] reported on inherent temporal distortions from solenoid lenses, mainly caused by two different mechanisms. First, off-axis electrons take significantly longer to pass the magnetic lens because some of their forward velocity is converted to azimuthal velocity in the lens region. Second, the conservation of absolute velocity during focusing leads to different arrival times for on- and off-axis electrons propagating from the lens to the sample. The authors estimated both contributions for non-relativistic electrons that in sum are given as

$$\tau_{\mathrm{ML}} \approx \left(\frac{g^2}{b} + \frac{g}{2} - \frac{b}{2} \right) \frac{v_r^2}{v_z^3} \tag{3.10}$$

with g the distance between solenoid and source and b the distance between solenoid and spatial focus, v_r the radial velocity and v_z the on-axis velocity. Note that τ_{ML} is proportional to the square of the radial velocity. The latter is caused by an energy spread of the photoelectrons that will be discussed in Section 3.3.3. From Eq. (3.10) zero temporal distortion is expected for $b = 2g$ which is called the isochronic setting. This is confirmed by simulations [117]. The minimum achievable temporal distortion observed in these simulations are on the order of a few femtoseconds.

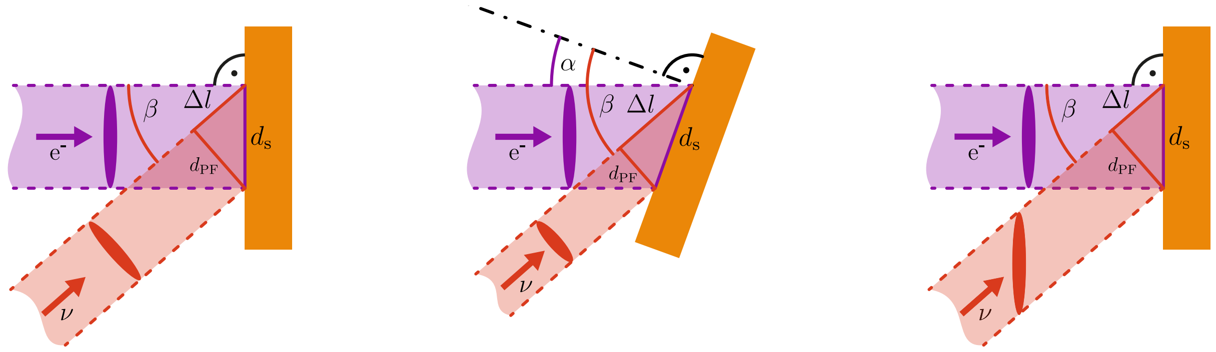

(a) (b) (c)

Figure 3.3: (a) Typical UED geometry. The non-collinear beam geometry leads to significant temporal mismatch, as the laser pulse front "rolls" along the surface. (b) Phase matching realized by tilting the sample in a way that the surface velocities of the electron and laser pulse fronts are equal. At typical electron velocities, this technique is limited to small diffraction angles. (c) Phase matching realized by tilting the laser pulse front. In this scheme the surface velocity of the laser can be adjusted to that of the electrons. For simplicity $\alpha = 0$ was chosen but in principle, arbitrary diffraction angles are supported.

Temporal distortions from a misalignment of the solenoid's axis were discussed by Kreier et al. [118]. Tilting or displacing the solenoid's symmetry axis with respect to the electron propagation vector were calculated to increase the effective pulse duration by 50 fs/° and 50 fs/mm for the used lens. However, following a demonstrated alignment procedure providing sufficient accuracy, these distortions can be minimized to the sub-femtosecond level [118].

3.3.2 Pulse front overlap

As written, Eq. (3.4) assumes the beams and collinear and incident perpendicular to the sample surface. In practice however, the angle of incidence of the electron beam must be chosen according to the Bragg reflections of interest (compare Appendix A). Collinear beam propagation is inconvenient and very challenging to realize due to the curved electron trajectory caused by the earth magnetic field. A typical geometry is shown in Fig. 3.3a. Electron and laser beam are spatially overlapped on the sample. For simplicity, the incident angle of the electron beam is chosen to be 0° whereas the pump beam hits the sample under the angle β. In contrast to the electron pulse, which probes the entire surface simultaneously, the laser pulse front "rolls" along the surface. The surface velocity can be derived referring to the labels in Fig. 3.3a as

$$v_{\mathrm{sur},\nu} = \frac{c\sqrt{{d_\mathrm{PF}}^2 + \Delta l^2}}{\Delta l} = \frac{c}{\sin\beta} \tag{3.11}$$

with c the speed of light. It follows that the timing mismatch of electron and laser pulse is

$$\tau_{\mathrm{PFM}} = \frac{d_{\mathrm{s}}}{v_{\mathrm{sur},\nu}} = \frac{d_{\mathrm{s}}\ \sin\beta}{c}\ . \tag{3.12}$$

Assuming $\beta = 10°$ and an electron beam diameter of 50 µm, τ_{PFM} is about 15 fs.

One approach to compensate this mismatch is to tilt the sample [69], taking advantage of the different forward velocities of the pump and probe pulses. As shown in Fig. 3.3b, the electron beam hits with an incident angle α causing a finite surface velocity of the electron pulse front $v_{\mathrm{sur,e}}$. The temporal mismatch between electron and laser pulse vanishes when their surface velocities are equal:

$$\frac{c}{\sin\beta} = v_{\mathrm{sur},\nu} \overset{!}{=} v_{\mathrm{sur,e}} = \frac{v_{\mathrm{e}}}{\sin\alpha} \tag{3.13}$$

with v_{e} the velocity of the electrons. Usually α is chosen according to the Bragg reflections of interest. For ideal phase matching the incident angle of the laser must be adjusted to

$$\beta = \arcsin\left(\frac{c\ \sin\alpha}{v_{\mathrm{e}}}\right) \quad \text{with} \quad v_{\mathrm{e}} > c\ \sin\alpha\ \Leftrightarrow\ \beta < 90°\ . \tag{3.14}$$

The condition in Eq. (3.14) shows the limitation of this approach. For a diffraction angle of 20° and a electron velocity of $0.3c$ a valid value for β can not be found and the temporal mismatch cannot be compensated. Furthermore, the influence of the generated wave of sample excitation on time-resolved results is controversial.

Another approach is to tilt the laser pulse front instead of the sample. This technique was described by Baum et al. [119] and is illustrated in Fig. 3.3c. Again, for simplicity, the incident angle of the electron beam is chosen to be 0° whereas the pump beam hits the sample under the angle β. The laser pulse front is tilted so that the surface velocities of electron and laser pulse front are equal and thereby temporal mismatch is avoided. In general this scheme supports arbitrary diffraction angles if the laser pulse front tilt is adjusted appropriately.

3.3.3 Temporal pulse broadening mechanisms

A three-dimensional particle tracking technique[3] was used to calculate individual trajectories of 10^3 electrons in a pulse generated with a typical DC electron gun with an anode-cathode distance of 8.5 mm, a acceleration field strength of 3.5 kV/mm, an anode radius of 1 mm and a source size of 3 µm [2]. The result is illustrated in Fig. 3.4. The radial position of each individual electron is given versus its difference in arrival time relative to the mean arrival time of the electron pulse for different positions along the propagation axis (z). During acceleration, massive broadening of the initially short electron pulse ($z = 0$ mm, see inset in Fig. 3.4) can be observed, leading to nearly picosecond pulses at the anode

---

[3] The General Particle Tracer (GPT) package, Pulsar Physics, The Netherlands, `http://www.pulsar.nl/gpt` (Accessed: 18 June 2014)

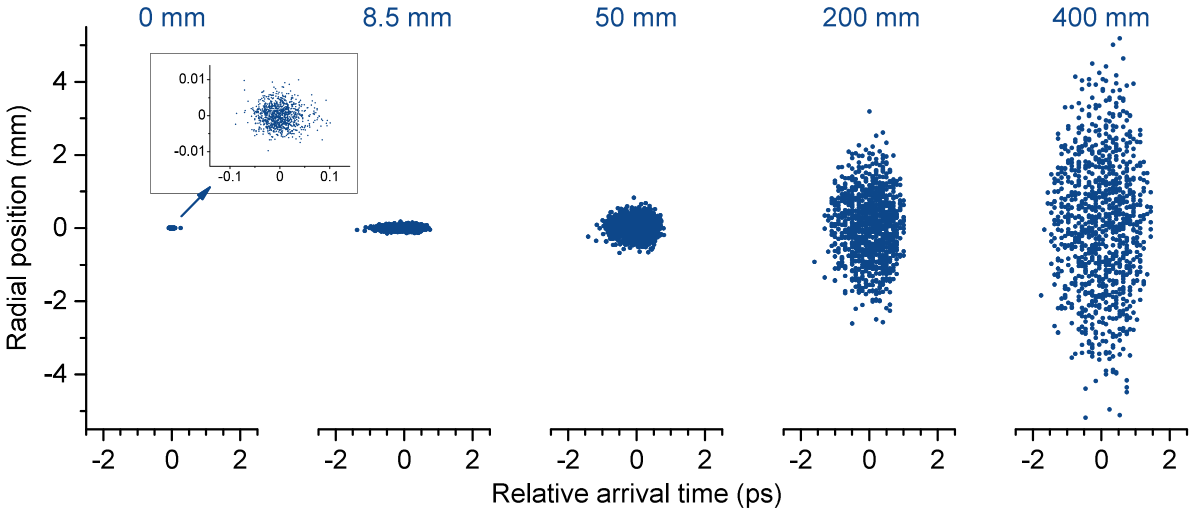

Figure 3.4: Radial position of 1000 individual electron versus its difference in arrival time relative to the mean arrival time of the electron pulse for different positions along the propagation axis (z). Pulse broadening in the acceleration region ($z = 0\,\mathrm{mm}$ to $8.5\,\mathrm{mm}$) as well as for field free propagation ($z = 8.5\,\mathrm{mm}$ to $400\,\mathrm{mm}$) can be observed. Simulations were performed for a typical UED geometry using the General Particle Tracer package.

($z = 8.5\,\mathrm{mm}$). Broadening continues during field free propagation ($z = 8.5\,\mathrm{mm}$ to $400\,\mathrm{mm}$) leading to temporal and spatial dimensions that are to large for UED even at sample positions close to the anode.

The observable temporal broadening for electrons traveling through vacuum arises from two different temporal broadening mechanisms: dispersive and space charge broadening. The underlying physics as well as fundamental limitations will be discussed in the following sections.

Dispersive broadening

In the simple picture of photoemission introduced in Section 3.3.1, an electron at the Fermi level can only be removed from the photocathode for $E_\nu \geq \phi$ and excess energy is transferred to kinetic energy of the electron. Different kinetic energies lead to different velocities towards the sample causing variations in arrival time and effectively broadening the pulse. This mechanism is called dispersive broadening. Eq. (3.5) shows that dispersive broadening can be avoided completely ($E_{\mathrm{kin}} = 0$) by tuning the laser photon energy to the work function of the photocathode. This can easily be achieved using monochromatic illumination but a laser pulse with the duration τ_ν fundamentally requires a minimum spectral bandwidth ΔE_ν around its central energy $\overline{E_\nu}$ given by

$$\Delta E_\nu\,\tau_\nu = \frac{2\,h\ln 2}{\pi}, \tag{3.15}$$

with h the Planck constant. Therefore $E_\nu = \phi$ cannot be achieved for all photons contained in the laser pulse. Photons with higher energy can also eject electrons from slightly lower energy states defined by the fermi distribution of the electron gas. Realistic photocathodes are usually operated at non-zero temperature which smears out the Fermi edge and thus also the work function. Furthermore, the photocathode material is in general non-isotropic and surface inhomogeneities as well as impurities can locally change the work function so that it becomes a function of surface coordinate $\vec{r}$. Therefore the kinetic energy spread ΔE_kin of the photoelectrons corresponds to the width of the kinetic energy distribution

$$D_{E_\mathrm{kin}} = \iint\limits_A d\vec{r} \int\limits_{-\infty}^{\infty} dE'_\nu \; D_\phi \left(E_\nu - E'_\nu, \vec{r}\right) \; D_{E_\mathrm{e}} \left(E_\nu, \vec{r}\right) \tag{3.16}$$

with $D_\phi \left(E_\nu, \vec{r}\right)$ the distribution of effective work function and $D_{E_\mathrm{e}} \left(E_\nu, \vec{r}\right)$ the distribution of excited electron energies normal to the surface. The latter takes into account laser spectrum, intensity profile and scattering processes. The $d\vec{r}$ integral is taken over the cathode surface A.

In general, dispersive broadening of the electron pulses can be minimized by carefully preparing a clean and homogeneous photocathode which decreases the spread in effective work function, tuning the central laser frequency to the average work function [85] and operating the cathode at 0 K. Beside these technological challenges however, Eq. (3.15) defines a fundamental lower limitation for the kinetic energy spread using ultrashort laser pulses. The two contrary requirements, short photoemission time window and small energy bandwidth can be optimized in terms of electron pulse duration. Following Aidelsburger et al. [85], the optimum laser pulse duration τ_ν^opt is

$$\tau_\nu^\mathrm{opt} \propto E_\mathrm{acc}^{-\frac{2}{3}}, \tag{3.17}$$

with E_acc the acceleration field strength. Hence, increasing the field strengths remains the only parameter for decreasing the electron pulse duration but is limited to approximately 10 kV/mm [115].

Dispersive broadening at a typical DC electron gun with an anode-cathode distance of 8.5 mm, an anode radius of 1 mm and a source size of 3 µm [2] was simulated via particle tracking[4]. The root mean square (rms) pulse duration averaged over 10^4 electrons was calculated at the position of the anode for field strengths from 1 kV/mm to 10 kV/mm, only taking into account the initial velocity spread given by the energy bandwidth of the laser [85]. The results of these idealized calculations are shown in Fig. 3.5. Figure 3.5a shows the electron pulse duration at the anode for different bandwidth limited laser pulse durations and two different acceleration field strengths, clearly indicating the expected shift in optimum laser pulse duration. However, the plotted traces for different field strengths also indicate that at a given laser pulse duration above 20 fs, an increase in field strength

---

[4] The General Particle Tracer (GPT) package, Pulsar Physics, The Netherlands, `http://www.pulsar.nl/gpt` (Accessed: 18 June 2014)

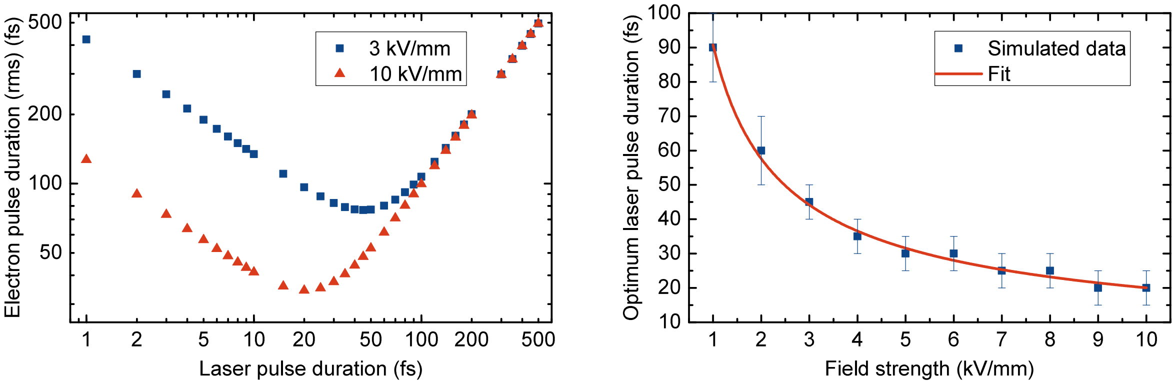

(a) (b)

Figure 3.5: (a) Resulting electron pulse duration at the anode from dispersive broadening depending on the laser pulse duration. Only laser energy bandwidth is taken into account. A clear optimum is observable that shifts with the laser pulse duration. (b) Laser pulse duration leading to shortest possible electron pulse durations for different acceleration field strengths.

does not significantly decreasing the electron pulse duration. Figure 3.5b shows the optimum laser pulse duration for different field strengths and a fitted exponent of -0.67 ± 0.01 reproduces Eq. (3.17) and numerically supports the estimates in Aidelsburger et al. [85].

One has to mention that the presented results are valid only for very idealized photoemission, assuming a perfectly homogeneous work function of the photocathode and a best possible tuned laser wavelength. However, the presented simulations give an upper limit for achievable electron pulse durations and strongly indicate that for this type of electron gun the 10 fs-regime is not accessible without further efforts.

Space charge broadening

As discussed in Section 2.1.2, roughly 10^7 incoming electrons are required for a suitable diffraction image (see also Refs. [27, 120]). Electron pulses used for UED usually contain several hundreds [5, 50], thousands [14, 43, 47, 71, 121] or even up to millions [51, 101] of electrons and the diffraction image is accumulated over many pump-probe-cycles. The higher end of this range is already close to the so-called “single-shot” regime. However, electrons are charged fermions. With multiple electrons in a single pulse, intra-pulse Coulomb repulsion gradually transfers potential Coulomb energy of the electrons into a kinetic energy, resulting in significant temporal broadening of the electron pulse. In contrast to dispersive broadening, with space charge broadening the kinetic energy is increasing dynamically and continuously. In literature, space charge broadening is identified as the dominant contribution for electron pulses containing more than 1000 electrons per pulse [122].

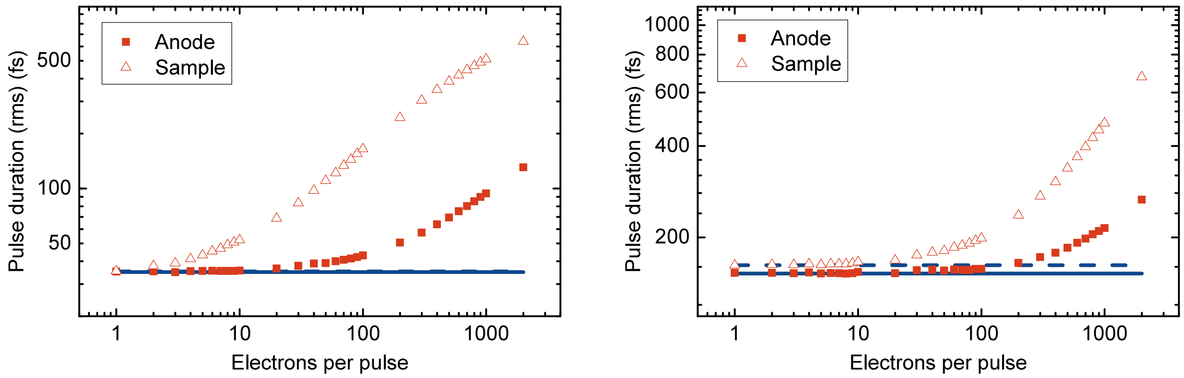

(a) (b)

Figure 3.6: Space charge broadening for different electron pulse densities and (a) ideal and (b) realistic energy spread. The resulting electron pulse durations are shown for the position of the anode (red, solid squares) and the sample (red, open triangles). The solid and dashed blue lines represent the electron pulse durations in the absence of space charge interactions (dispersive broadening only) at the position of the anode and the sample, respectively.

Electron pulse durations were calculated from particle tracking simulations[5] for different electron pulse densities (e/pulse) with and without space charge effects included. Simulation parameters are the same as before, with an anode-cathode distance of 8.5 mm, an anode radius of 1 mm and a source size of 3 µm. The field strength was set to 10 kV/mm. Root mean square (rms) pulse durations averaged over 10^4 electron trajectories were determined at at the anode and at the sample (465 mm from the photocathode). The results are shown in Fig. 3.6. In Fig. 3.6a the electron pulse durations were calculated only taking into account the initial velocity spread given by the energy bandwidth of the laser [85]. As expected, the pulse durations for different numbers of electron per pulse without space charge interaction do not vary and were only performed for numerical verification. The average values at the position of the anode and at the sample are given as solid and dashed blue lines respectively. The increase in pulse duration during propagation from the anode to the sample is minor, indicating that the bulk of the dispersive broadening happens during acceleration. Pulse durations at the position of the anode and the sample including space charge effects are given as red solid squares and red open triangles, respectively. Space charge broadening leads to a significant increase in pulse duration at the anode for 100 e/pulse and a significant increase in pulse duration at the sample already for less than 10 e/pulse. In Fig. 3.6b the calculations are repeated, taking into account a more realistic value for the initial energy spread of the electrons as measured by Kirchner et al. [3]. In general the observations made for the ideal case remain the same, but with further propagation of the electron pulse to the position of the sample, a slight increase in dispersive

---

[5] The General Particle Tracer (GPT) package, Pulsar Physics, The Netherlands, `http://www.pulsar.nl/gpt` (Accessed: 18 June 2014)

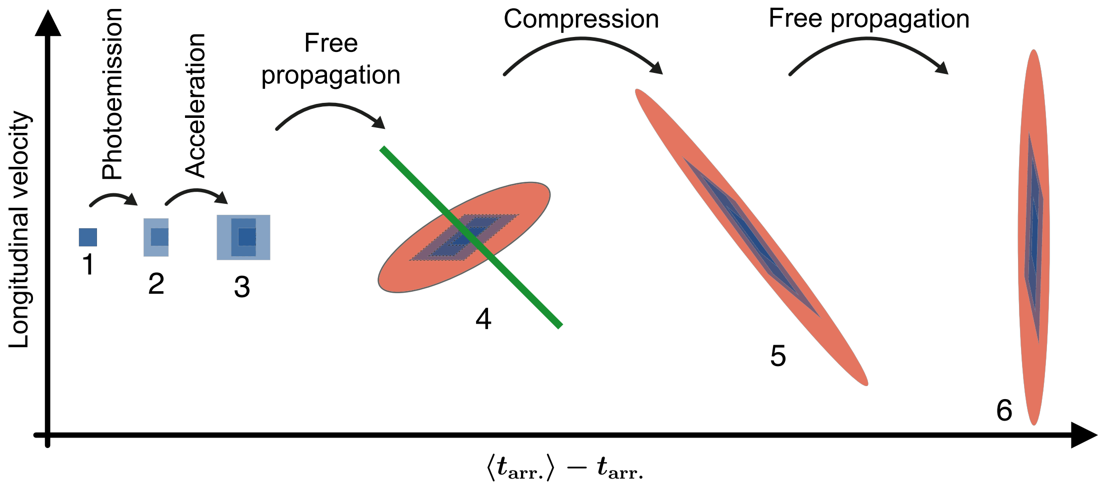

Figure 3.7: Phase volumes of an electron pulse taking into account the laser pulse duration and energy bandwidth (1), photoemission (2) and HV (3) jitter propagates (purple arrow) through vacuum and gets broadened from dispersive broadening and space charge (4). Dispersive broadening conserves the phase volume (blue parallelogram in 4) whereas space charge broadening (red ellipse in 4) increases the volume. An applied electric field (green line) re-distributes the phase space volume (5), leading to pulse compression (6).

broadening can be observed. Note that contributions from space charge broadening are negligible below 500 e/pulse and 100 e/pulse at the anode and sample, respectively. These values are much larger than those determined for ideal energy spread, because the increased dispersive broadening with larger energy spread dominates the space charge broadening for these values.

In summary, dispersive broadening can be minimized to the order of tens of femtoseconds in the ideal case by tuning the laser wavelength to the work function and the spectral width to the acceleration field. Simulations indicate that further efforts must be undertaken to reach the 10 fs-regime. However, space charge was shown to be much more problematic at ideal emission conditions than reported by Siwick et al. [122]. Hence the handling of space charge is the major challenge reaching ultimate temporal resolutions.

3.3.4 (Re-)Compression techniques

The estimates of timing jitter and simulations in Sections 3.3.1 and 3.3.3 clearly reveal that effective electron pulse duration on the order of 10 fs cannot be generated even with ideal DC electron guns. Hence, schemes for compensation of the temporal broadening are indispensable for pioneering the 10 fs-regime in UED.

The effect of the different sources of timing jitter and temporal broadening on the velocity-time phase space of an electron pulse as well as the principle of compensation is illustrated in Fig. 3.7. The longitudinal velocity of different pulses are given depending on the relative time of arrival which is defined as difference between the mean arrival time of the pulse $\langle t_{\mathrm{arr.}} \rangle$ and the actual arrival time of the electron $t_{\mathrm{arr.}}$. Scales are arbitrary for clarity. The effective pulse duration for each pulse is roughly given by the illustrated arrival time width. The leftmost blue square (1) corresponds to an ideal electron pulse with temporal width and velocity spread determined by laser pulse. In (2), timing jitter from photoemission and additional energy spread (see Eq. (3.16)) is taken into account, leading to later arrival times (for photoelectrons generated below the surface) and a spread in velocity. The pulse in (3) includes the effect of acceleration voltage jitter which causes only minor additional velocity spread but a significant increase in effective pulse duration. Spatiotemporal distortions from magnetic lenses are not taken into account, as they can be avoided by using isochronic settings and proper alignment procedures [123]. After free-space propagation, faster electrons arrive sooner whereas electrons with small velocity are delayed. Hence, dispersive broadening leads to a distortion of the electron pulse in phase space (blue parallelogram in (4)) but conserves the phase space volume. In contrast to that, space charge broadening leads to an increase in phase space volume [124] (illustrated as the reddish ellipse) due to the continuous modification of kinetic energy. From the phase space picture it becomes intuitively clear, that a kind of arrival time dependent velocity modification is required to decrease the width of the pulse. An appropriate re-distribution function, decelerating faster electron and accelerating slower electrons, is illustrated as the green line in (4). The resulting phase space volume is shown in (5). As the pulse propagates further (purple arrow) inverse dispersive broadening leads to a temporal focus, shown as the pulse on the very right hand side (6). Depending on the strength of the applied compression, the temporal focus can be tuned to the position of the sample and effective pulse durations shorter than the original pulse can be realized at the cost of energy spread. Note that space charge broadening fundamentally leads to larger effective electron pulse durations than dispersive broadening alone (blue parallelogram inside reddish ellipse) for the same compression strength.

Thus far, various approaches for pulse compression have been proposed or demonstrated. Some of the most promising ones will be introduced and discussed in the following. The use of alpha magnets is well established in high-energy particle acceleration and can compress multi-electron pulses down to tens of femtoseconds [75, 125], but as electron energies are typically in the MeV-regime, these pulses are less suitable for diffraction (compare Section 3.1). However, Tokita et al. [76] have demonstrated a temporal resolution of several hundred femtoseconds at a central electron energy of only 350 keV using alpha magnets. Another approach is to use the static electric field in a so-called reflectron compressor to re-compress the electron bunches [126, 127]. Hansen et al. [128] recently proposed a new approach for a static compression device, basically a hybrid of an omega filter and a Wien filter [129], reported to achieve attosecond pulse duration in theory. However, the simulations done by Hansen et al. [128] are based on highly idealized experimental conditions and further simulation taking into account realistic beam properties are necessary.

In recent years, several groups have implemented electron pulse compression based on microwave cavities [74, 125, 130] that are operated in TM_{010} mode at 3 GHz to 6 GHz [120, 131] providing a longitudinal electrical field [132]. If the zero crossing of this field is synchronized carefully to the temporal center of the electron pulse, the approximately linear electric field provides the velocity re-distribution required (compare Fig. 3.7). The main technical limitation of this approach has been laser-microwave synchronization jitter which is transferred to timing jitter [101, 120, 121]. Reported pulse duration achieved in diffraction experiments following this approach are in the range of 200 fs to 500 fs (FWHM) [82, 101, 133, 134]. Using ellipsoidal bunches, Oudheusden et al. [120] reported a pulse duration of 67 fs (rms), but the instrument response function was 104 fs (rms) due to laser-microwave synchronization jitter. Gao et al. [101] reported on a new approach, directly measuring the arrival time of the electron pulse for each shot. The contribution of microwave jitter could thereby be reduced to a level below 30 fs (rms) [101], but the instrument response function was dominated by the electron pulse duration of 300 fs (FWHM) and the time-stamping method only works for single-shot experiments.

The development of technologies that provide better temporal resolution in UED are of large interest [31, 135], and a variety of approaches to this problem exist [27]. Combining the time-stamping of Gao et al. [101] with the shortest individual dense pulses of Oudheusden et al. [120], one could reduce the instrument response function to approximately 80 fs (rms). Further improvements in laser-microwave synchronization, especially at higher repetition rates, could be made with intra-cavity phase detection [136], optically-enhanced direct microwave generation [131], or interferometric jitter detection [137]. Ultimately, however, compression of individual dense electron pulses is very challenging and the dynamic increase in phase space volume due to space charge (compare Section 3.3.4) might be a fundamental limitation in the case of typical gaussian shaped electron pulses [113, 124]. Uniform ellipsoidal bunches do not suffer from emittance growth but are challenging to realize [113, 124, 138] and have not so far been compressed to the 10 fs regime [120].

In summary, state-of-the-art temporal resolution in UED [101, 120] is sufficient for observation of a range of atomic motions but still is an order of magnitude to large to study the fastest interesting nuclear motions in solids as well as electronic motion on the atomic scale [135]. A main reason is the large challenge in accurate compression of typically used space-charge dominated pulses.

Chapter 4

The single-electron approach

Space charge effects turn out to be a major limitation of current UED approaches in terms of coherence Section 3.2 and temporal resolution Section 3.3. An alternative approach, circumventing these limitations is to work with so-called single-electron pulses which contain only one electron per probe pulse [139] and thereby are inherently free of any space charge effects. To completely eliminate space charge effects single-electron pulses must be implemented over the entire trajectory from the photocathode to the sample and especially in the sensitive cathode-anode region. Therefore it is not sufficient to generate single-electron pulses by spatially filtering multi-electron pulses after the anode, as is typically done in single-electron ultrafast transmission electron microscopy (UEM) [140].

Note that in contrast to space charge, kinematic broadening and timing jitter cannot be avoided completely (compare Section 3.3) and re-compression techniques are indispensable even in the single-electron regime to reach the 10 fs-regime. Simulations [130] and first experiments [131] show that pulse durations down to few-femtoseconds or below are expectable from microwave-based compression Section 3.3.4. Improving the laser-microwave synchronization using optically-enhanced direct microwave generation, single-electron pulses were demonstrated to provide an instrumental response function below 20 fs (rms) [141], indicating that unprecedented temporal resolution is achievable with the single-electron approach.

Another main advantage is the low peak radiation load for the sample. On the one hand, especially organic compounds often suffer from electron radiation leading to sample damage. On the other hand, the development of shorter pulses in the single-shot approach and improvements towards working with TEM-like sample sizes at the same time might face a fundamental problem concerning the electron density within the pulse. Assuming an electron pulse containing 10^7 electrons focused to 1 µm^2 with a pulse duration of 1 fs at an energy of 100 keV, the resulting electron density is on the order of 0.1 % of the electron density of bulk aluminum. It remains questionable if such a probe pulse reliably reads out the dynamics of the sample, especially in the case of correlated materials. In contrast, working with single-electrons, the peak electron density is usually negligibly small, even at high repetition rates.

Circumventing space charge effects by using single-electrons is very promising to reach the 10 fs-regime. However, roughly 10^9 electrons are required for a suitable time-resolved diffraction study (see Section 2.1.2) corresponding to the number of pump-probe-cycles the sample has to withstand total without damage. This entails three major challenges which is why the applicability of purely single-electron pulses to pump-probe experiments has been controversial [27] First, single-electron studies are limited to highly reversible processes. Although techniques have been developed to allow a continuous exchange of the sample, the effort for ten billion shots is unreasonably high: For a typical beam diameter of 50 µm nearly 20 m^2 of sample would be required with a re-positioning accuracy better than 1 µm (10 fs at 30 keV electron energy). Second, single-electron diffraction must be performed at higher repetition rates compared to the kilohertz rates in conventional UED [101]. The correspondingly larger thermal load on the sample puts a high demand on sample preparation. Third, even with optimized sample preparation and mounting techniques, thermal issues limit the repetition rate to hundreds of kilohertz. As a consequence, significantly longer data acquisition times are required putting high demands on the stability of essential parameters of the setup such as laser pulse energy and duration, laser and electron beam pointing, surrounding magnetic field and electron emission yield.

In this thesis an existing single-electron diffraction apparatus [2, 142] was developed further to provide capability for full single-electron diffraction studies (see Chapter 5). Special emphasis was placed on studying the decrease of photo yield in a high-coherence electron gun. Based on the results, a new design for a single-electron source which simultaneously provides sufficient long-term stability and high coherence was conceived and realized (see Section 5.2). Furthermore, the underlying physics of sample damage from excitation were investigated and the sample preparation was optimized based on the findings (see Chapter 6). The feasibility of the single-electron approach in terms of sample excitation and experimental stability is demonstrated with a proof-of-principle experiment (see Chapter 7).

Chapter 5

Apparatus for pump-probe single-electron diffraction

The first generation electron diffraction apparatus in the group of Prof. Krausz was described in 2013 by Kirchner [142]. It was principally built by Peter Baum, Friedrich Kirchner, Stefan Lahme and Alexander Gliserin, who contributed in different areas of expertise. This apparatus is unique in two ways. First, it was designed for operation in single-electron mode. Second, it has an extremely small electron source size of 4 µm resulting in a high degree of coherence of 3×10^{-4} [2]. However, due to the long integration times required for single-electron diffraction, stabilization of the system poses an extreme challenge, and the version of the apparatus described in Refs. [2, 142] did not provide sufficient stability to perform a time-resolved UED experiment with single-electron pulses. The following sections described the UED apparatus, with emphasis on developments undertaken to achieve single-electron diffraction capability.

5.1 Basic setup

A detailed sketch of the final single-electron diffraction apparatus is shown Fig. 5.1. The details of this sketch are described in the following sections. In Section 5.1.1, the laser source is described. The details of the pump-probe optics and electron optics are given in Sections 5.1.2 and 5.1.4, respectively. The sample positioning system, a custom-built beam blocker and the detection scheme are described in Section 5.1.5. The electron beam pointing is stabilized using a magnetic field stabilization system as described in Section 5.1.6.

One crucial improvement was the stabilization of photoemission yield, which was observed to decay over time in the original apparatus. A new electron gun design addressing this problem is described in Section 5.2. In Section 5.3, a signal-to-noise analysis of the full apparatus is performed.

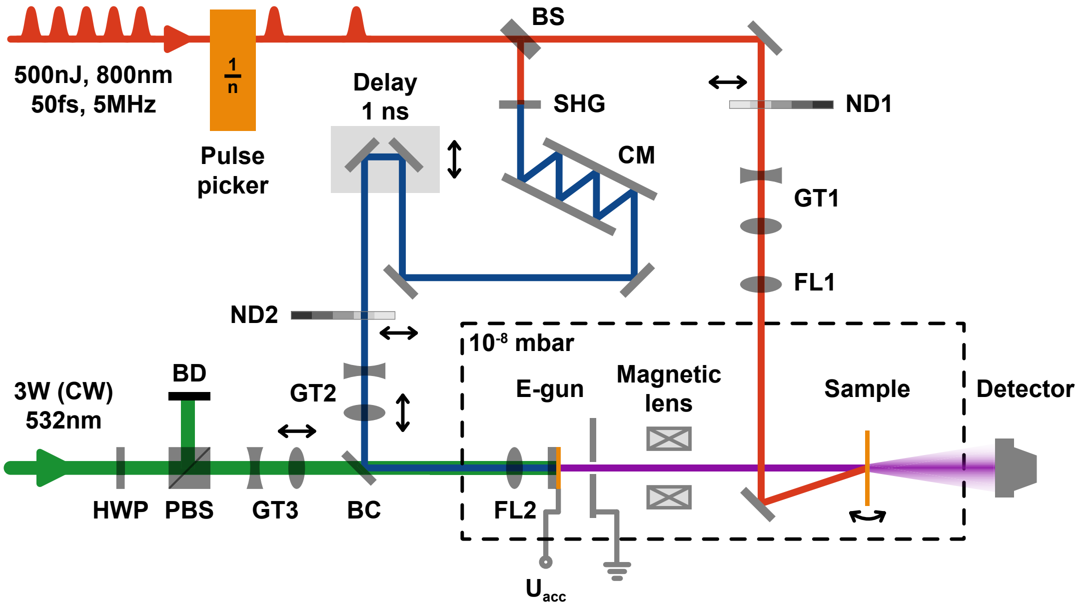

Figure 5.1: Sketch of the single-electron diffraction apparatus used in this work. The laser repetition rate can be set by a pulse picker. After a beam splitter (BS), the probe pulses are frequency doubled (SHG) and compressed (CM). A tight focus (FL2) provides high beam quality from two-photon photoemission inside the thermally stabilized photo-yield single-electron gun (E-gun) operated at 10^{-7} mbar to 10^{-9} mbar. Magnetic lens is used to focus the generated electron beam onto the sample. The pump beam is focused onto the sample and pump-probe diffraction patterns can be recoded with a CMOS active pixel sensor. See text for further details.

5.1.1 Laser sources

The pulsed laser source is a mode-locked titanium sapphire (Ti:Sa) long-cavity oscillator (FEMTOSOURCE™ XL™ 500[1]), providing 500 nJ pulse energy and bandwidth limited pulse durations of 50 fs to 60 fs (FWHM) at a repetition rate of 5.13 MHz and a carrier wavelength of 800 nm. The Ti:Sa crystal is optically pumped with 11.5 W of continuous wave (CW) laser power at 532 nm provided by a COHERENT Verdi V18[2]. As the full output power of the pump laser (18 W) is not required for standard operation, the housing of the Ti:Sa was modified so that an additional CW output with approximately 3 W at 532 nm wavelength is available. This output is used to stabilize electron emission from the photocathode as described in Section 5.2.

For single-electron diffraction experiments, the long-term stability of the entire setup is of major interest. Due to its long optical cavity (≈ 30 m), the beam pointing and chirp

---

[1] FEMTOLASERS Produktions GmbH, Austria, `http://www.femtolasers.com` (Accessed: 24 June 2014)

[2] Coherent, Inc., `http://www.coherent.com` (Accessed: 24 June 2014)

of the Ti:Sa are extremely susceptible to fluctuations of the environmental temperature. Hence, the entire laser was placed in an additional closed housing with an average distance of approximately 10 cm to the laser. This passive shielding damps environmental temperature fluctuations by more than an order of magnitude, resulting in less than ±0.05 K temperature fluctuations within the inner housing. The beam pointing of the output is actively stabilized with a piezo-based alignment system[3], not shown in Fig. 5.1.

5.1.2 Pump-probe optics

The repetition rate of the pulsed laser can be reduced using a pulse picker consisting of a Rubidium Titanyl Phosphate Pockels cell and a subsequent polarizing beam splitter (see Ref. [142] for further details). If set active, the Pockels cell rotates the polarization of individual pulses to make them pass the polarizing beam splitter. Any repetition rate that is a integer fraction of the basic repetition rate can be realized. Achievable suppression ratios are on the order of the order of 1 : 50. After repetition rate modification at the pulse picker, a 90 : 10 beam splitter (BS) generates pump and probe beam. The pulse energy of the pump beam can be adjusted using neutral density filters (ND1) which provide 43 different optical densities (OD) ranging from 0.1 OD to 8 OD. The ND filters used introduce much less dispersion in comparison with a combination of half-wave plate and polarizing beamsplitter. A Galilean telescope (GT1) is used to expand the beam so that a small focus (FL1) can be obtained at the sample without lenses inside the vacuum chamber.

Compared to the setup described in Refs. [2, 142], an improved design for the probing electron beam was developed, providing improved stability, smaller optical foci and shorter optical pulses. Photoelectrons are generated via two-photon absorption which has several advantages in practice (see Section 5.2 for details). The second harmonic of the laser fundamental is generated using a beta barium borate crystal (SHG). At the central wavelength of 400 nm, chirped mirrors (CM) are readily available and are used to compensate dispersion from all following optics. They also act as an efficient high pass filter, removing the fundamental laser wavelength. A delay stage consisting of a retro reflector on a linear motion stage provides a time delay scan range of 1 ns. Tiny misalignments of the retro reflector mostly cause parallel displacement of the beam and have less effect on the angular beam pointing. Parallel beam drifts in the large pump beam might lead to a loss of pump-probe overlap on the sample. However, parallel beam drifts in the probe beam do not affect the electron beam too much, as the high-coherence electron gun concept [2] is based on tightly focusing onto the cathode. Hence, the delay stage is placed in the probe beam path. After passing the delay stage, the probe beam's pulse energy and divergence can be adjusted precisely with ND filters (ND2) and a Galilean telescope (GT2), respectively. A beam combiner (BC) is used to overlap the probe pulse with the aforementioned additional CW output of the FEMTOSOURCE™. The latter can be adjusted in power using a combination of half wave plate (HWP) and polarizing beam splitter (PBS). Excess

---

[3] Aligna®, TEM Messtechnik GmbH, Germany, `http://www.tem-messtechnik.de` (Accessed: 24 June 2014)

laser power is reflected to a beam dump (BD) and the divergence of the transmitted beam is adjusted with a Galilean telescope (GT3). To minimize dispersion effects, the beam combiner is used in reflection mode for the probe beam. The collinear beams pass a viewport of the electron gun (E-gun) chamber which is operated at $10^{-7}\,\mathrm{mbar}$ to $10^{-9}\,\mathrm{mbar}$. The E-gun is described in detail in Section 5.2. The entire optical setup is housed by plastic covers mounted on the optical table which prevents influence from air flow and provides additional thermal decoupling from the lab.

5.1.3 Control of laser parameters for the photoemission process

Two successive two-photon processes are used to generate the electron pulse: SHG and two-photon photoemission. This makes the emission yield highly sensitive to the energy and chirp of the laser pulse. Here, the dependence is derived to allow accurate adjustment of the laser pulse compression at the photocathode. Furthermore the resulting formula allows deconvolution of the effects of laser pulse energy and chirp fluctuations from the photoemission yield using data from a simple in-situ measurement.

The chirp of a laser pulse is described by the group delay dispersion (GDD) introduced by different optics. In the case of the UED probe beam path shown in Fig. 5.1, GDD sources at 400 nm and 800 nm must be treated separately. Assume the electric field of the fundamental laser pulse to be

$$E_\omega(t) = \sqrt[4]{\frac{2P_\omega^2}{\pi\nu^2\tau^2}}\; e^{i\omega t}\; e^{-\left(\frac{t}{\tau}\right)^2} \tag{5.1}$$

with P_ω the laser average power, ν the repetition rate, τ the pulse duration and ω the central frequency. The pre-factor in Eq. (5.1) was chosen so that the integration over the laser intensity $|E_\omega(t)|^2$ is equal to P_ω. Introducing ϕ_ω and $\phi_{2\omega}$, the GDD for the fundamental and the second harmonic respectively, the second harmonic power and the electron yield (number of emitted electrons per pulse) are

$$P_{2\omega} \propto \frac{P_\omega^2}{\sqrt{\tau^4 + 4\phi_\omega^2}}\ , \tag{5.2}$$

$$Y_{\mathrm{PE}} \propto \frac{P_{2\omega}^2}{\sqrt{\tau^4 + 4\left(\phi_\omega + 2\phi_{2\omega}\right)^2}} = \frac{P_\omega^4}{\left(\tau^4 + 4\phi_\omega^2\right)\sqrt{\tau^4 + 4\left(\phi_\omega + 2\phi_{2\omega}\right)^2}}\ . \tag{5.3}$$

Equations (5.2) and (5.3) are peak functions with steep slopes. Hence, to reduce sensitivity to GDD fluctuations, it is crucial to operate the multi-photon processes at minimum GDD. In the fundamental beam path, the GDD can be conveniently controlled with the variable prism compressor built into the FEMTOSOURCE™. In the second harmonic beam path, the chirped mirrors (CM) introduce approximately $-200\,\mathrm{fs}^2$ per reflection. The number of bounces was adjusted to compensate the calculated GDD of all other optics and achieve $\phi_{2\omega} = 0$.

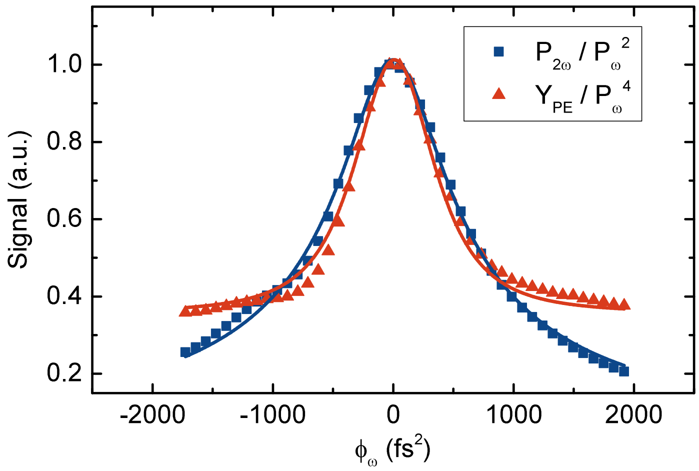

Figure 5.2: SHG and electron yield for different ϕ_ω. The zero-point of ϕ_ω was set for the maximum of $P_{2\omega}$. The measured data (markers) can be fitted nicely with theoretical predictions (lines). The electron yield clearly shows, that both two-photon processes are at maximum efficiency for the same GDD of the fundamental, i.e. the number of bounces on the chirped mirrors accurately compensate for GDD in the probe beam path.

This was checked with a simple measurement, recording P_ω, $P_{2\omega}$ and Y_{PE} for different values of ϕ_ω set by the prism compressor. To extract the GDD dependencies, according to Eqs. (5.2) and (5.3) the values for $P_{2\omega}$ and Y_{PE} were divided by factors of P_ω^2 and P_ω^4, respectively. The result, plotted against ϕ_ω, is shown in Fig. 5.2. Here, the zero-point of ϕ_ω was set for the maximum of $P_{2\omega}$. The fits (lines) using Eqs. (5.2) and (5.3) are in nice agreement with the measured data (markers). Only a very tiny difference in peak position of the two curves can be observed, indicating a well adjusted chirp compensation and a small value for $\phi_{2\omega}$. This is supported by the corresponding fit result of only $(15 \pm 6)\,\mathrm{fs}^2$, which is less than one bounce on the chirped mirrors. Third order dispersion was neglected here and is neither compensated by the prism compressor nor by the chirped mirrors, but might be responsible for the small differences between fits and measured data. Still, the effect is very small so that the probe beam path can be assumed to be well dispersion compensated, providing nearly transform-limited laser pulses at the cathode.

With $\phi_{2\omega} \approx 0$, the dependence of the electron yield on laser parameter is

$$Y_{\mathrm{PE}} \overset{(5.3)}{\propto} \frac{P_{2\omega}^2}{\sqrt{\tau^4 + 4\phi_\omega^2}} \overset{(5.2)}{\propto} \frac{P_{2\omega}^3}{P_\omega^2} \,. \tag{5.4}$$

By simply measuring both laser powers P_ω and $P_{2\omega}$, the relative change in photoemission due to fluctuations in pulse energy and chirp of the fundamental can be calculated from Eq. (5.4). The measured electron intensity can be divided by the derived value to deconvolve laser-related fluctuations from the data. With this simple in-situ measurement, the signal-to-noise of measured electron beam intensity was significantly improved. Note that changes of the laser spectrum are not taken into account by Eq. (5.4), but these were found to be negligible for our laser system.

5.1.4 Electron optics

Due to the energy spread in photoemission (see Section 3.3.3), the beam obtained from the electron gun is divergent leading to beam diameters too large for diffraction. To correct this, solenoid lenses are used to focus the electron beam as discussed in Section 3.3.1. In practice, additional control of the electron's beam pointing is required and can be realized with homogeneous magnetic fields perpendicular to the propagation axis.

An in-vacuum, water-cooled magnetic lens providing focusing and deflecting of the electron beam has numerous advantages and was conceived, manufactured, calibrated and applied as described in the following. Compared to solenoids mounted outside the vacuum chamber, in-vacuum devices can be extremely compact requiring orders of magnitude less electric power. The correspondingly smaller stray magnetic fields generated by the lenses have only minor influence on magnetic field stabilization system discussed in Section 5.1.6. Furthermore, no distortions from shielding effects of the chamber's material are introduced. The perfect thermal insulation of vacuum provides high decoupling from environmental temperature fluctuations leading to high stability of the lens' position. The head of the custom-built magnetic lens combines a typical solenoid for focusing coil and two additional Helmholtz coils for steering the beam. Figure 5.3a shows a sketch of the device especially designed to be mounted on a 3-axis translation stage[4] providing precise positioning of the head along all spatial dimensions. The thermal insulation of vacuum also necessitates efficient cooling of the device, which is very challenging under UHV conditions. Here, this was solved by using an in-vacuum lens mount consisting of two mechanically stabilized pipes for cooling water (flow and return). The pipe coil heat exchanger of the head can be attached to the pipes with two vacuum fittings from Swagelock[5] connectors and provides cooling water flows of 2 L/min. To avoid any remanent field from pole shoes, copper was used for the reels and non-magnetic steel was used for the heat exchanger and the pipes. A technical drawing and a picture of the assembled head are shown in Fig. 5.3b and Fig. 5.3c, respectively. The dimensions of the focusing lens were designed to minimize power dissipation [116] resulting in a power consumption of only 20 W for focusing an electron beam at 60 keV central energy. The Helmholtz coils provide sufficient deflection of the electron beam to cover nearly the entire sensor of the detector and consume negligible power compared to the focusing lens. All three channels can be controlled individually and the temperature of the coil is monitored using a thermocouple sensor. Taking into account the maximum power consumption of the device, the heat capacity of water ($4.2\,\mathrm{kJ\,kg^{-1}\,K^{-1}}$) and the flow of cooling water, the temperature difference in flow and return line can be calculated to be approximately 0.1 K. The corresponding length difference of the two pipes from thermal expansion is less than 100 nm. Hence, position drifts due to

---

[4] customized Vab KPM 12, VAb Vakuum-Anlagenbau GmbH, `http://vab-vakuum.de` (Accessed: 01 July 2014)

[5] Swagelok Company, United States of America `http://www.swagelok.com` (Accessed: 04 July 2014)

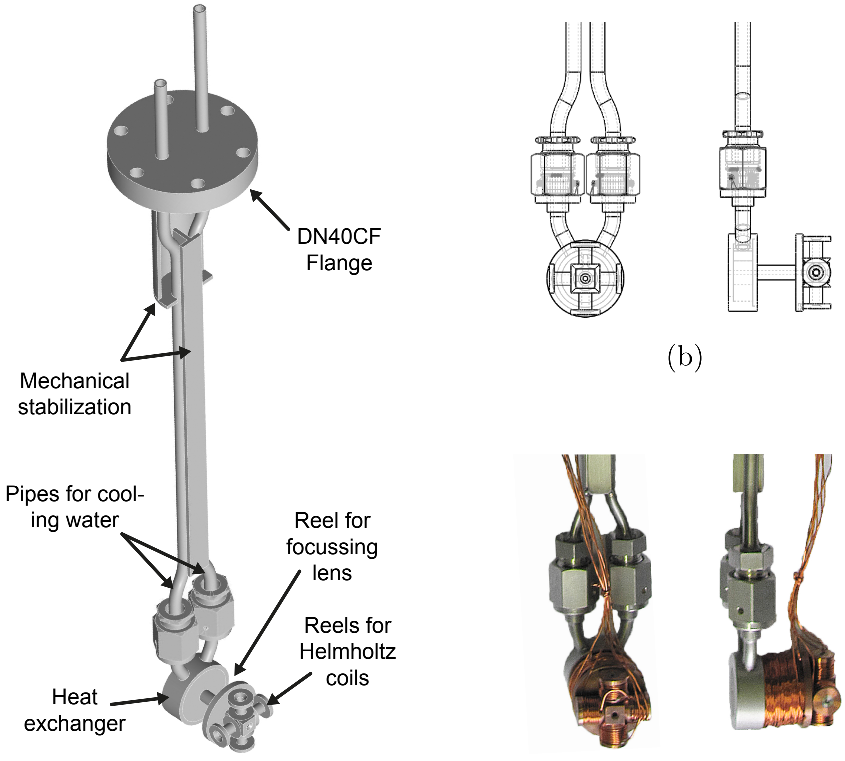

(a) (b) (c)

Figure 5.3: Design (a) of a water-cooled UHV-compatible magnetic lens. The head of the lens is mounted on two pipes with additional mechanical stabilization, which also provide high cooling water flow. The head (b) and (c) consists of one solenoid lens for focusing and a pair of Helmholtz coils for deflection that can be controlled individually. See text for further details.

different operational currents are negligible and there is no latency from thermalization of the system.

This estimate also shows that the temperature stability of the cooling water must be better than 0.1 K. This was realized using a Peltier-based water chiller [6], which provides ±0.01 K temperature stability. This corresponds to position drifts of the magnetic lens of ±10 nm.

---

[6] Thermotek T255P3CR, ThermoTek Inc., United States of America, `http://thermotekusa.com` (Accessed: 01 July 2014)

5.1.5 Sample mount, beam blocker and detector

Sample positioning

Thin film samples in TEM are usually mounted on TEM grids (see Chapter 6 for details). A homemade mount able to hold multiple grids can be attached to the five axis goniometer[7] with 50 mm range in all three spatial dimensions, ±15° of tilt, and continuous panning. These ranges provide convenient remote control of the position of the sample.

Electron beam block

As discussed in Section 2.1.2, only a tiny fraction of the incoming electrons are diffracted, while the rest are concentrated in the transmitted beam. This usually vastly exceeds the dynamic range provided by typical detection schemes including the CMOS detector used here. To avoid damage to the detector, the transmitted beam must be blocked without blocking the diffraction pattern. This becomes challenging especially in the case of limited transverse coherence of the electron beam and diffraction of complex materials with large lattice constants leading to only small distances between the reflections (see Eq. (3.1)).

A beam block design, considering particular needs of single-electron diffraction, was conceived and realized. A sketch of the design and a picture of the assembled device installed in the UED vacuum chamber are shown in Fig. 5.4a and Fig. 5.4b, respectively. A combination of a linear and a rotary feedthrough made of non-magnetic components and with UHV capability provides the basis for the beam block. The feedthrough is mounted perpendicular to the electron beam propagation direction and under 45° with respect to the vertical. A change of the linear feedthrough position leads to a movement illustrated by the blue arrow in Fig. 5.4b. In addition to the fine tuning adjustment, a pull-back of fixed distance provides fast and reliable exit and entry of the beam block with high repositioning accuracy. A miniature gearing (see Fig. 5.4a for details) was designed and mounted at the end of the feedthrough transforming axial rotation into rotation of a thin copper wire around an axis parallel to the electron beam. A tiny paddle at the end of the wire is the actual beam block as illustrated with an artificial electron beam (purple beam in Fig. 5.4a). Its size is designed to reliably block the transmitted beam but to not affect the innermost Bragg reflection for lattice spacings of up to 5 Å at 50 keV. Compared to two-dimensional linear motion feedthroughs, the combination of linear and rotary positioning allows the copper wire to be aligned such that no Bragg reflection is blocked. All components are UHV-compatible and non-magnetic.

---

[7] HUBER Diffraktionstechnik GmbH & Co. KG, Germany, `http://www.xhuber.de` (Accessed: 25 June 2014)

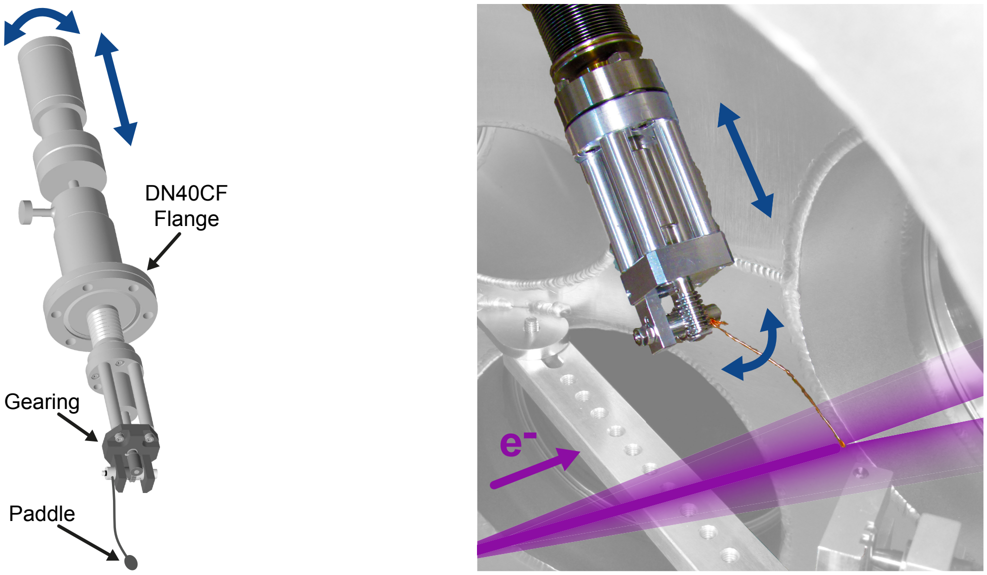

(a) (b)

Figure 5.4: Highly flexible UHV-compatible electron beam block. The conceived design (a) combines translational and rotary motion of a tiny paddle for high flexible beam blocking feedthrough. The built device (b) attached to the UED chamber is positioned to accurately block the transmitted beam of the diffraction pattern.

Detector

The diffraction pattern is recorded using a TemCam-F416[8] which is based on a phosphor screen coupled to a CMOS-based APS. The detector provides a spatial resolution of 16 megapixels distributed over a sensor area of 64 mm × 64 mm with an active pixel size of 15.6 µm. Exposure times can be varied from 0.1 s to 30 s and each pixel is read out with 16 bit dynamic range. The CMOS sensor is operated at 293 K to reduce thermal noise on the image. A detailed discussion of the noise of the setup and especially the detection scheme is given in Section 5.3.

5.1.6 Magnetic field stabilization

One basic prerequisite of any pump-probe experiment is spatial overlap of the pump and probe beam at the sample. Working with electron beams, omnipresent fluctuations in magnetic fields can deflect the beam, thereby leading to a loss in spatial overlap. Measurements show that in the case of the single-electron diffraction apparatus, variations on the order of 40 nT in the magnetic field lead to a peak shift of 1 pixel at the detector, corresponding to relative changes of more than 1 % for large lattice constants (see Eq. (3.1)). Only

---

[8] Tietz Video and Image Processing Systems GmbH, Germany, `http://www.tvips.com` (Accessed: 01 July 2014)

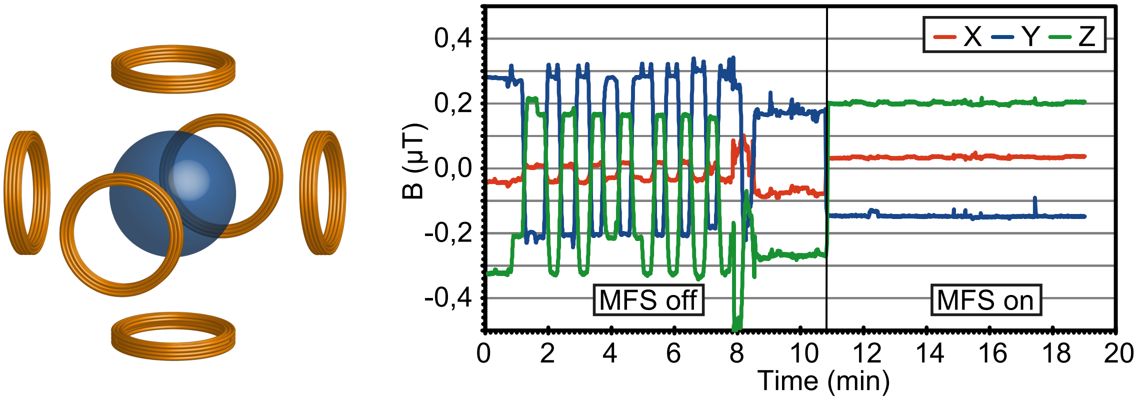

(a) (b)

Figure 5.5: (a) Magnetic field stabilization is realized with three pairs of Helmholtz coils (yellowish coils) , each compensating for changes of the magnetic field in one spatial dimension. In the overlap volume of all the channels (blue sphere), the magnetic field is stabilized in all dimensions. (b) Measurement of magnetic field compensation quality. The time-dependent magnetic field is given for all three spatial dimensions. The intense oscillations from 1 min to 8 min are related to the building's elevator. At $t = 11\,\text{min}$ the magnetic field stabilization (MFS) is switched on. From 11.5 min to 18 min the elevator is moved again, but the magnetic field variations are suppressed with a factor of up to 60.

changes of the field strength during experiments must be avoided; static components, e.g. the geomagnetic field, are not an issue. In the case of single-electron diffraction, long data acquisition periods put high demands on the long-term stability of the magnetic field.

Sources of magnetic field fluctuations close to the experiment can be avoided by working with non-magnetic materials for movable parts and simply moving time-changing sources of magnetic field as far away as possible. Fluctuations from outside the experiment are more difficult to deal with. Typical sources are elevators, forklifts, underground railways and the line frequency of 50 Hz. Power cables and other experimental setups can cause fluctuations. However, these sources are far enough away from the experiment that their magnetic field is approximately constant in space over the experimentally relevant volume. Hence, changes of these fields can be compensated by artificial generation of uniform opposing fields. A sketch of a three-dimensional magnetic field stabilization (MFS) following this idea is shown in Fig. 5.5a. Individually controlled solenoids pairs (yellowish coils in Fig. 5.5a) for each spatial dimension, working nearly at Helmholtz condition, can generate any field vector in the stabilized volume (blue sphere in Fig. 5.5a). The absolute magnetic field vector inside this volume is measured with high precision sensors and an electronic feedback control adjusts the currents for each coil to keep it constant.

The single-electron diffraction apparatus was installed in the volume of three custom-built Helmholtz-like coils, each providing 18 turns with a cross-section of 1.5 mm^2. Applying a driving current of 2 A corresponds to a magnetic field of roughly 2 µT inside the volume. Appropriate amplifiers, including electronic feedback control as well as high precision sensors are commercially available [9]. A measurement from the acceptance certificate [10] is shown in Fig. 5.5b. Triaxial measurement of the magnetic field (B_X, B_Y, B_Z) next to the electron gun is given versus time, while the elevator close to the laboratory was frequently moved on purpose. For the first 11 min, the magnetic field stabilization is switched of (MFS off) and one can clearly identify varying field amplitudes of several hundred nanotesla. After activation of the system (MFS on), the elevator is moved again, but only very tiny variations in magnetic field can be observed corresponding reduction factors of up to 60. The remaining field fluctuations of 10 nT or less are negligible for the experiment.

5.2 Thermally stabilized photo-yield high-coherence single-electron source

For an electron gun capable of single-electron diffraction experiments, three major properties are required. First, the generation of shortest electron pulses at the sample is desirable. Second, a high degree of transverse coherence and focusability is required to be able to investigate complex unit cells and support small sample sizes. And third, the photoemission yield must be stable over typical data acquisition periods, on the order of tens of hours.

5.2.1 First generation single-electron source with high transverse coherence[11]

The transverse coherence is limited by the transverse velocity spread $v_\perp$ (Eq. (3.3)). Due to the absence of space charge in single-electron emission, $v_\perp$ is remarkably low and mainly limited by the photoemission process itself (see Section 3.3.3). As discussed in Section 3.2, the global degree of coherence (GDC) is a conserved quantity in the single-electron regime and reducing the beam diameter linearly increases the GDC. This is another advantage of single-electrons as the emission area is not limited by image charge effects which prohibit emission of dense electron packets [143, 144]. Therefore, minimizing dispersive broadening effects and reducing the emission area at the same time significantly increases the GDC.

Following this concept in a modified electron gun, a global degree of coherence of roughly 3×10^{-4} was achieved [2] by using an focusing lens with only 20 mm focal length and single photon photoemission at 266 nm laser wavelength. This GDC corresponds to a coherence length of approximately 20 nm at the sample which enables observation of materials with large unit cells or even small biological samples [89].

Unfortunately, this first-generation electron gun suffered from two major problems. The short Rayleigh length (less than 200 µm) defines the accuracy in lens position required to reliably focus on the photocathode. Small deviations in position of the focal length were

---

[9] MACOM II®,Müller-BBM GmbH, Germany, `http://www.muellerbbm.de` (Accessed: 04 July 2014)

[10] Measurement performed together with Dr. Gisbert Gralla, Müller-BBM GmbH.

[11] A part of this section is based on the work performed together with Friedrich Kirchner [2].

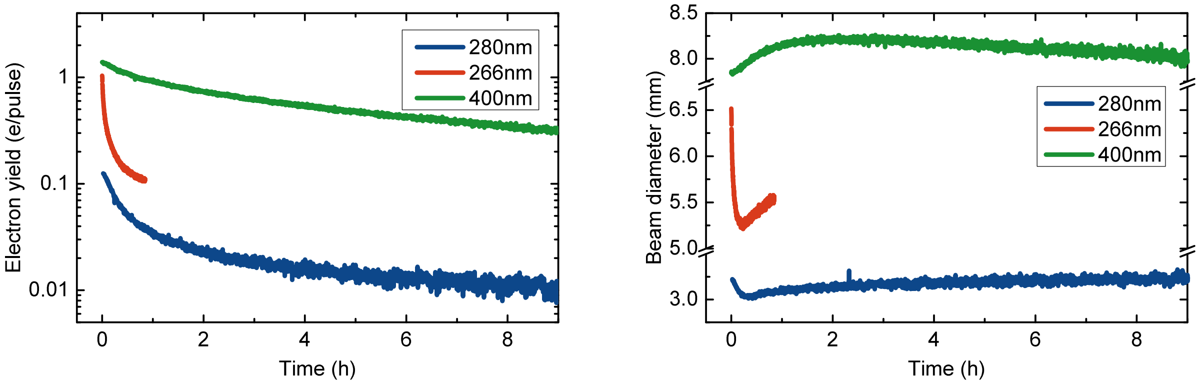

(a) (b)

Figure 5.6: Changes in (a) electron emission yield and (b) electron beam diameter at the screen with time observed for different excitation wavelength. Within a few hours, the yield drops to less than 20 %, insufficient for diffraction experiments using single-electron pulses. The corresponding change in beam diameter indicates changes of the work function due to the aging process.

corrected by changing the beam divergence with an additional lens, e.g. 400 mm focal length at 220 mm distance to the cathode [142]. This cannot be interpreted as a small correction though, and subsequently leads to a significant increase in minimum achievable focus size. Another problem of this electron gun was the limited long-term stability of the photoelectron yield, i.e. electrons per pulse. As mentioned before, typical UED data acquisition times are on the order of tens of hours. Therefore emission yield stability is especially crucial for single-electron diffraction.

In summary, the first generation electron gun successfully demonstrated the concept of high-coherence in the single-electron regime. However, besides the optical deficiencies, which could be corrected rather easily (see Section 5.2.3), the problem of decreasing emission yield was found to be the most crucial limitation preventing time-resolved diffraction studies. The investigation of that problem and an approach to solve it will be discussed in detail in the following sections.

5.2.2 Decay of photoelectron yield

Phenomenon

The change in electron yield over time was measured for wavelengths of 280 nm and 266 nm, generated via tunable-UV [85] and third harmonic generation (THG), respectively. The results are shown in Fig. 5.6a. The intended electron yield of 1 e/pulse could not be achieved with the tunable-UV setup [85, 142]. For both wavelengths the electron yield decreases quickly within the first few hours while a saturation cannot be observed. Figure 5.6b shows fitted beam diameters of the unfocused electron beams at the detector. For both data sets, the beam diameter decreases quickly for awhile but then slowly increases until the end of

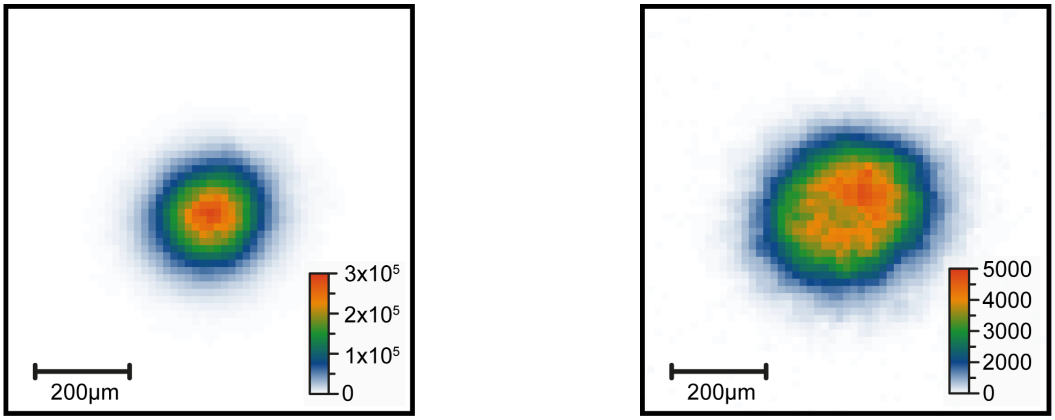

(a) (b)

Figure 5.7: Inhomogeneous photocathode abatement causes the electron beam profile of a new photocathode (a) to change during aging (b).

the measurement. The results for a third data set at 400 nm shown in Fig. 5.6 as well and will be discussed later.

As the acceleration voltage is approximately the same for both measurements (30 kV), the beam diameter can be associated with the work function of the cathode [85]. In general, this is supported by the larger initial beam diameter for observed for the shorter wavelength, which can be explained by a larger kinetic energy spread (see Section 3.3.3). However, the emission profile of the cathode was found to change as aging proceeds. Figure 5.7 shows slightly focused electron beam intensity profiles before (Fig. 5.7a) and after (Fig. 5.7b) cathode aging. Besides the massive decrease in intensity, a change of the beam profile can clearly be observed, indicating faster aging at areas of higher laser intensities. As this was not taken into account for determination of beam diameters shown in Fig. 5.6b, fitted values after significant aging might be distorted artificially.

From several additional measurement series, dependencies of the aging on background pressure, residual gas composition, laser repetition rate and high voltage level clearly could be excluded. However, indications that the aging speed depends on irradiance ($\mathrm{J\,m^{-2}\,s^{-1}}$), were found. Smaller laser beam diameter at the cathode and higher laser average power lead to faster decay of electron yield which is also supported by the observation of inhomogeneous aging across the emission profile (see Fig. 5.7).

Photocathodes whose yield had decayed below 10 % were unmounted for post-damage analysis. The results from measurements with a interference-based profilometer[12] are shown in Fig. 5.8a. A group of four, nearly perfectly round variations on the surface were identified as laser induced damage of different emission areas used. The profilometer measurement shown surface elevations on the order of some tens of nanometers. Laser-

---

[12] Profilometer measurements were performed by Olga Razskazovskaya.

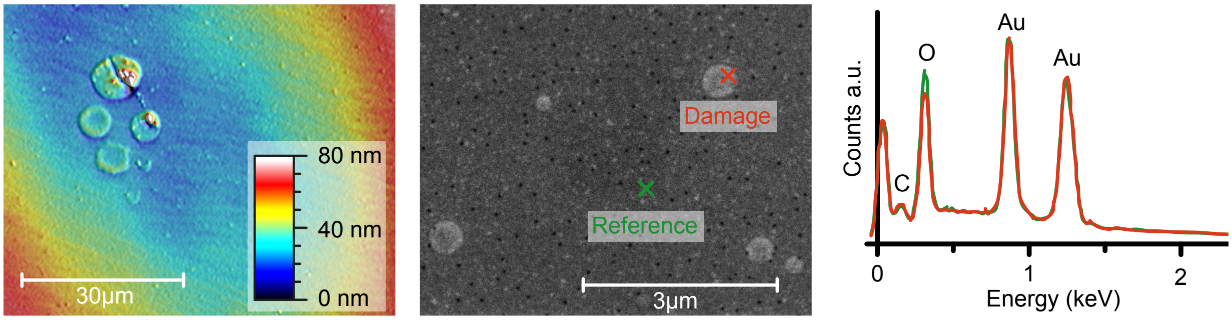

(a) (b) (c)

Figure 5.8: (a) Interference-based profilometry of laser-damaged photocathode. Four damaged spot are clearly observable as elevations of roughly 40 nm. (b) Scanning electron microscopy of another laser-damaged photocathode. Again round surface modification are observed. (c) Energy-dispersive X-ray spectroscopy of reference and damaged spot. No significant change in composition can be observed.

induced surface modifications were also identified by scanning electron microscopy (SEM)[13] as shown in Fig. 5.8b. Note that the cathode investigated by SEM is not the same as the one investigated by profilometry. Similar changes of the surface were observed although their diameter was roughly an order of magnitude smaller. At the marked spots in Fig. 5.8b, energy-dispersive X-ray spectroscopy (EDX) was performed[13]. The results are shown in Fig. 5.8c. Two peaks from the gold coating of the photocathode and additional peaks from carbon and oxygen were identified. As the cathodes were exposed to air after aging, a contamination with carbon and oxygen, e.g. CO_2, is possible. No significant changes in composition were found which is in contradiction to similar studies [145].

In summary, the photoelectron yield deacy was found to depend to some extent on the incident laser irradiance. Furthermore, indications for a coincident increase in work function were observed whereas the subsequent decrease in work function might be related to the inhomogeneous aging of the emission profile. Other dependences could not be found. Profilometry studies indicate laser-induced elevation of the surface but no change in material composition of aged and non-aged photocathode was observed using energy-dispersive X-ray spectroscopy. Both the tight focusing of the laser on the photocathode in the high-coherence electron gun (see Section 5.2.1) as well as laser pulse durations of a few tens of femtoseconds are not common in conventional UED setups. The correspondingly high peak laser intensities might be the reason why similar observations of photoelectron yield decay have not so far been reported in the UED literature. In the following, various processes that can cause a change in electron yield are discussed.

---

[13] SEM and EDX measurements performed by Mag. Lisa Koll, Institute of Materials Science and Mechanics of Materials, Technical University Munich.

Physical mechanism of photocathode aging

Due to the small laser power of approximately 5 µW, melting and evaporation of the gold film can clearly be excluded. However, because of the peak intensities on the order of 10^9 W/cm^2, thin film ablation processes should be considered. Ablation would cause a continuous thinning of the gold layer. As long as the thickness of the photocathode is more than a few times the mean free path length (which is the approximate escape depth of the electrons), increasing emission yield would be observed with decreasing cathode thickness. Falling below this thickness would result in a decrease in emission yield due to less absorption. Thus after a possible initial increase, the electron yield would decrease continuously to zero, without saturating. This lack of saturation is consistent with the observations. However, cathode thinning is not consistent with the results from profilometry and EDX measurements.

The annealing of the polycrystalline gold thin film might explain a significant increase in work function. The work functions of sputtered or evaporated thin films are known to be much smaller than the corresponding bulk material values. In the case of gold for example, the bulk work function is known to vary from 5.3 eV to 5.5 eV [61] depending on the crystal orientation, but Aidelsburger et al. [85] measured 4.3 eV for a thin film cathode. This large difference might be caused by different crystal orientations, crystal defects and/or impurities. Annealing or cleaning (UV bleaching) of the photocathode could therefore induce a convergence of the work function towards the bulk values. If the work function exceeds the available photon energy of 4.7 eV provided by the 266 nm laser pulses, the photoemission yield is expected to be equal to zero. This is in agreement with the observation that no saturation of the decrease occurs. Possible saturation due to annealing was tested using two-photon photoemission with the second harmonic of the Ti:Sa laser (400 nm) providing 6.2 eV of electron energy, which is well above the bulk work function of gold. The results of this measurement are given in Figs. 5.6a and 5.6b. Although the decrease in emission yield is much slower compared to excitation with 266 nm, after 10 h the electron beam intensity nevertheless drops to 10 %. As expected, the beam diameter is larger compared to the 266 nm data sets but shows different temporal behavior. The measurement was repeated for even longer times, but saturation in beam intensity did not occur. A significant decrease in beam diameter as expected for annealing could also not be observed. Furthermore, annealing and/or cleaning mechanisms cannot explain the results from profilometry. Hence, the decrease in electron yield can not be explained by annealing or cleaning mechanisms alone.

Photocathode aging might be explained by gradually increasing contamination of the photocathode surface. This is known to have a significant influence on the work function and thereby on the photoemission yield. Contamination can either be initially present or adsorbed from the residual gas. Initial contaminations could be avoided by in-situ coating of the photocathode in the gun chamber or plasma cleaning the surface. Adsorption of residual gas molecules however, cannot be avoided because surface and surrounding gas equilibrate thermodynamically. The rate of this process decreases for lower pressures and also depends on sticking coefficient and diameter of the residual gas molecules [146]. At vacuum levels of 10^{-7} mbar to 10^{-9} mbar the adsorption of a monolayer of residual gas molecules takes roughly 10 s to 10^3 s [146]. Without baking the vacuum chamber, the major components of the residual gas are water vapor and carbon dioxide. Calculations [147] and experimentally investigation [148] of the influence of water monolayers on the work function of different metals showed an immense effect of up to a few electron volts. Starting with a perfectly clean photocathode, equilibrium should be reached ofter less than 1 h of residual gas exposure. The measured decrease in electron yield does not saturate and the rate of the decrease was found to be laser-dependent.

From the consideration of the previous paragraph, the accumulation of surface adsorbates on its own cannot explain the data. However, a more complex model of contamination taking into account interactions of the intense UV pulses with surface adsorbates might. A "trapping"of molecules at the emission area due to the laser focus is conceivable. In case of pure physisorption, the decrease would be reversible because of the re-establishment of the previous equilibrium between residual gas and adsorbates when the laser is switched off. This was not observed in the measurements. As the photon energies are on the order of bond-dissociation energies of carbon dioxide or water [149] and high enough to split most organic compounds, photo-chemical reactions of the contamination molecules cannot be excluded. Laser-induced bond breaking, i.e. cracking, usually leads to smaller molecules with lower vapor pressure but potentially generated radicals might interact with the surface or physisorbed molecules leading to permanent bonding and contamination. This picture of chemisorption is supported by the profilometry measurements. In contrast to pure adsorption, the resulting change in work function is continuous and irreversible. Starting from a clean surface, layers of organic compounds are known to decrease the work function of pure metals. Therefore in the beginning of the aging process an increase in emission yield is expected. As the layer thickness increases, blocking of photoelectron by additional scattering processes becomes more likely and the emission yield should approach zero. This is not observed in the measurements but could be explained by initial contamination of the photocathode as long as it is large enough. However, a significant increase of contamination specific atoms in the areas exposed to the laser was not observed in EDX measurements (Fig. 5.8c).

In summary, an extremely discouraging decay of the cathode photoelectron yield was identified if working at highly-coherent single-electron emission. The magnitude and rate of this decay prevent any pump-probe experiment in the single-electron regime. Systematic studies were addressed to this problem to locate the underlying physics. Evaporation, ablation and pure physisorption were excluded. It is hypothesized here that an interplay of initial contamination, physisorption and laser-induced chemisorption leads to a permanent deposit which is responsible for photocathode aging. Additional contributions from potential annealing of the emission area must be taken into account as well. This hypothesis is in rough agreement with similar studies [145, 150] identifying carbon content, ex-situ heat treatment, surface adsorbates and gold coverage as parameters of influence for emission yield stability. Note, however, that no dependence of the vacuum level and the residual gas composition was found and the EDX measurements did not show a significant change in material composition, suggesting that the full mechanism may be even more complex.

5.2.3 Concept for stable-yield, high-coherence photoemission

To perform time-resolved diffraction studies, it was imperative to stabilize the electron yield of the photocathode so that the probe pulse maintains its characteristics over the experimental integration time. Based on the results of the previous section, a new photocathode concept was developed.

Optics

To provide photon energies larger than the work function of the potentially annealed photocathode, two-photon photoemission from second harmonic laser pulses at 400 nm central wavelength was established (see Section 5.1.2 for further details). Depending on the actual amount of annealing and increase of work function, one might also work with the third harmonic (266 nm) reducing the kinetic energy spread. However, the contributions from annealing are unknown and laser pulse compression and characterization is challenging at this wavelength. Furthermore, the non-linearity in laser intensity of the two-photon photoemission process (see Eq. (5.3)) provides simple and precise optimization of focus size and chirp (see Section 5.1.3) at the cathode which is very convenient in practice. The disadvantage of larger fluctuations in photoemission due to the higher order photon process (fourth instead of third order) can be compensated by measuring the power of the fundamental and the second harmonic and correcting the intensity using Eqs. (5.2) and (5.3).

For the new electron gun design, a lens (FL2) with a focal length of only 14.3 mm at 400 nm wavelength was embedded in the electron gun providing a smaller focus diameter on the photocathode. The global degree of coherence should therefore be even larger than the value of 3×10^{-4} measured by Kirchner et al. [2]. As mentioned in the introduction to Section 5.2, minimal focus sizes can be achieved only for very accurate positioning of the lens, in this case better than 100 µm. Therefore, the exact position of (FL2) was calculated and shims were used to iteratively optimize the distance between lens and cathode inside the electron gun while measuring the electron yield for different laser divergences. Once a precision of less than 100 µm is reached, the optical focus can be placed exactly on the photocathode by adjusting GT2. Gaussian beam ray-tracing was used to optimize the entire focusing geometry (GT2, FL2 and photocathode).

Cathode heating

Photocathode emission yield was shown to be stabilized by exposure of the photocathode to high intensity UV light at high oxygen partial pressure [150]. However, this kind of UV cleaning is not feasible during a UED measurement. A novel approach to prevent adsorption and/or permanent chemical bonding of residual gas compounds, is heating of the emission area of the cathode. Heating of a surface increases both the mobility of the molecules on the surface and their probability to desorb. This is commonly used in thin film deposition technology to control layer growth. Heating by a few hundred kelvin should be suffice to avoid adsorption of residual gas components.

However, permanent heating of a photocathode at up to 60 kV is challenging. Installation of a resistive heater is very complex, because it requires high-voltage insulation and high thermal conduction at the same time. Furthermore, resistive heating introduces additional magnetic fields. Heating of the entire gun and its vacuum chamber is also excluded, as thermal stress on the construction might lead to beam instabilities. To this end, a CW laser was chosen to selectively heat the area of photoemission of the gold thin-film (roughly 10 μm^2). For wavelengths above 500 nm, the absolute absorption of a 20 nm thick gold film is around 20 % [151] and the additional output of the FEMTOSOURCE™ could be used as heating laser (see Fig. 5.1). It is aligned collinear with the femtosecond laser and its power and divergence can be adjusted as described in Section 5.1.2 providing temperature control and tunable beam diameter at the photocathode. The photon energy of 2.3 eV is well below the work function of the photocathode and multi-photon photoemission is impossible considering the low peak intensity. To achieve both spatial overlap of heating and probe laser at the photocathode and sufficient heating of the emission area, the beam diameter of the heating laser at the cathode is set a few times larger than the probe laser focus. Note that due to the different wavelength, the focal length of FL2 differs for the heating laser. Again Gaussian ray-tracing simulations were used to optimize the optical setup.

To estimate the required power, laser heating of the photocathode was simulated based on the finite element method (FEM). A typical cathode used in the high-coherence electron gun consists of a fused silica substrate with 6.25 mm in diameter and 1 mm thickness. A gold film with a thickness of approximately 20 nm is sputtered on the entire front surface and acts as the actual photocathode. The combination of substrate and coated photocathode was provided by LayerTec[14] and is mounted in a gap on top of the high-voltage mount of the electron gun [142]. A model of the cathode was built with a finite element software package[15] and is shown in Fig. 5.9. Laser heating was simulated as a continuous heat source corresponding to the laser dimensions. As the transmission of the thin film is on the order of several 10 % and the film thickness is similar to the mean free path length of excited electrons, the heat source is assumed to be homogeneous in the excited volume of the thin film. In FEM simulations, dealing with structures whose dimensions span many orders of magnitude is very challenging. Meshing the entire model with a mesh size corresponding to the smallest structure of the model easily leads to an impracticably high number of mesh elements. Substrate and thin film therefore cannot be simulated completely. For large distances to the heat source however, the heat transfer along the thin film can be neglected compared to that into the substrate. Hence, only a portion of the gold film a few times larger than the heat source was simulated (see inset in Fig. 5.9). The heat sink due to the cathode mount was simulated with a correspondingly dimensioned ring of copper. Considering an incident laser power of 200 mW at the cathode, the peak temperature was calculated to be around 500 °C (see Fig. 5.9). In this model, ideal thermal conduction

---

[14] LAYERTEC - optische Beschichtungen GmbH, Germany, `https://www.layertec.de` (Accessed: 17 July 2014)

[15] COMSOL Multiphysics®, COMSOL Inc., United States of America, `http://www.comsol.com` (Accessed: 10 July 2014).

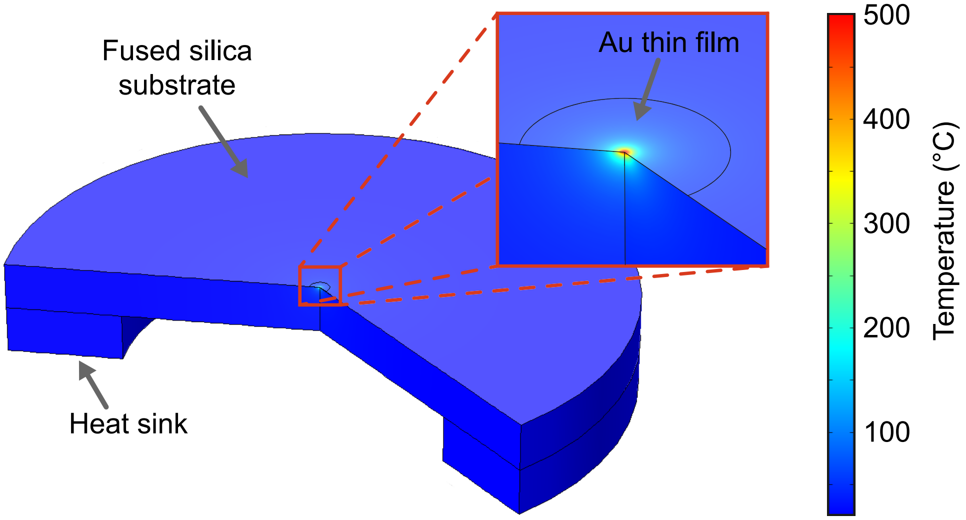

Figure 5.9: Model and results from a FEM calculation on laser heating of the photocathode. To limit the number of mesh elements, only a small slab of the thin film on top of the substrate is simulated. For 200 mW of incident laser power the temperature distribution on the cathode is shown in the inset peaking at roughly 500 °C.

between thin film and substrate as well as substrate and heat sink was assumed. Additional thermal resistance along the model might lead to higher temperatures. However, the results provide an order of magnitude for the required laser power.

In summary, simulations show that sufficient heating of the photoemission area can be achieved by focusing an additional CW laser onto the cathode. The order of magnitude of required laser power was estimated to a few hundred milliwatts of incident power. This is not extraordinarily high and can for example easily be provided by the additional CW output of the laser system used here. However, heated of the photocathode can lead to unwanted thermal electron emission, which would contribute spuriously to the recorded diffraction pattern. Therefore the amount of thermal emission must be accurately characterized.

5.2.4 Characterization of the new single-electron gun

Spatial overlap of laser beams on the photocathode

To provide reliable heating of the photoemission area, heat and pump beam must be overlapped on the cathode. Thermal emission generated from the heated cathode can be used to accomplish this. Simultaneously overlapping of the beam from thermal emission with that from photoemission on the detector generates overlap at the photocathode as well. The achievable precision is demonstrated in Fig. 5.10. To obtain sufficient thermal emission, the incident laser power was set to 450 mW measured at the entrance of the electron gun chamber. The resulting beam is shown in Fig. 5.10a. Note that according to

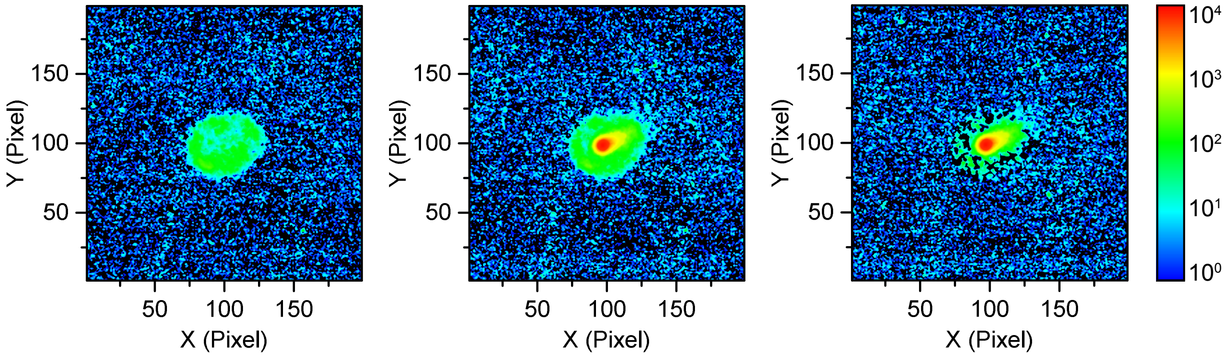

(a) (b) (c)

Figure 5.10: Spatial overlap of heating laser and probe laser at the cathode is realized by overlapping thermally emitted electrons and probe electrons at the detector. As the fields defining the electron trajectories are identical, this assures the overlap at the cathode. (a) shows the thermal emission and (b) shows both beams simultaneously. To characterize the probing electron beam alone, a differential image (c) is generated.

simulations, 450 mW of incident laser power should heat the gold film close to its melting point. However, possible losses due to the fact that the anti-reflection coatings on the viewport and focusing lens are not designed for 532 nm as well as reflections from the substrate were not taken into account in the simulation. The thermal emission was stable over hours, indicating that the peak temperature at this setting is still far too small for evaporation of the gold film. The combination of thermal emission and photoemission is shown in Fig. 5.10b. The accurate overlap of the two beams as well as reliable heating of the entire photoemission area due to larger heating beam diameter is demonstrated. The intensity is given in logarithmic scale and the integrated intensity of thermal emission is roughly one order of magnitude smaller than that of photoemission. However, the photoelectron yield of the pulsed beam was reduced to less than 0.01 e/pulse to avoid saturating the camera. In consequence, working at 1 e/pulse the contribution from thermal emission is less than 0.1 %. Therefore variations of the electron flux from thermal emission and their influence on the signal-to-noise ratio of the pulsed electron beam are negligible. Figure 5.10c shows the differential image of Figs. 5.10a and 5.10b demonstrating the small focal size of the photoelectron beam at the detector. It was measured to be on the order of a few tens of microns.

Emission stability

After obtaining spatial overlap of heating laser and probe laser at the photocathode following the aforementioned procedure, the long-term stability of the electron yield was studied. Starting from an initial value of approximately 1 e/pulse, electron beam intensity as well as the laser powers P_ω and $P_{2\omega}$ were measured over more than 10 h. The electron yield was

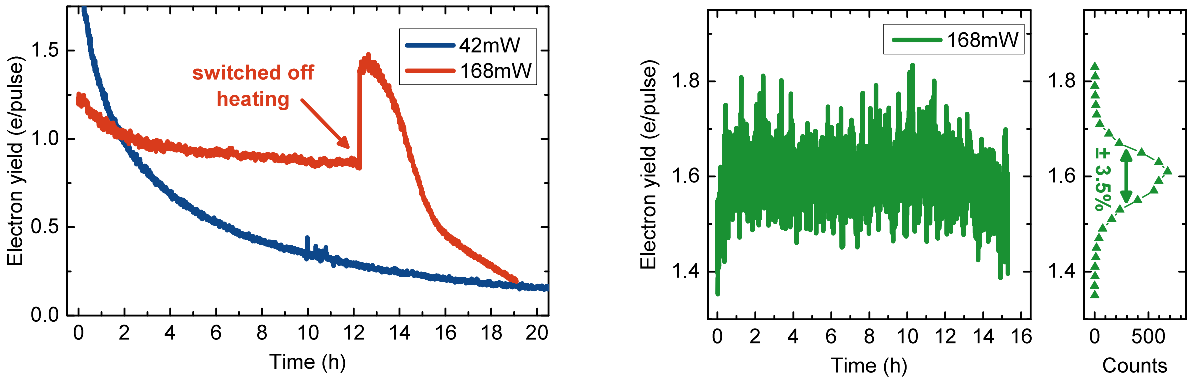

(a) (b)

Figure 5.11: (a) Long-term measurements of the laser-corrected electron emission yield for different heating powers. Insufficient heating power (42 mW) slows down photocathode aging whereas sufficient heating power (168 mW) leads to stable emission yield. Switching off the heating, aging continues. (b) Determination of the standard deviation of laser-corrected electron yield defining the stability of the electron source.

calculated from the measured beam intensity and corrected according to Eq. (5.4) (see Section 5.1.3). Results for different incident heating laser powers, measured at the entrance of the electron gun chamber, are shown in Fig. 5.11a. At an incident power of approximately 40 mW (blue line in Fig. 5.11a) a 90 % decrease in electron yield is observed in 20 h. This is significantly slower compared to the measurement without heating where -90 % was observed after 10 h (compare Fig. 5.6a). Increasing the heating power to approximately 170 mW (red line in Fig. 5.11a) leads to a nearly stable electron yield over many hours. Switching off the heating (marked with the red arrow in Fig. 5.11a) after roughly 12 h, the electron yield instantaneously increases by 50 %, but then decreases rapidly within a few hours. This clearly demonstrates the feasibility of cathode heating for electron yield stabilization. Further measurements indicate that the required heating power for stable emission depends on the desired intensity of the pulsed electron beam.

The emission yield of another, previously unused cathode with CW heating on was recorded for more than 15 h, shown in Fig. 5.11b. The integration time of the camera was 1 s. After a small increase in the first hour, the yield remains constant. The distribution shown in the right inset in Fig. 5.11b is Gaussian with a standard deviation of 3.5 %, defining the image-to-image long-term stability of the electron gun at the chosen integration time. Suitable vacuum levels for stable operation of the electron gun were found to be the range of 10^{-7} mbar to 10^{-9} mbar. All of the following experiments were performed with this cathode and no aging was observed over the many weeks of frequent usage.

In summary, laser driven heating of a gold photocathode was demonstrated to stabilize the electron emission yield. The achieved superior stability of this novel electron gun concept is the crucial advance enabling time-resolved diffraction studies using single-electrons.

5.2.5 Expected temporal resolution

The principal contributions to the instrument response function (IRF) is dispersive broadening (see Section 3.3). Due to the two-photon photoemission process at 400 nm, excited electrons gain more than 6 eV of energy. Furthermore, contributions from the high temperature of the cathode due to laser heating are not negligible. Both induce a significant kinetic energy spread of the photoelectrons leading to dispersive broadening on the order of a few hundred femtoseconds for single-electron pulses. The next most important contribution to IRF is mismatch of the pump and probe pulse fronts at the sample. The pump pulses, driving the dynamics of interest in the sample, are untilted because introducing pulse front tilt would induce unacceptable losses in pump irradiance. In the single-electron diffraction apparatus, the incident angle of the pump beam with respect to the electron beam is approximately 16°. For $U_{\mathrm{acc}} = 30\,\mathrm{kV}$ and beam diameters of 75 µm at the sample [1], the mismatch in arrival time is 70 fs at a diffraction angle of 0°. According to Eq. (3.12), ideal phase matching is achieved for a sample tilt of approximately 5°. However, the sample tilt is given by the required diffraction angle, i.e. the angle between the electron beam and the sample surface, which is defined by the zone axis desired for the specific diffraction experiment. Hence, if the required sample tilt is not equal to 5°, the phase mismatch between the pump and probe beams represents a major limitation in achievable temporal resolution. The remaining contributions to IRF are negligible: Timing jitter of the electrons from the photoemission process was estimated to less than 10 fs as discussed in Section 3.3.1. The stability of the high-voltage power supply is specified to be better than 10^{-5} corresponding to less than 20 fs timing jitter at 5 kV/mm and a distance of $l_{\mathrm{AS}} = 0.5\,\mathrm{m}$ (estimated from Eq. (3.9)). Temporal distortions from the solenoid lens are present, as the the solenoid is not adjustable along all axes and isochronic setting is not provided by the geometry of the vacuum chamber. However, the resulting increase in pulse duration is below $< 30\,\mathrm{fs}$ [117, 123].

Achieving the shortest single-electron pulse durations is not the essential part of this work but could be realized by integrating a pulse compression stage [131, 141] with the apparatus. Nevertheless, the estimated temporal resolution of a few hundreds of femtoseconds was confirmed by laser-based streaking measurements in a comparable beamline [2] and is comparable to typical UED setups working with compressed multi-electron pulses. Hence, the apparatus described here enables proof-of-principle studies of time-resolved single-electron diffraction, as well as studies of structural dynamics with temporal resolution of a few hundred femtoseconds without complex compression methodology.

5.3 Signal-to-noise analysis of the electron detection scheme[16]

5.3.1 Expected signal-to-noise ratios for intensity measurements

To evaluate the intensity of a Bragg reflection, a region of interest (ROI) is defined around the reflection and the values of the pixels in the ROI are summed up. This sum generally consists of the number of diffracted electrons N_e and a background value B caused by the camera. The measurement is repeated K times and the averaged intensity is

$$\overline{I_\mathrm{BS}} = \frac{1}{K}\sum_{k=1}^{K}\left(N_{\mathrm{e},k} + \frac{B_k}{\zeta}\right) = \overline{N_\mathrm{e}} + \frac{\overline{B}}{\zeta} \tag{5.5}$$

with ζ the proportionality constant of the detetctor in counts per electron. $\overline{I_\mathrm{BS}}$ is given in units of electrons. Its standard deviation is

$$\sigma_{\overline{I_\mathrm{BS}}} = \frac{1}{\sqrt{K}}\sqrt{\sigma_{N_\mathrm{e}}^2 + \frac{1}{\zeta^2}\sigma_B^2} \tag{5.6}$$

with σ_{N_e} and σ_B the standard deviations of N_e and B, respectively.

CMOS chip working principle and background noise

The background signal B is a characteristic of the camera. The camera used in the single-electron diffraction apparatus is a CMOS-based active-pixel sensor (APS). The sensor is a two-dimensional array of pixels where each pixel's circuit equivalent is a capacitor in parallel with a photodiode. At the beginning of image acquisition, the capacitor is charged. Photons that are absorbed by the diode during integration discharge the capacitor. The light intensity can be determined by reading out the voltage of the circuit after integration. To provide fast data acquisition times, the read-out procedure can determine the values of an entire row of pixels simultaneously [153]. A detailed description of CMOS based APS is given by Tian [154]. Due to the high complexity of real APS pixel circuits, many different noise sources must be considered [154]. However, to estimate the cumulative standard deviation σ_B, a simplified picture emphasizing three major contributions is used. First, the thermal agitation of the charge carriers in the photodiode generates thermal noise σ_th. This contribution is proportional to the square root of the integration time [155] but can be reduced by cooling the CMOS chip. Second, variations in surrounding electromagnetic fields during the read-out of the pixels can inducing currents to the circuits thereby distorting the read data[17]. As the read-out of a CMOS chip is done row by row [153], the read-out noise σ_r is equal for every pixel in the row. In contrast to thermal noise, the amplitude

---

[16] The experiments discussed in this section were performed together with Bachelor student Theresa Urban [152].

[17] Private communication with Mr. H. R. Tietz, Tietz Video and Image Processing Systems GmbH, Germany.

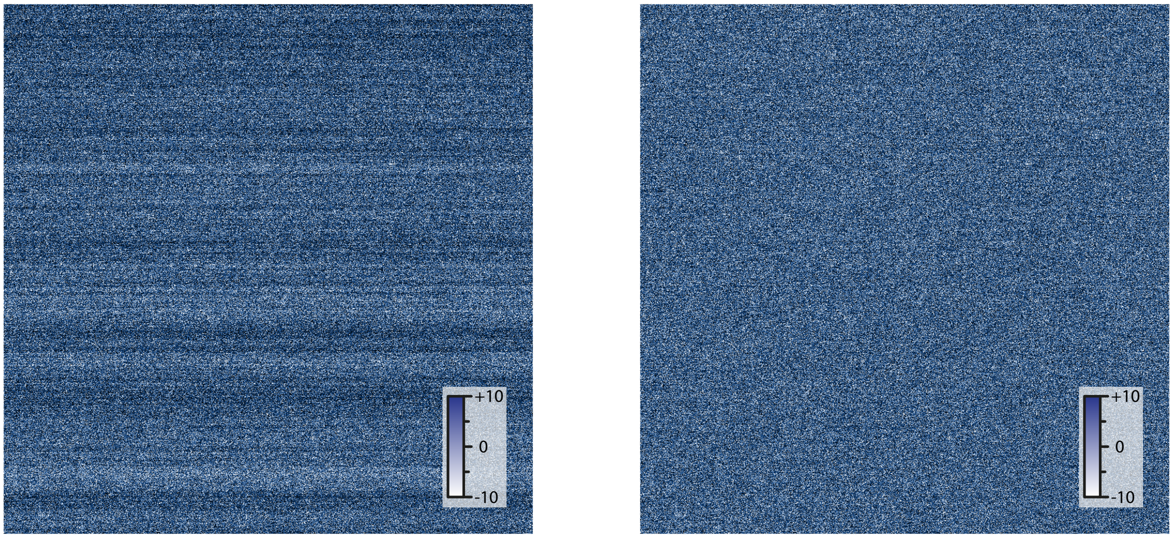

(a) (b)

Figure 5.12: (a) Read-out noise of the detector leads to line by line pixel value offsets. (b) Same image but with average row values subtracted. The line pattern vanished demonstrating that row noise affects an entire row.

of the read-out noise is independent of the integration time. Figure 5.12a shows a typical dark image of the cooled camera. A line pattern from read-out noise is clearly observable. Subtracting the average values of each line from the corresponding pixels, read-out noise σ_r vanishes as shown in Fig. 5.12b. This correction procedure only works for dark images and σ_r must be taken into account when analyzing diffraction patterns. Third, as every pixel has its own amplification, each pixel has a slightly different offset sensitivity. Whereas the latter can be calibrated by illuminating the entire chip with a homogeneous signal (so-called *flat-fielding*), the offset causes a fixed pattern on the chip. The resulting fixed pattern noise can be eliminated by subtracting a dark image from signal images, which is known as correlated double sampling. This also eliminates the average background signal $\overline{B}$. The bias value of the entire chip can vary as well. For one pixel, statistical fluctuations of the bias cannot be distinguished from thermal noise. Hence, it need not be considered as a separate noise source and is assumed here to be included in σ_th.

From the above considerations, the standard deviation of the background signal is

$$\sigma_B = \sqrt{n_\mathrm{r} n_\mathrm{c} \sigma_\mathrm{th}^2 + n_\mathrm{r} n_\mathrm{c}^2 \sigma_\mathrm{r}^2} \tag{5.7}$$

with n_r and n_c the numbers of rows and columns that form the ROI [152]. σ_B is given in counts. By careful noise analysis of multiple dark images recorded at 0 °C sensor temperature, Urban [152] determined the thermal noise at 1 s integration time and the read-out noise as $\sigma_\mathrm{th} = (4.5 \pm 0.1)$ counts and $\sigma_\mathrm{r} = (0.8 \pm 0.1)$ counts, respectively.

Electron beam noise

The standard deviation of the number of detected electrons mainly consists of fluctuations of the electron source σ_{gun} (see Fig. 5.11b) and shot noise σ_{SN} (see Section 2.1.2). Fluctuations in photoemission can be described as

$$\sigma_{\mathrm{gun}} = \eta \overline{N_{\mathrm{e}}} \tag{5.8}$$

with η the relative deviation of the electron source which can be easily determined experimentally (see Fig. 5.11b). In Section 5.2 this was determined to be on the order of a few percent. The shot noise σ_{SN} was defined in Eq. (2.5). Hence, the standard deviation of N_{e} is

$$\sigma_{N_{\mathrm{e}}} = \sqrt{\sigma_{\mathrm{SN}}^2 + \sigma_{\mathrm{gun}}^2} \overset{(2.5)}{\overset{(5.8)}{=}} \sqrt{\overline{N_{\mathrm{e}}} + \eta^2 \overline{N_{\mathrm{e}}}^2} \;. \tag{5.9}$$

Signal-to-noise

The SNR is defined as signal over standard deviation (see Eq. (2.4)). Taking into account $\overline{B} = 0$, the SNR for the intensity of a Bragg spot is

$$SNR_{\mathrm{BS}} = \frac{\overline{N_{\mathrm{e}}}}{\sigma_{\overline{I_{\mathrm{BS}}}}} \overset{(5.7)}{\overset{(5.9)}{=}} \sqrt{K} \left(\underbrace{\eta^2}_{\text{gun}} + \underbrace{\frac{1}{\overline{N_{\mathrm{e}}}}}_{\text{SN}} + \underbrace{\frac{n_{\mathrm{r}} n_{\mathrm{c}} \sigma_{\mathrm{th}}^2 + n_{\mathrm{r}} n_{\mathrm{c}}^2 \sigma_{\mathrm{r}}^2}{\overline{N_{\mathrm{e}}}^2 \zeta^2}}_{\text{camera}} \right)^{-\frac{1}{2}} \;. \tag{5.10}$$

To maximize SNR_{BS}, the ROI should be as small as possible in order to minimize contributions from the camera. However, these contributions are negligible compared to shot noise (SN) for $\overline{N_{\mathrm{e}}} > 100$ and the size of the ROI does not matter. For $\overline{N_{\mathrm{e}}} \gtrsim \eta^{-2}$ the stability of the electron source (gun) is the limiting contribution. However, the relative deviation of the electron source η is not a fixed value but depends on the experimental conditions and is expected to drop with the square root of the integration time. For a UED experiment with single-electron, the electron flux (e/s) of each Bragg spot is determined by the scattering cross section of the sample (see Section 2.1.2) and the repetition rate of the laser. The latter is limited, which will be discussed in Chapter 6. $\overline{N_{\mathrm{e}}}$ and σ_{th} are proportional to the integration time of the camera whereas the the read-out noise σ_{r} remains constant. If the latter can be neglected, Eq. (5.10) clearly shows that increasing the integration time and increasing the number of averaged patterns K is equivalent.

From a single diffraction pattern, the average number of diffracted electrons $\overline{N_{\mathrm{e}}}$ for a specific Bragg reflection can be estimated. Hence, if the noise characteristics of the electron source are known, the number of images required to achieve a specific SNR in the experiment can be estimated from Eq. (5.10). Considering a ROI of 25 pixel × 25 pixel, the known proportionality constant[18] of $\zeta = 60$ counts/e at 30 keV and perviously determined values for σ_{th}, σ_{r} and η, achievable SNR were derived for different values of N_{e} and K.

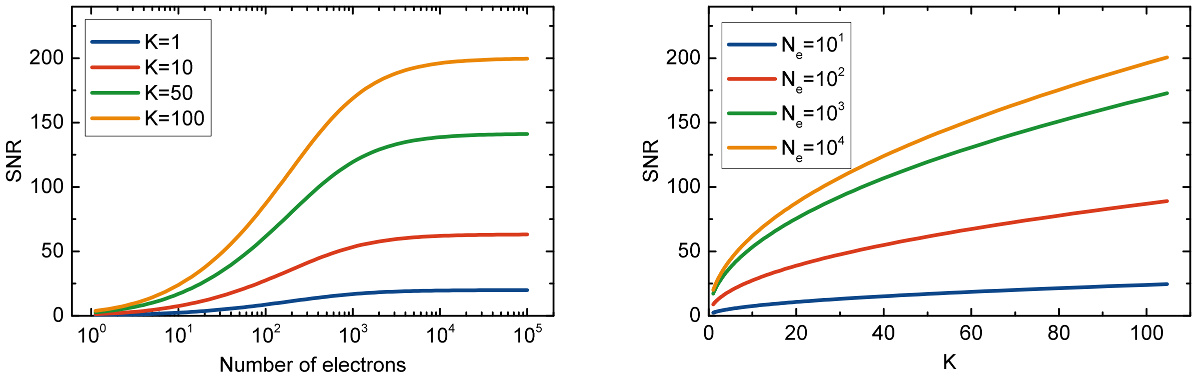

(a) (b)

Figure 5.13: (a) Predicted SNR calculated from Eq. (5.10) for different number of images K that are averaged. N_e values of more than 10^3 do not increase the SNR as it is limited by η. (b) Predicted SNR for different numbers of electron contained in the observed Bragg reflection. Averaging over more images increases the SNR continuously.

The results are shown in Fig. 5.13. In the case of varying number of electrons contained in the Bragg reflections, as shown in Fig. 5.13a, the saturation caused by the limited source stability η can be observed for N_e larger than $1000\,e$. In this regime, the SNR does not increase with more detected electrons but with averaging over K measurements. This effect is also visible in Fig. 5.13b giving the SNR for various values of K. Both plots show that the single-electron diffraction apparatus theoretically provides SNR of more than 100 with sufficient averaging.

In summary, the single-electron diffraction apparatus is expected to provide sufficient signal-to-noise ratios for time-resolved studies, as determined by the criterion derived in Section 2.1.2. For typical parameter values, SNR of 100 are achievable by averaging only 50 images. If read-out noise can be neglected, the increase of SNR from longer acquisition times for a single pattern is equivalent to the increase from a larger number of recorded patterns that are averaged. Achievable SNR values can be estimated from Eq. (5.10).

5.3.2 Signal-to-noise analysis under realistic conditions[19]

Achievable SNR were measured at diffraction patterns from the organic charge-transfer salt potassium tetracyanoquinodimethane (K-TCNQ) [156]. Due to its semiconductor properties [157, 158] K-TCNQ is an interesting compound for realizing molecular electronics [4, 156]. Hence, understanding photo-induced processes of K-TCNQ [7] is highly desirable.

---

[18] Personal communication with Mr. H. R. Tietz, Tietz Video and Image Processing Systems GmbH, Germany.

[19] The production of thin film samples from K-TCNQ discussed in this section was performed together with Master student Alexander André [156].

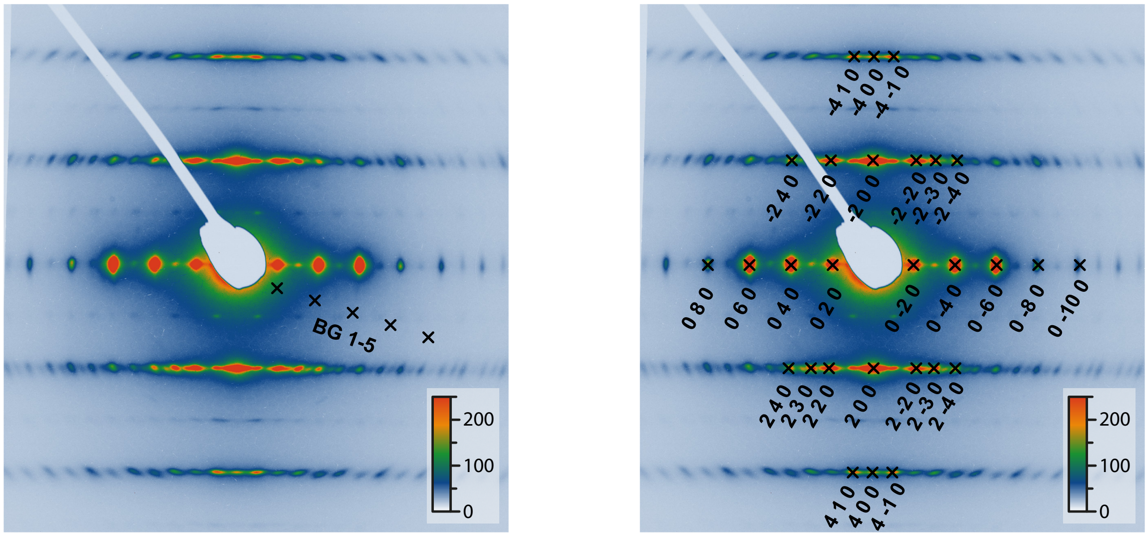

(a) (b)

Figure 5.14: Averaged electron diffraction pattern of K-TCNQ recorded with the single-electron diffraction apparatus. The many observable diffraction orders indicate both, degree of high-coherence and sample quality. To analyze achievable SNR, several ROI for (a) inelastic background and (b) Bragg reflections of different intensity were evaluated.

The feasibility of investigating of K-TCNQ using single-electron diffraction was studied by André [156]. Single-crystals of K-TCNQ were grown with an advanced diffusion technique [156]. Samples with a thickness of roughly 40 nm were produced using ultramicrotomy, which will be discussed in Chapter 6. Static diffraction patterns, i.e. without pump, of these thin films were recorded at roughly 10 e/pulse. The measurement series consists of more than 200 diffraction images with 5 s integration time each. CDS was used to eliminate fixed-pattern noise and average background contributions. The averaged diffraction pattern is shown in Fig. 5.14. The many observable diffraction orders (see Fig. 5.14a) indicate the high quality of the single-crystalline thin films. Only small distortions in terms of rotational blurring are visible, probably caused by crystal damage from ultramicrotomy. The complex diffraction pattern of K-TCNQ was identified by numerically simulating the diffraction pattern[20].

To span a wide range of intensities, ROI's of 25 pixel × 25 pixel were defined around several Bragg reflections and in the inelastic background as shown in Fig. 5.14b and Fig. 5.14a, respectively. The laser corrected mean intensity and standard deviation were derived for all recorded diffraction images and the SNR was calculated using Eq. (2.4). The results (blue squares) are shown in Fig. 5.15. As a fundamental physical limitation to SNR, the shot noise limit ($\eta = 0$, $\sigma_\mathrm{r} = 0$ and $\sigma_\mathrm{th} = 0$ in Eq. (5.10)) is plotted as the green dashed

---

[20] CrystalMaker™ and SingleCrystal™, CrystalMaker Software Ltd., United Kingdom, `http://www.crystalmaker.com` (Accessed: 16 July 2014).

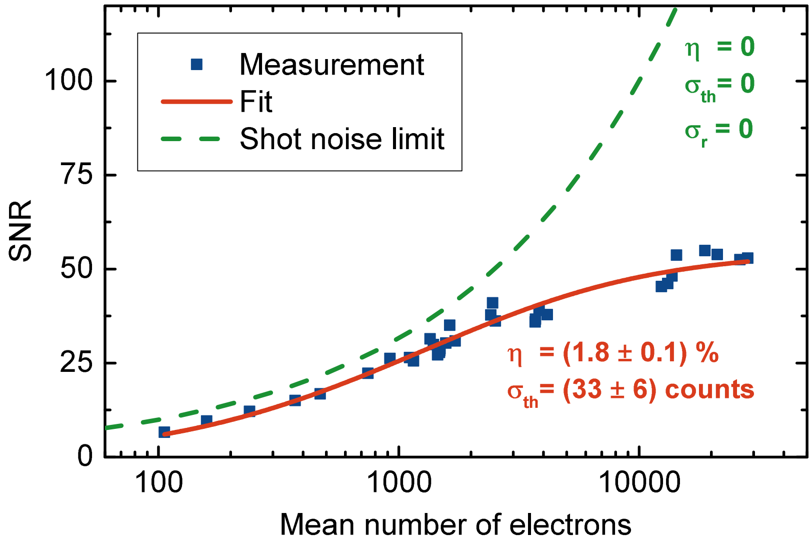

Figure 5.15: Determined intensities for the ROI defined in Fig. 5.14. For low mean number of electrons, the measured SNR (blue squares) are close to the shot noise limit (green dashed line). For large mean number of electrons the measured SNR is limited by the photoemission stability. η and σ_{th} are determined by fitting Eq. (5.10) (red solid line) to the data.

line. For small numbers of electrons, the achieved SNR is close to the shot noise limit. The deviation can be explained by camera noise contributions. For larger values of $\overline{N}_{\mathrm{e}}$, the actual SNR is much smaller than the shot noise limit. This is related to a non-zero source stability η. The measured data points were fitted with Eq. (5.10) for $K = 1$ (red line). ζ and σ_{r} were assumed to be constant values, wheres η and σ_{th} were fitting parameter. As the images were taken at an integration time of 5 s, the previously determined value for $\eta = 3.5\,\%$ (see Fig. 5.11b) is assumed to be reduced by a factor of $\sqrt{5}$. This is in good agreement with the fitted value of $(1.8 \pm 0.1)\,\%$. Considering the five times larger integration time, the thermal noise is expected to be around 10 counts. The fitted value of (33 ± 6) counts is significantly higher but might be explained to a higher temperature of the detector.

In summary, the noise contributions of the camera are negligible even for weak Bragg reflections. Hence, the SNR for weak Bragg reflections are close to the shot noise limit. In contrast, the finite source stability η of the electron source turns out to be the major noise contribution for intense Bragg reflections. The good agreement of the data with Eq. (5.10) demonstrates the feasibility of estimating achievable SNR on that basis. This allows prediction of the required measurement time for recording atomic motions in the material under study, before starting the actual experiment. This possibility will avoid explorative studies with potential failure in the future, and can therefore help making single-electron diffraction a more versatile methodology for complex materials.

Chapter 6

Sample preparation for single-electron diffraction

In Section 3.1.1 appropriate electron energies for diffraction experiments were found to be in the range from 10 keV to 300 keV. Due to the high diffraction efficiency of electrons (see Chapter 1) typical mean free path lengths are in the range of 10 nm to 100 nm [159], e.g. 31 nm for Carbon at 30 keV. This means that feasible sample thicknesses in transmission geometry are three orders of magnitude less than achievable beam diameter (see Section 5.2.5) [1, 2]. Samples that are significantly smaller than the electron beam size lead to a reduction in effective electron flux, decreasing the signal-to-noise ratio (SNR). Hence, free-standing nanometer thin samples with diameters of several tens of microns are required for transmission electron diffraction experiments.

Besides the challenging aspect ratio, the sample must withstand 10^9 pump-probe cycles at $1\,e$/pulse to achieve sufficient SNR (see Section 2.1.2). This not only limits single-electron UED to highly reversible processes but also requires operation at much higher repetition rates than conventional UED setups. Preparation methods for crystalline thin films are discussed in Section 6.1. A versatile optical setup for sample characterization is discussed in Section 6.2. The reversibility criterion and effects of high repetition rates are discussed in Sections 6.3 and 6.4, respectively.

6.1 Preparation of free-standing nanoscale crystalline thin films

Many different sample preparation techniques have already been developed for transmission electron microscopy to produce free-standing, crystalline thin films. Different materials require different preparation techniques and a variety of techniques were used to prepare samples for single-electron diffraction in this work. In general, the techniques can be grouped into two different approaches discussed in the following sections.

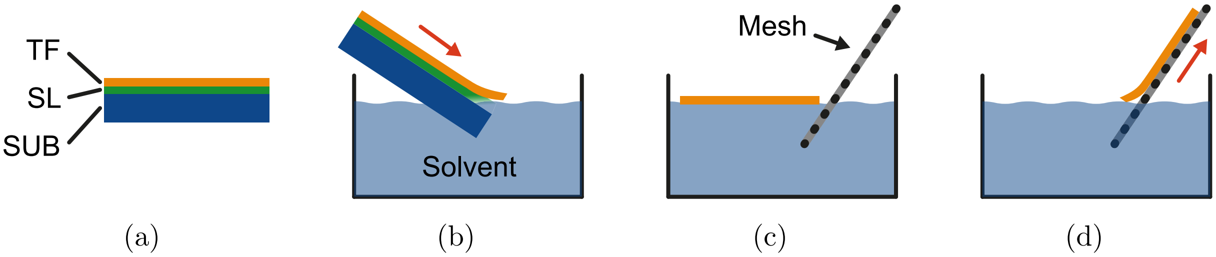

(a) (b) (c) (d)

Figure 6.1: Sacrificial layer method. (a) The substrate (SUB) is coated with a sacrificial layer (SL) and thin film (TF). (b) The substrate is slowly slid into a solvent, removing the SL. (c) Due to surface tension, the TF floats onto the solvent and can be picked up with a mesh as shown in (d).

6.1.1 Bottom-up technique

Using preparation techniques that follow the bottom-up approach, the thin film is directly deposited onto an appropriate substrate. Nanometer film thickness has been demonstrated for a variety of different deposition techniques and with high reproducibility. The most common techniques are based on deposition from the gas phase. In physical vapor deposition (PVD) [160], the target material is sputtered or evaporated under vacuum and subsequently transported to the substrate where it is deposited. All processes involved are purely physical. In contrast, chemical vapor deposition (CVD) [161] takes advantage of a chemical reaction between the surface of the substrate and the gas to produce the desired deposit. Both techniques have been demonstrated as reliable tools for preparation of large-area crystalline or even single-crystalline thin films. However, for UED, free-standing films are required, so these techniques can only be used if there is a means to separate the film from the substrate.

Sacrificial layer method

One way to produce free-standing thin films from deposited layers is the sacrificial layer method, which is well established at the Technological Laboratory (TecLab) of LMU and illustrated in Fig. 6.1. In a first process, the substrate (SUB) is coated with a thin sacrificial layer (SL) on which the actual thin film (TF) is deposited (Fig. 6.1a). At the Technological Laboratory for example, water-soluble soaps, organic compounds (e.g. Betaines) or salts (e.g. NaCl) are used as the sacrificial layer. After deposition, the ensemble is slowly slid under an angle into a container filled with a solvent (Fig. 6.1b). This solvent only dissolves the SL and must provide high surface tension. The latter is important to make the TF float on the liquid when the SL is dissolved (Fig. 6.1c). Subsequently, a mesh can be pushed into the container and careful extraction will cause the TF to lay on the mesh (Fig. 6.1d). At the Technological Laboratory the sacrificial layer method is mainly used to produce free-standing thin films on large frames (several square centimeters) as targets for particle acceleration experiments. Figure 6.2a shows such a frame supporting a free-standing aluminum thin film of less than 100 nm in thickness but nearly 10 mm diameter.

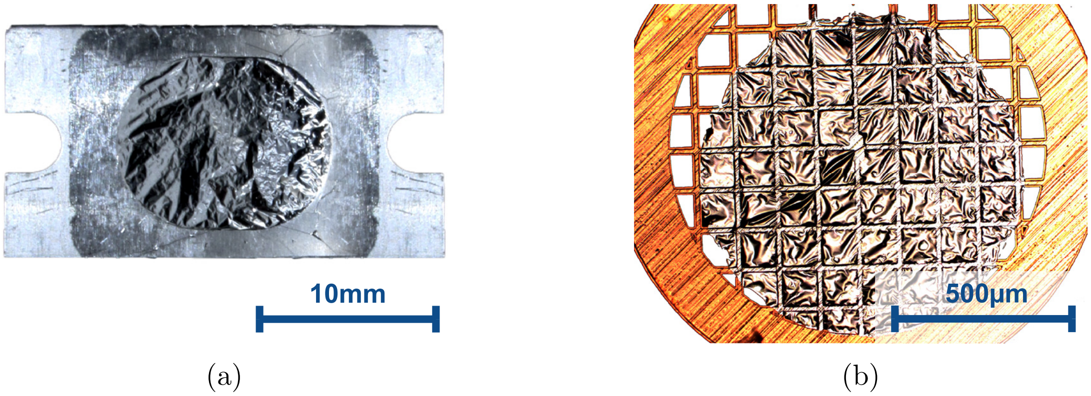

(a) (b)

Figure 6.2: (a) Photograph of an aluminum thin film with less than 100 nm thickness on a large frame. The diameter of the free-standing membrane is around 8 mm. (b) Bright field microscopy image of an 50 nm aluminum thin film on a 100 mesh TEM grid.

Due to the large size, the membrane is not entirely flat which is problematic in time-resolved experiments. For transmission electron microscopy however, typically TEM grids [162] are used as sample mounts. Together with D. Frischke[1], the sacrificial layer method was optimized for mounting samples on TEM grids by using coating masks according to the grid diameter. Figure 6.2b shows a 50 nm thin film on a TEM grid with 100 mesh, i.e. a grid with 100 bars per inch. Due to the periodic mechanical support, the flatness of the membrane is significantly increased.

Selective etching

Another technique to produce free-standing thin films from deposited layers is selective etching. This is illustrated in Fig. 6.3. Before depositing the actual thin film (TF), the substrate is coated with an additional thin etch-blocking layer (EBL) as shown in Fig. 6.3a. The EBL is made of a different material but typically made of a similar compound or thin enough to adapt the crystal structure of the substrate. After deposition of the actual thin film, a masked dry or wet etching process (Fig. 6.3b) selectively etches the substrate material and therefore stops at the etch-blocking layer (EBL). Hence, the thin film is not affected. An additional selective etching process (Fig. 6.3c) is used to remove the EBL, generating a free-standing thin film. This technique was used in the framework of a collaboration with the group of Professor Amann at the Walter Schottky Institut, Munich. Single crystalline, free-standing thin films of the semiconductor indium phosphide (InP) were produced. A transillumination microscopy image[2] is shown in Fig. 6.4a. The bright slits are 30 nm thin membranes of InP. Whereas the marked ones are intact, the other four membranes shown are damaged (bright spots and/or slits). A static diffraction pattern is

---

[1] D. Frischke, Technological Laboratory of LMU, Germany.

[2] Microscopy image was performed together with Master student Alexander André [156].

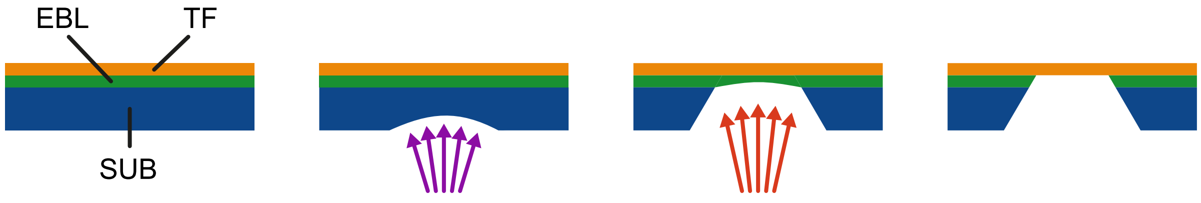

(a) (b) (c) (d)

Figure 6.3: Selective etching method. (a) The substrate (SUB) is coated with an etch-blocking layer (EBL) and a thin film (TF). (b) An etching process that selectively etches the substrate but not the EBL is applied. (c) Another etching process selectively etching only the EBL is applied. (d) After selective etching is completed, a free-standing thin film is generated.

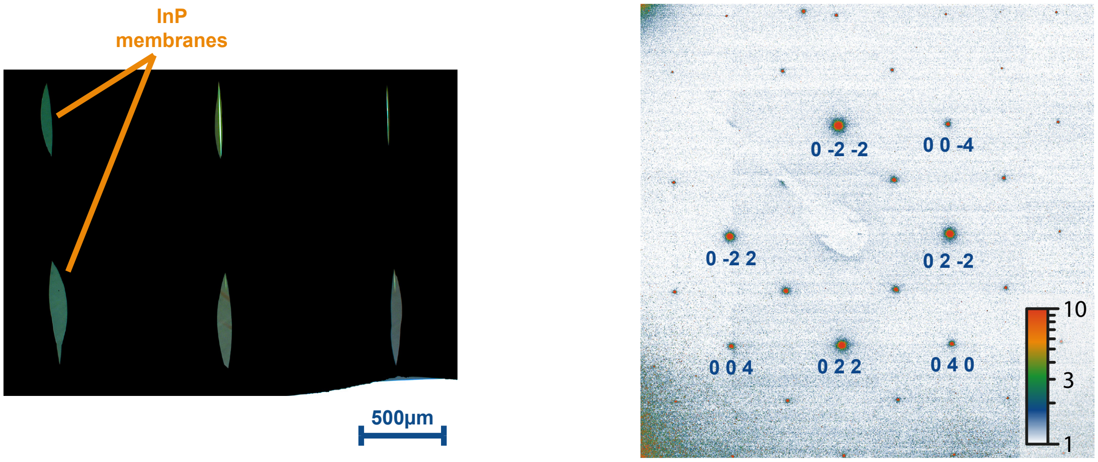

(a) (b)

Figure 6.4: (a) Transillumination microscopy image of InP membranes produced by selective etching. Due to etching process and applied masks, the membranes have a slit shape. Bright areas on the membranes indicate damage of the thin film. (b) Static diffraction image recorded with the single-electron diffraction apparatus. The sharp Bragg reflections and the many observable diffraction order indicate both, high transversal coherence of the electron beam and high crystallinity of the membranes.

shown in Fig. 6.4b. The crystal orientation was determined by numerically simulating the diffraction pattern[3] of InP and comparing it with the measured data. The high crystallinity of the thin films is demonstrated by the many observable diffraction orders.

6.1.2 Top-down technique

In contrast to the bottom-up technique with direct growth of the thin film, the top-down approach starts from a macroscopic single-crystal. The latter can be grown easily with high quality using well-known and established procedures discussed in the following. The most simple technique is to work with supersaturated solutions. By introducing a seed crystal and causing supersaturation by temperature or evaporation of solvent, large single-crystals can be grown. One of the most common technique however, is crystal growth by freezing the material from its liquid phase, which is used for the production of silicon wafers for example. By applying zone melting, extremely pure crystals can be grown. Deposition techniques such as PVD and CVD (see Section 6.1.1) can also be used to grow single-crystals of large scale with high purity. Another widely-used technique is to utilize diffusion of a reagent through a semipermeable membrane with subsequent precipitation of the product. This technique was used in collaboration with André [156] to produce high-quality K-TCNQ single-crystals. A custom-made diffusion apparatus was developed and by varying parameters, e.g. the concentrations of the involved solutions, the crystallization process was optimized. A microscope image of a typical crystal is shown in Fig. 6.5a.

Whereas crystal growth is relatively simple, the main challenge using the top-down technique is the production of thin film samples from the grown crystals. Although as before preparation techniques have been developed for TEM, the extraordinary large lateral sample diameter required for UED is demanding.

Focused ion beam

One technique is to use a focused ion beam (FIB) and cut a lamella from the bulk material [162]. This lamella can be transferred to a TEM grid. However, FIB also leads to ion implantation, which is highly undesirable in UED. Furthermore, producing FIB lamellas with sufficient diameter is challenging. Therefore this technique cannot be used, although it is common in TEM.

Ultramicrotomy

A more gentle technique is ultramicrotomy (UM) which uses a sharp knife to cut off a thin sections of the macroscopic sample. This technique has been used for decades in TEM [162] and is illustrated in Fig. 6.6. In the first step (Fig. 6.6a), the sample is mounted on the movable sample holder of the ultramicrotome. A large variety of different sample mounts are available due to the many different fields of application for this preparation

---

[3] CrystalMaker™ and SingleCrystal™, CrystalMaker Software Ltd., United Kingdom, `http://www.crystalmaker.com` (Accessed: 16 July 2014).

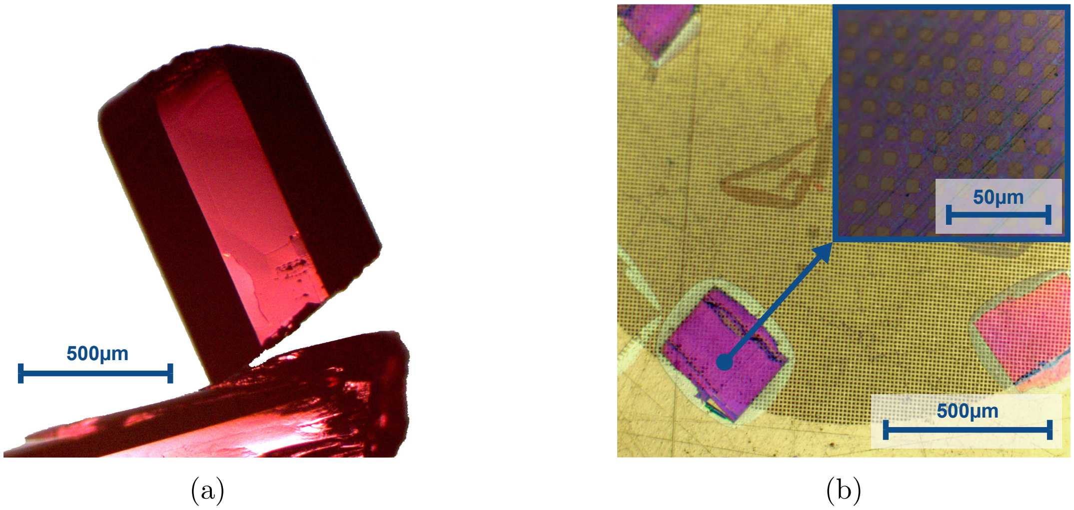

Figure 6.5: (a) K-TCNQ single-crystals grown by André [156]. The large diameter of 0.5 mm and the smooth surface of the crystal indicate high crystallinity. (b) Thin films (purple rectangles) of the K-TCNQ single crystal sectioned by ultramicrotomy and transferred to a 2000 mesh TEM grid. Several sections were placed on the grid. A larger magnification of one of the thin films is shown in the inlet. Only minor damage (grooves) from sectioning is observed.

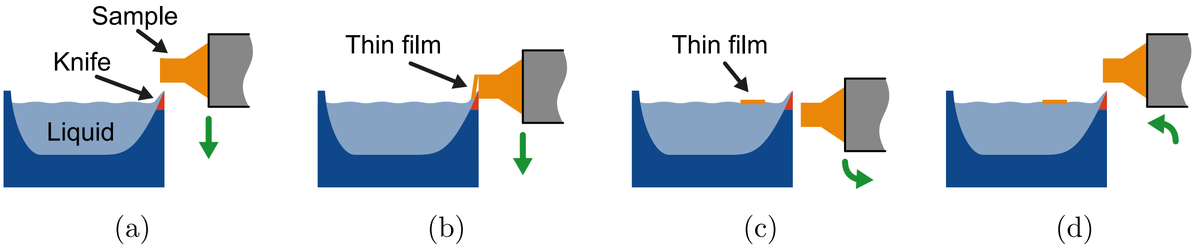

Figure 6.6: Functional principle of ultramicrotomy. The sample is mounted above a diamond knife (red triangle) which is attached to a fixed container of liquid (a). As the sample is moved downwards (b), a section is sheared off the crystal and floats onto the liquid (c) due to surface tension. The sample mount is retracted, moved upwards and feed (d) by the amount of the desired film thickness. The process can be repeated continuously and the thin films can be transferred to TEM grids.

method. Normally, tiny objects are embedded into a resin to provide adequate mechanical stability. However, this is generally not suitable for sensitive crystals. A new sample holder was therefore designed allowing the crystal to be attached to the mount using super glue. A drop of glue encloses the crystal and provides sufficient mechanical stability. Note that the sample material must not be soluble in or reactive with the glue. After mounting, the surface of the sample is positioned above an extremely sharp diamond knife, which is attached to a fixed container filled with liquid. Depending on the surface tension of the liquid, the fill level is chosen carefully to barely wet the knife. By moving the sample holder downwards with a controlled velocity a thin section is sheared of the sample by the diamond knife (Fig. 6.6b). This velocity, typically in the range of 0.1 mm/s to 100 mm/s, is one of the most crucial parameters in ultramicrotomy and needs to be determined individually for every sample. It also strongly depends on the desired film thickness. The sample mount is retracted from the knife while the thin film floats on the liquid's surface (Fig. 6.6c). In the last step, the sample mount is moved upwards again and then forward by an arbitrary amount, i.e. the film thickness. Feed values of less than 20 nm were realized. For sectioning, the hardness of the knife must be larger than that of the sample. With a diamond knife, there are no general constraints on sample material. However, only a few liquids can simultaneously provide wetting of the knife and sufficient surface tension to float the thin film. Typical liquids are water (H_2O) or dimethyl sulfoxide (C_2H_6OS). As the liquid must not dissolve the thin film, it turns out to be the most limiting constraint in conventional UM. Besides the liquid-based UM described, techniques for working at cryogenic temperatures are also available.

Ultramicrotomy was performed on a K-TCNQ single crystal (see Fig. 6.5a) using a state-of-the-art ultramicrotome[4] and a diamond knife[5]. No embedding was used. The solubility of this compound in water was estimated to be small enough to provide enough time to safely transfer the sections to a TEM grid [156]. As shown in Fig. 6.5b, several K-TCNQ thin films (purple rectangles) with thicknesses below 50 nm were successfully sectioned and transferred to a 2000 mesh TEM grid. The inset shows the homogeneous sample quality over more than 100 µm. The observable grooves in the thin film are related to the cutting process. However, these films are adequate for UED which is demonstrated by the diffraction pattern shown in Fig. 5.14.

Another demonstration of the feasibility of UM for UED sample preparation is given by the production of large thin films from N-(triphenylmethyl)-salicylidenimine (MS1) [65, 163] single-crystals. The structural formula of MS1 is shown in the inset of Fig. 6.7a. From spectroscopy in solution, MS1 is known to show a excited state intramolecular proton transfer (ESIPT) which plays an important role in understanding stability, functionality and dynamics of biomolecules [66]. Although spectroscopic studies have been performed on many different ESIPT molecules, a direct observation with UED is very desirable and might lead to additional insight into the real space dynamics of ESIPT. MS1 was synthesized and

---

[4] Leica EM UC7, Leica Microsystems GmbH, Germany, `http://www.leica-microsystems.com` (Accessed: 23 July 2014).

[5] ultra 35°, Diatome AG, Switzerland, `http://www.diatome.ch` (Accessed: 23 July 2014).

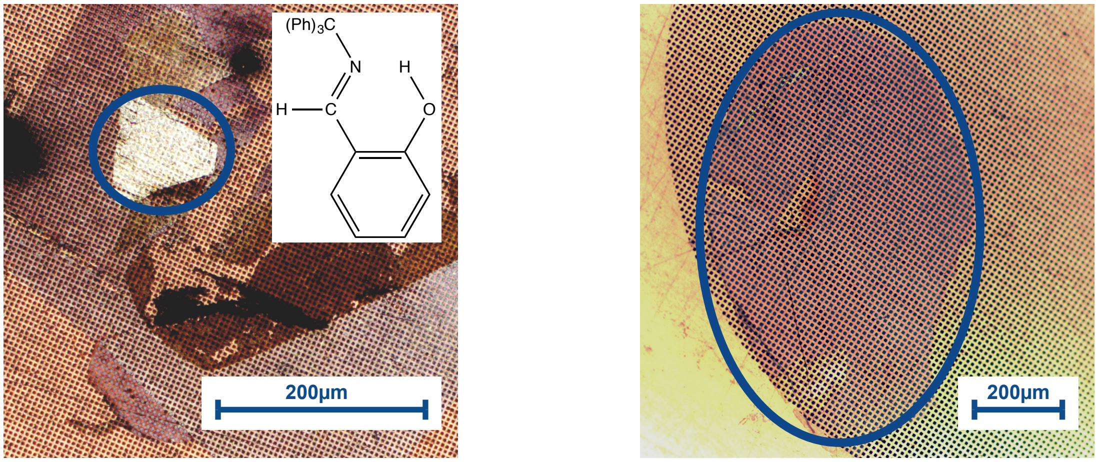

(a) (b)

Figure 6.7: Single-crystalline thin films of MS1 produced by ultramicrotomy. (a) UM sections of an embedded crystal of MS1. Besides many fragments of sample material and resin, an intact area of a free-standing thin film can be observed (bright triangular in blue ellipse). (b) UM section of a non-embedded crystal. The thin film has a diameter of several hundreds of microns.

crystallized by the group of Professor Lewanowicz[6] in Wrocław. Due to the high crystal quality, thin films with 30 nm to 50 nm thickness and a diameter of 100 µm were produced by ultramicrotomy. The different results for embedded and un-embedded crystals are shown in Fig. 6.7. The UM section of an embedded crystal (Fig. 6.7a) consists of many fragments of broken crystal material and embedding material. However, a single-crystalline thin film of triangular shape can be observed (highlighted by the blue ellipse). Using the custom made sample mount to circumvent the embedding process, much larger sections with several hundreds of microns could be produced as shown in Fig. 6.7b. The feasibility of MS1 as a sample for single-electron diffraction was investigated together with Bachelor student Marina Hoheneder [164]. The results are discussed in Section 6.3.

Exfoliation

Another technique to produce thin films is exfoliation, which can be used for materials with layered crystal structures such as graphite or mica, for example. A typical exfoliation process is illustrated in Fig. 6.8. In the first step (Fig. 6.8a), the crystalline bulk sample (BS) is stuck in between two layers of a flexible sticky tape (ST) that are arranged parallel to the basal planes of the crystal. To ensure proper sticking the ST layers are carefully compressed. In the second step (Fig. 6.8b) the ends of the ST are pulled apart gently. Due to its layered crystal structure, the bulk material separates into two parts one sticking to

---

[6] Prof. A. Lewanowicz, Institute of Physical and Theoretical Chemistry, Wrocław University of Technology, Poland

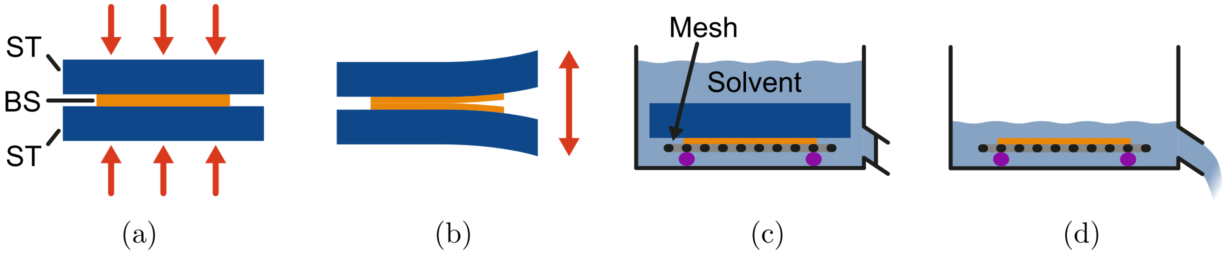

Figure 6.8: Functional principle of exfoliation. (a) The bulk sample (BS) is placed in between two layers of sticky tape (ST) and carefully compressed as illustrated by the red arrows. (b) The sticky tape is pulled apart very gently. These steps are repeated until only a thin film of the BS remains. (c) ST and thin film are transferred to a TEM grid and the ST is solved. (d) The solvent is removed carefully and the free-standing thin film remains on the grid.

each ST layer. The separation of the ST is the most crucial step of exfoliation as good results are only observed for very slow and steady motion. Mechanical apparatus can be used[7] to achieve very slow motions, extending the exfoliation process to hours or even days. Continuous thinning of the layers sticking to the ST is achieved by repeating the first two steps iteratively. When the required film thickness is achieved, the thin film and sticky tape are attached to a mesh and placed in a container of solvent (Fig. 6.8c) to remove the ST. After dissolving the ST, careful removal of the solvent provides a free-standing thin film (Fig. 6.8d). Exfoliation has been successfully demonstrated to produce relatively large thin films of graphene [165] for example. However, the applicability of this techniques is limited to samples with a layered crystal structure.

Exfoliation was used to produce graphite thin films[8] from highly ordered pyrolytic graphite (HOPG). To transfer the thinned film from the sticky tape to TEM grids a intermediate step had to be performed. A 2000 mesh TEM grid was attached to the thin graphite layer using a special glue[9] and subsequently the sticky tape was removed. To remove the remaining Crystalbond, acetone was used as solvent. A typical result is shown in Fig. 6.9. Due to mechanical stress during the production process, different thicknesses occur. However, domains with appropriate thickness and area for UED experiments are available (red ellipse in Fig. 6.9). Diffraction of these thin films will be discussed in Chapter 7.

---

[7] Private communication with B.Sc. Marina Hoheneder, Walter Schottky Institut, Munich.

[8] Sample preparation was performed together with student assistant Matthias Redies.

[9] Crystalbond 509, SPI Supplies / Structure Probe, Inc., United Stated of America, `http://www.crystalbond.com` (Accessed: 23 July 2014).

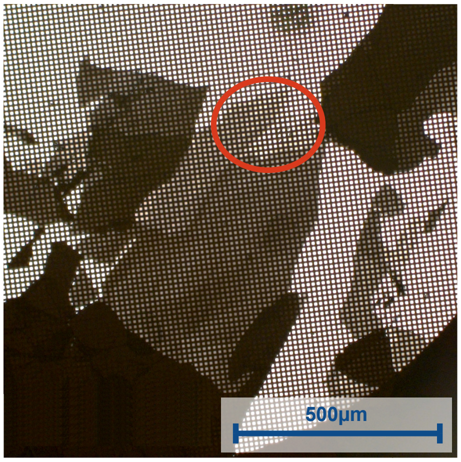

Figure 6.9: Transillumination microscopy image of graphite thin films produced by exfoliation. The heterogeneous layer thickness observed from different absorption is a result of the mechanical stress during exfoliation transfer of the thin film. However, a large area with sufficient thickness (red ellipse) for UED experiments is achieved.

6.2 Optical sample characterization

The determination of efficient excitation conditions for which a sample thin film provides sufficient reversibility is a major challenge of single-electron diffraction and a simple and fast characterization technique providing realistic excitation conditions is desired. The transmission microspectrometer described by Kirchner, Lahme, Riedle, and Baum [166] provides fast and easy optical characterization of small thin film sample. A white light source is collimated and focused onto the sample using two 90° off-axis parabolic mirrors. Another pair of these mirrors is used to collimate and couple the transmitted light into a fiber coupled, miniaturized spectrometer[10]. However, the incoherent white light source does not represent a realistic excitation and is therefore not suitable to characterize samples in terms of reversibility. To overcome this deficiency, the microspectrometer was upgraded together with Bachelor student Marina Hoheneder [164]. An additional optical excitation based on the excitation options in the UED setup was build providing laser pulses of roughly 50 fs at 800 nm, 400 nm and 266 nm wavelength. Using the UED pulse picker (see Section 5.1) variable repetition rates of up to 2.56 MHz are available. A sketch of the enhanced setup is shown in Fig. 6.10a. The focusing optics (simplified in the figure as a single lens FL) were designed to precisely adjust the beam diameter at the sample and achieve sufficient pumping fluence at the thin film. The incident angle of the laser is chosen such that transmitted intensity does not hit the off-axis parabolic mirror.

Besides conventional operation as microspectrometer, the additional optical excitation allows measurement of non-transient changes of the optical properties of the sample due to

---

[10] USB2000XR-1+ES, Ocean Optics Inc., United Stated of America, `http://www.oceanoptics.com` (Accessed: 3 September 2014).

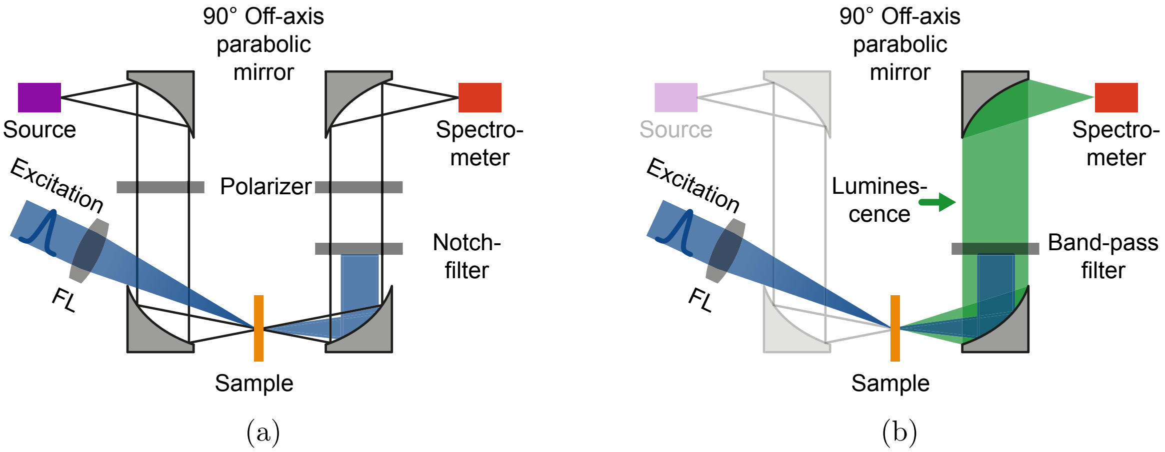

Figure 6.10: Upgrade to allow laser-excitation of the sample creates new operational modes for the original microspectrometer. (a) Non-reversible changes of optical properties of the sample can be observed by in-situ spectroscopy. (b) In micro-photoluminescence-spectrometer mode, photoluminescence from sample excitation is spectrally resolved.

excitation. For this, stray excitation light can be blocked by using a notch filter as shown in Fig. 6.10a. Additional thin film polarizers may be introduced to the incident and/or transmitted beam.

Another operational mode is shown in Fig. 6.10b which is applicable to samples that show any kind of photoluminescence from excitation. The primary broad-band source transmission microspectrometer (grayed out) is not used here. Exciting the sample, the specific photoluminescence is collected and measured by two parabolic mirrors and the spectrometer, respectively. Scattered excitation light can be blocked by either using a notch or a band-pass filter. This micro-photoluminescence-spectrometer (MPLS) mode has the advantage that no influence of the incoherent white light (such as UV bleaching) need to be taken into account.

In summary, the microspectrometer introduced by Kirchner, Lahme, Riedle, and Baum [166] was upgraded to allow spectral measurements during realistic sample excitation. This enables qualitative and quantitative measurement of sample damage from the excitation pulse before performing complex electron diffraction experiments. Furthermore, preliminary tests and systematic studies on damage thresholds minimize the overall amount of sample required and are indispensable for result-oriented time-resolved experiments. However, the presented setup does not yet feature vacuum capability. Hence, the significantly lower thermal insulation and potential (photo-chemical) oxidation of the sample must be taken into consideration when evaluating the results measured in air.

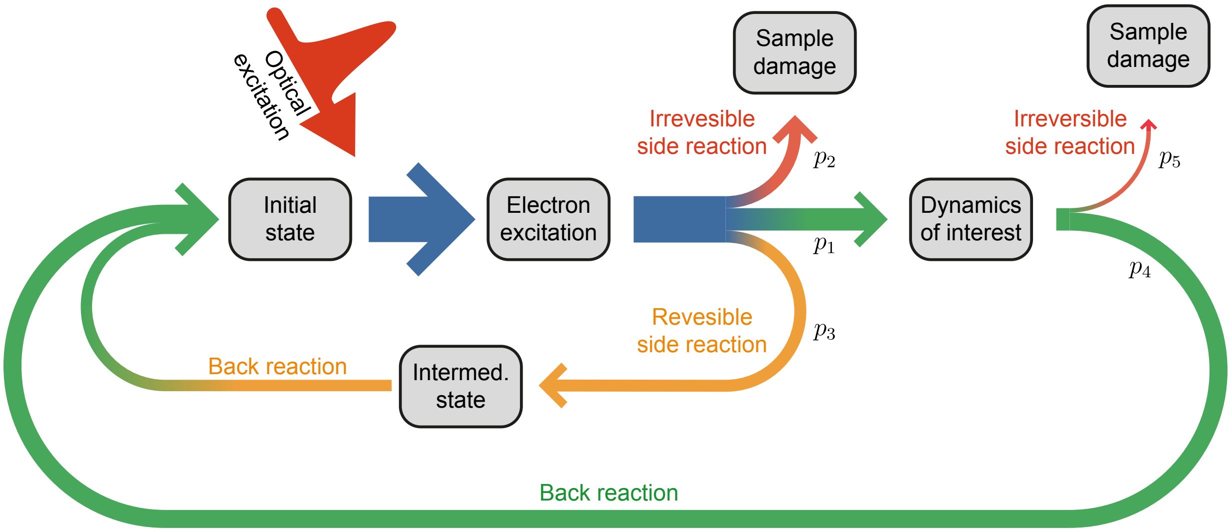

Figure 6.11: Illustration of a single excitation cycle including possible damage mechanism path ways. After laser excitation, the system of electrons relaxes via different channels. Only specific channels (p_1) trigger the dynamic of interest. Sample damage occurs from irreversible channels (p_2 and p_5) leads to a permanent change of the sample. These channels can either be present inherently or triggered by strong pumping (single pulse melting). Reversible side channels (p_3) are unproblematic as long as they do not dominate the dynamics of interest.

6.3 Damage from individual excitation

Mechanism

To perform a single-electron diffraction experiment in transmission without sample replacement, the prepared thin film sample has to withstand roughly 10^9 pump-probe cycles. The occurrence of even small amounts of sample damage from individual excitation cycles can therefore have disastrous consequences. A simplified illustration of a generalized excitation cycle is shown in Fig. 6.11. The pump laser pulse optically excites the sample from its initial state. Light couples strongly to the electronic system (electron excitation) but the dynamics of interest in UED often involve nuclear motion. Hence, the dynamics studied occur as a consequence of and subsequent to the electron excitation. However, only certain relaxation channels (green arrow) trigger the dynamics of interest, represented by probability p_1. Competing channels are irreversible and reversible side reactions. Whereas the former with probability p_2 cause sample damage (red arrow), the latter with probability p_3 lead back to the initial state (orange arrow). The relaxation of the studied dynamics in general can occur in different channels also. The back reaction with probability p_4 lead the system back to its initial state (green arrow) whereas an irreversible side reaction with probability p_5 causes sample damage (red arrow). From this picture, the reversibility of the process is defined as

$$\begin{aligned} \varrho &= p_1\, p_4 + p_3 \\ &= 1 - p_2 - p_5\,(1 - p_2 - p_3)\ . \end{aligned} \tag{6.1}$$

Full reversibility ($\varrho = 1$) is only achieved in the absence of any sample damage ($p_2 = p_5 = 0$). The amount of sample damage after n pump-probe cycles is $1 - \varrho^n$. To achieve less than 10 % sample damage after 10^9 cycles for example, p_2 must be less than 10^{-10} assuming $p_5 = 0$ for simplicity. This demonstrates the enormous sample reversibility required in single-electron diffraction.

An example of damage that can occur during a single excitation cycle is the irreversible breaking of bonds in molecular crystals. Photochemical modifications act as crystal defects that are randomly distributed over the sample. Defects lead to non-periodic changes in the local charge density of the crystal. Assuming the defects to be random vacancies, the structure factor (Eq. (A.4)) is effectively decreased by the relative defect density δ, and the intensity of a Bragg reflection is reduced by a factor of $(1 - \delta)^2$ [114]. However, this fast decrease of intensity with damage does not take into account spontaneous amorphization at a specific level of defect density. This might be energetically favorable and would lead to a complete loss in signal.

Damage from a single excitation cycle can also be a consequence of low excitation yields ($p_1 \ll 1$). To observe significant changes in the diffraction pattern at least 10 % of the sample must be excited to the dynamics of interest [167]. Hence, low pumping efficiencies have to be compensated with very intense pumping of the sample. However, the overall amount of deposited energy can lead to significant thermal stress and damage the sample by single pulse melting. To some extent, heat sinking and cooling of the sample can be applied to increase the damage threshold. In general, efficient excitation mechanisms should be preferred, e.g. direct terahertz excitation of phonon modes [168–170].

Example: MS1

The single-electron diffraction feasibility for the ESIPT compound MS1 was investigated. The unit cell and the crystal's basis is shown in Fig. 6.12a. The crystal structure is triclinic with lattice parameters of 9.0 Å, 10.9 Å and 11.2 Å for the lengths of the unit cell edges and 77.3°, 68.1° and 87.1° for the angles between them. The basis consists of two MS1 molecules that are flipped with respect to one another. An idealized illustration of the excitation mechanism is shown in Fig. 6.12b. MS1 crystallizes in the enol-closed configuration corresponding to the initial state in Fig. 6.11. A UV photon excites the molecule from S_0 to S_1 states. One relaxation pathway for the excited enol-closed form is to perform an ESIPT leading to the excited state of the cis-keto form. Fluorescence transfers the molecule back to the ground state of the cis-keto form with subsequent relaxation to the energetically favorable enol-closed form. The intensity of the photoluminescence is thus a measure of the relative number of molecules that have undergone an excitation cycle with ESIPT. A more complete description including competing side reactions is given by Karpicz et al. [65]. For example, the ESIPT excitation yield is decreased by direct $S_1 \rightarrow S_0$

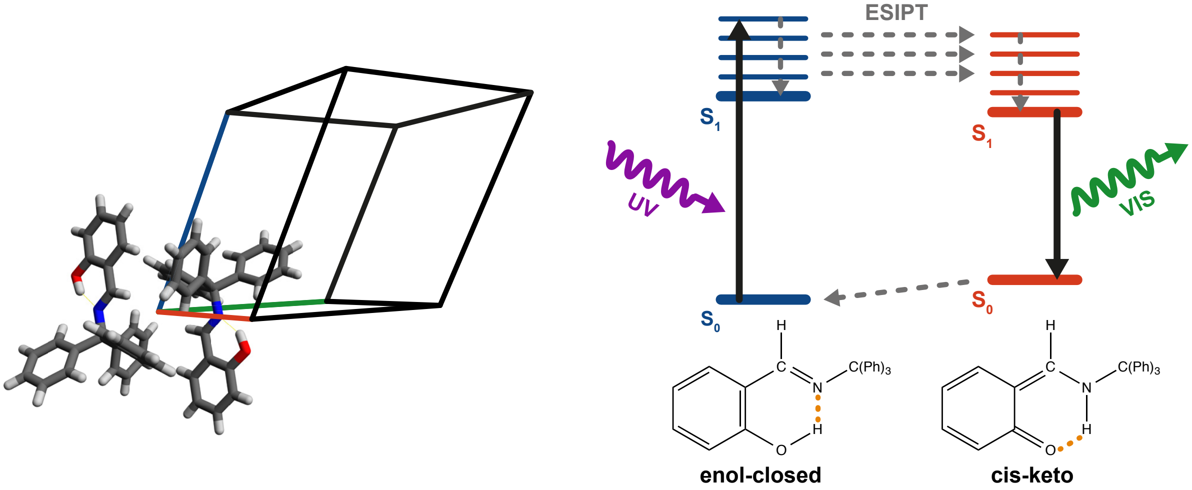

(a) (b)

Figure 6.12: (a) Illustration of the triclinic structure and the basis of crystalline MS1. The latter is formed by two molecules that are flipped with respect to one another. (b) Simplified excitation model of MS1 [65] and corresponding tautomers. The excited enol-closed tautomer relaxes via ESIPT to the excited state of the cis-keto tautomer. The subsequent, fluorescent relaxation to the ground state can be used as indicator of proton transfer. Relaxing back to the enol-closed tautomer completes one excitation cycle. Parasitic side channels are not shown for simplicity.

back reaction of the enol-closed form, corresponding to a process like p_3. Furthermore, different relaxation pathways from the S_1 state of the cis-keto form are assumed to build up a different species (e.g. trans-keto form or a photoproduct). If this species is stable, its build up ratio corresponds to a process like p_5 and causes irreversible sample damage.

To investigate the excitation mechanism of MS1, a micro-photoluminescence-spectroscopy study was performed together with Bachelor student Marina Hoheneder [164]. The ESIPT (see Fig. 6.12b) was excited with 400 nm laser pulses in a crystalline, 50 nm thin film of MS1 and the spectrum of the photoluminescence was recorded using the MPLS setup (see Fig. 6.10b). Scattered excitation light is blocked by an additional band-pass filter[11] whereas the expected photoluminescence around 525 nm [65] is transmitted. The results are shown in Fig. 6.13. A massive decay of integrated spectral intensity from 520 nm to 530 nm was observed within only 30 min of exposure as shown in Fig. 6.13a. The details of the unexpected interim recovery of the photoluminescence intensity within the first five minutes is not part of this work and are discussed in Ref. [164]. Figure 6.13b shows normalized spectra for different exposure times, indicating that no other photoluminescent species is involved in the damage mechanism of MS1.

---

[11] HQ465LP25, Chroma Technology Corporation, United Stated of America, `http://www.chroma.com` (Accessed: 3 September 2014).

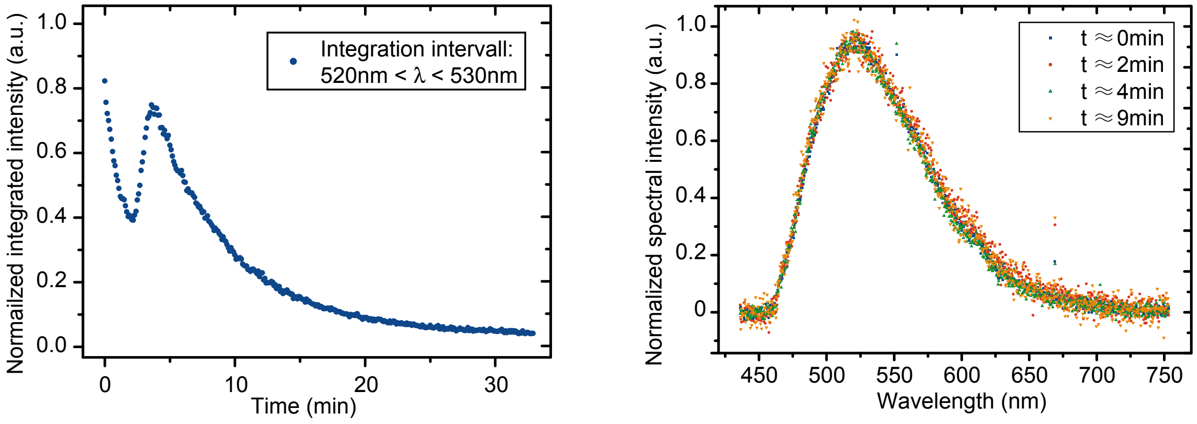

(a) (b)

Figure 6.13: Sample damage of MS1 from excitation observed by micro-photoluminescence-spectroscopy. (a) A massive loss in fluorescence intensity is observed within minutes. Furthermore, the data shows an unexpected interim recovery which is discussed in Ref. [164]. (b) Comparison of normalized spectra from different exposure times clearly indicate that no other photoluminescent species is involved in the damage mechanism. The spectra are in agreement with the literature [65].

To further investigate the excitation mechanism of MS1, photoluminescence and diffraction intensity were recorded after different laser exposure times in the range of 1 s to 400 s. A static diffraction pattern of a typical MS1 thin film produced by ultramicrotomy is shown in Fig. 6.14a. The many diffraction orders visible and the sharp Bragg reflections indicate both the high sample quality and high transverse coherence of the electron gun [2]. Note that the wire of beam block (see Section 5.1.5) was used to block the zeroth order of the beam as the paddle would have blocked the entire first diffraction order due to the large lattice constants of the crystal. The intensity of the 20 most intense Bragg reflections was evaluated for each exposure time, normalized and averaged. The photoluminescence was recorded with the close-up camera system consisting of a macro lens[12] and a high-resolution color C-mount camera[13] as described in [142]. A typical image is shown in the inset of Fig. 6.14 showing the photoluminescence of a bright triangular thin film such as the one shown in Fig. 6.7a. The orange ellipse corresponds roughly to the laser diameter. The summed intensity of this region was evaluated for for each exposure time. Both the photoluminescence and the diffraction intensity decrease rapidly with increased exposure time. As the photoluminescence I_{PL} reflects the number of molecules that successfully performed ESIPT it is assumed to be proportional to $1-\delta$. Assuming defects as random vacancies,

---

[12] Tamron SP AF 180 mm F/3.5 Di LD (IF) Macro 1:1, model: B01N from TAMRON Europe GmbH, Germany, `http://www.tamron.eu` (Accessed: 28 July 2014).

[13] Daheng DHHV3151UC-ML from China Daheng Group Inc., China, `http://www.daheng-image.com` (Accessed: 28 July 2014).

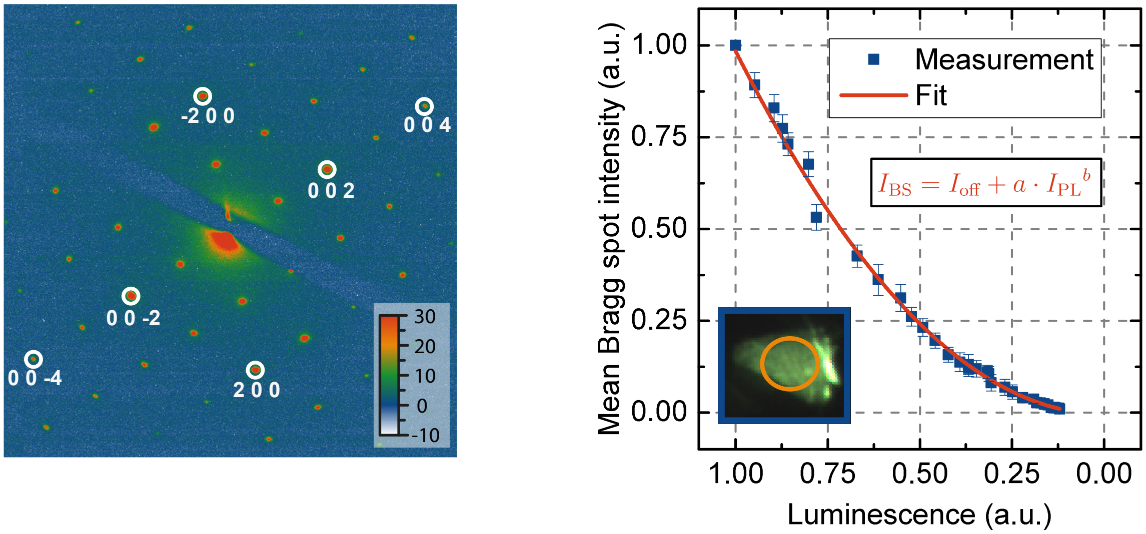

(a) (b)

Figure 6.14: (a) Typical diffraction pattern from MS1 single-crystals with identified crystal orientation. For reference, some of the reflections have been labeled with Miller indices (white circles). The many observable, sharp diffraction peaks indicate both, a degree of coherence of the electron source as well as high crystallinity. Due to the large lattice constants, only the wire of the electron beam block was used. (b) Measurement of the mean Bragg spot intensity versus photoluminescence from relaxation of the cis-keto tautomer after ESIPT. Equation (6.2) gives a good fit to the data indicating competing relaxation channels leading to crystal defects. The inset shows a photoluminescence image of the sample.

the diffraction intensity can be calculated to be proportional to $(1-\delta)^2$ [114]. Hence, if the decrease in diffraction intensity is caused by individual photo-induced damage to MS1 molecules, the mean intensity of the Bragg reflections should scale with $I_{\mathrm{PL}}{}^2$. To verify this hypothesis, the mean Bragg spot intensity is plotted against the photoluminescence and fit to an equation of the form

$$I_{\mathrm{BS}} = I_{\mathrm{off}} + a \cdot I_{\mathrm{PL}}{}^{b} \tag{6.2}$$

with I_{off} an arbitrary intensity offset. The result is shown in Fig. 6.14b with the fitted value $b = 2.01 \pm 0.04$. This is in nice agreement with the theory and supports the idea of competing relaxation channels in MS1 leading to irreversible damage or transition of the molecules. The average number of ESIPT cycles that an MS1 molecule can perform was estimated as 10^3 together with Hoheneder [164], corresponding to $p_5 \approx 10^{-3}$. Compared to the value of 10^{-10} required for a single-electron diffraction study this value of p_5 is orders of magnitude too large. In MS1, the irreversible side reactions are known to be related to rotational degrees of freedom [65]. Designing a MS1 derivate that features double bonds at the critical locations might significantly increase the reversibility without changing the ESIPT dynamics too much.

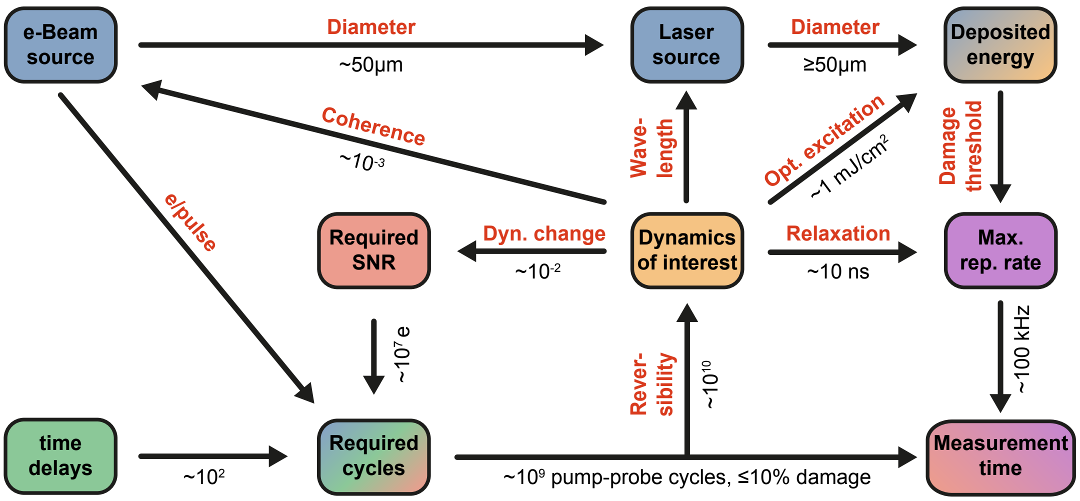

Figure 6.15: Illustration of the complex interrelations and dependencies working at high repetition rates of pump-probe cycles. Sample physics, number of time steps and electron source properties determine the required number of excitation cycles as well as the maximum feasible repetition rate, typically $> 10^9$ and $\sim 100\,\text{kHz}$, respectively. The ratio of both gives the required overall measurement time ($\sim 10\,\text{h}$). In return, this puts high demands on the stability of setup and electron source.

Summary

In summary, potential samples for single-electron diffraction studies must satisfy the condition that the probabilities $p_2, p_5 \leq 10^{-10}$ under the excitation conditions required for the dynamics of interest. Although in some cases p_2 might be reduced by tuning the wavelength of the pump laser, competing relaxation pathways usually cannot be avoided completely. Hence, sample damage from individual excitation cycles represents a major limitation of single-electron diffraction. However, especially in the case of organic molecules, molecular engineering might help to increase the reversibility without changing the dynamics of interest too much.

6.4 Damage from accumulated excitation and avoidance strategies

Mechanism

In contrast to the damage mechanisms from individual pump-probe cycles discussed in the previous section and due to the relatively high repetition rates required for UED, damage from accumulated excitation cannot be excluded. The complex interplay between different aspects of UED is illustrated in Fig. 6.15. To observe the dynamic of interest, a certain

SNR is required depending on the dynamical change induced from pumping. The resulting number of electrons required per time step was estimated to 10^7 in Section 2.1.2. Together with the number of time delays that need to be measured and the number of electrons per probe pulse, the number of required pump-probe cycles was estimated to $\sim 10^9$. This leads to high demands on the reversibility of the observed process as discussed in the previous section.

Working with $1\,e$/pulse, high repetition rates are beneficial as they reduce the integration time. Fundamentally the repetition rate is limited by the relaxation time of the observed dynamics, typically on the order of tens of nanoseconds. This corresponds to an upper limit of tens of megahertz at which 10^9 electrons could be acquired in less than 1 h. However, typical optical excitation fluences required are on the order of $1\,\mathrm{mJ/cm^2}$ and must be applied over the entire area probed by the electron beam. This leads to significant energy deposition in the sample. If an ensuing pump cycle is started before the sample has relaxed completely, excitation energy accumulates. Usually, deposited energy is ultimately transferred to thermal energy, increasing the sample temperature. The pump-probe repetition rate is thus limited by the thermal damage threshold of the sample.

The thermal damage threshold of a specific sample strongly depends on experimental setup and material properties. In general, heat diffusion in a sample is described by the heat equation

$$\rho\, c\, \frac{\partial}{\partial t} T(\vec{r}, t) - \kappa\, \nabla^2 T(\vec{r}, t) = Q(\vec{r}, t) \tag{6.3}$$

with T the temperature and the material constants ρ, c and κ as density, heat capacity and thermal conductivity, respectively. Note that in general, the material properties change with excitation but are assumed to be constant here for simplicity. Q represents an arbitrary source term of the system. The solution of this inhomogeneous parabolic partial differential equation (PPDE) depends on the particular boundary conditions set by the experimental setup.

The influence of the position of a heat sink $\vec{r}_{\mathrm{hs}}$ can be easily demonstrated assuming a one-dimensional, stationary and axially-symmetric problem. From Eq. (6.3) follows

$$-\kappa \left(\frac{\mathrm{d}^2}{\mathrm{d}r^2} + \frac{1}{r} \frac{\mathrm{d}}{\mathrm{d}r} \right) T(r) = Q(r) \tag{6.4}$$

$$T(r_{\mathrm{hs}}) = T_0\ , \quad \left. \frac{\mathrm{d}}{\mathrm{d}r} T(r) \right|_{r=0} = 0 \tag{6.5}$$

with Eq. (6.5) the Dirichlet boundary condition for the heat sink at temperature T_0 and the Neumann boundary condition excluding gradients at $r = 0$. Note that this model only takes into account a simple heat sink at the position r_{hs} of the sample. Continuous laser heating is modeled as

$$Q(r) = f_{\mathrm{rep}}\, E_{\mathrm{abs}}\, \frac{2}{\pi w_0^2 d_{\mathrm{s}}} \exp\left(-\frac{2r^2}{w_0^2} \right) \tag{6.6}$$

with f_{rep} the laser repetition rate, E_{abs} the absorbed laser energy per pulse, w_0 the laser beam diameter and d_{s} the thickness of the sample. From Eq. (6.6) and the axial symmetry

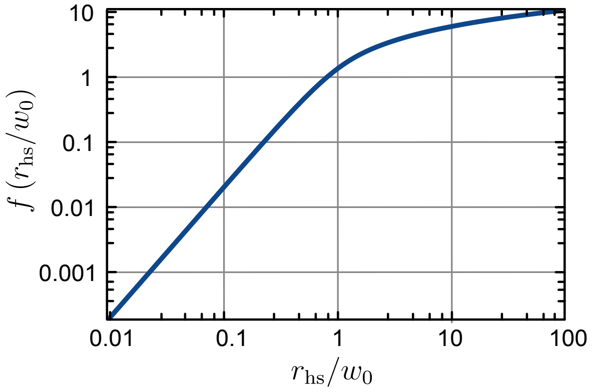

Figure 6.16: Derived slope f of Eq. (6.7) for different values of the ratio r_{hs}/w_0. Providing heat sinks with smaller radii significantly decreases the peak temperature and thereby increases the damage threshold.

of the problem follows that the peak temperature occurs at $r = 0$. The solution of Eq. (6.4) at $r = 0$ can be derived analytically as

$$T_{\mathrm{peak}} = T_0 + \frac{f_{\mathrm{rep}}\,E_{\mathrm{abs}}}{4\pi\,\kappa\,d_{\mathrm{s}}} \underbrace{\left[\mathfrak{E}_1\left(\frac{2{r_{\mathrm{hs}}}^2}{w_0^2}\right) + \ln\left(\frac{2{r_{\mathrm{hs}}}^2}{w_0^2}\right) + \gamma\right]}_{f(r_{\mathrm{hs}}/w_0)} \tag{6.7}$$

with $\mathfrak{E}_1$ the exponential integral[14] and γ the Euler–Mascheroni constant. Sample properties such as thickness and thermal conductivity as well as pumping energy are given by experimental constraints. The peak temperature scales linearly with the repetition rate but also depends strongly on the ratio r_{hs}/w_0. Figure 6.16 shows the calculated value of f for various ratios. For $r_{\mathrm{hs}} < w_0$, f decreases rapidly allowing higher values for the repetition rate. As the laser beam diameter is determined by the electron beam size, in general small values for r_{hs} are desired. Hence, UED samples are typically mounted on TEM grids consisting of fine meshes with up to 2000 bars per inch. However, to provide sufficient electron transmission, finer meshes must have smaller and thinner bars, limiting the thermal diffusivity (see Eq. (6.3)).

Example: Aluminum

The effect of accumulated temperature from laser excitation for a free-standing aluminum membrane was simulated using a finite element software package[15]. The model is shown in Fig. 6.17c and consists of a 50 nm aluminum thin film with a free-standing diameter of 200 µm mounted on copper. The bottom surface is held at a constant temperature and

---

[14] The exponential integral is defined as $\mathfrak{E}_1(z) = \int_1^\infty \frac{\exp(-tz)}{t}\,dt$.

[15] COMSOL Multiphysics®, COMSOL Inc., United States of America, `http://www.comsol.com` (Accessed: 10 July 2014).

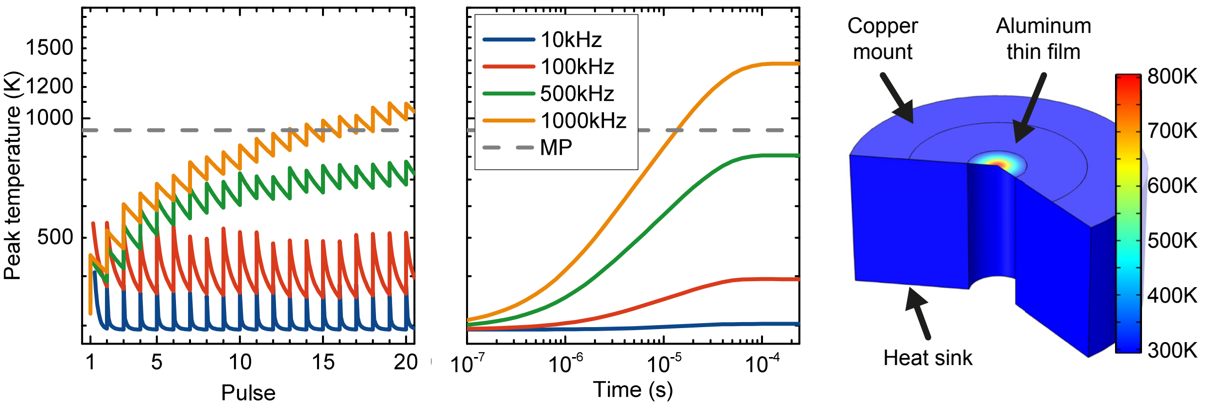

(a) (b) (c)

Figure 6.17: Simulation of thermal load from accumulated excitation in a 50 nm aluminum thin film. Time-dependent simulations of pulsed (a) and continuous (b) heat sources considering constant excitation fluence per cycle were performed on a model (c) of thin film and copper mount. For increasing repetition rates, the system does not have enough time to relax back to its initial temperature and a significant build up of average temperature occurs. In the case of 1 MHz the melting point (MP, grey, dashed line) is reached after only a few pulses, whereas for 500 kHz a saturation below the damage threshold is observed. Varying temperature step magnitudes in (a) are artificial, see text for detailed discussion.

act as a heat sink. Pulsed laser heating was simulated as a pulsed heat source with pulse lengths of 1 ns depositing 50 nJ at a fluence of roughly 50 mJ/cm^2. The simulation was performed for different repetition rates from 10 kHz to 1 MHz and the results for the first 20 laser pulses are shown in Fig. 6.17a. However, the results deviated significantly from the increase of average temperature which was simulated by simulating a continuous heat source with equivalent average power ($f_{\text{rep}} \cdot E_{\text{abs}}$). This is probably related to numerical issues as the simplified implementation of the periodic heat source turned out to be highly sensitive on the chosen time step intervals. Therefore, the results for the pulsed heat source were scaled to fit the reliable average increase in temperature derived for the continuous heat source. Variations in the magnitude of the temperature spikes are artificially caused by this re-scaling. Nevertheless, the basic mechanism of accumulated excitation can be seen. In the case of 10 kHz and 100 kHz, the temperature after relaxation is roughly equal to the initial temperature and no significant accumulation occurs. At 500 kHz however, a significant increase in relaxation temperature is observed, leading to an accumulation of heat at the sample. For an even larger repetition rate of 1 MHz, the accumulation is faster and the melting point (MP) of aluminum (gray, dashed line at 933 K) is reached after only 15 pulses. The results for the average temperature simulated by simulating a continuous heat source are shown in Fig. 6.17b. In the case of 500 kHz, a saturation closely to the damage threshold can be observed whereas working at 1 MHz leads to sample damage. The

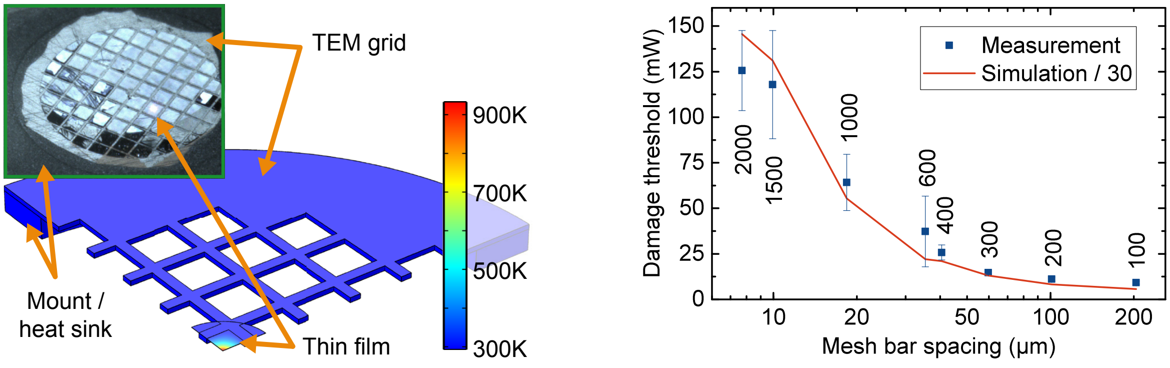

(a) (b)

Figure 6.18: The damage threshold for TEM grids with different mesh sizes were simulated and measured. (a) Model and mounted sample under laser excitation. (b) Measured damage thresholds and scales simulation results. The factor of 30 is likely related to a non-ideal thermal contact between the thin film and grid in the measurement and different material properties of the nanometer thin film. Reliable damage detection for larger meshes leads to small error bars.

time-dependent simulations with constant heat source were used to calibrate numerical inaccuracies of the simulations with pulsed heat sources.

The damage threshold of an 50 nm aluminum thin film mounted on a TEM grid was experimentally and theoretically studied for various mesh sizes from 100 mesh to 2000 mesh. Samples were produced together with D. Frischke[16] using electron beam evaporation and the sacrificial layer method. A mounted sample is shown in Fig. 6.18a. In the UED apparatus (see Chapter 5), the samples were exposed to a laser beam at 800 nm central wavelength with roughly 60 fs pulse duration, 30 µm beam width (FWHM) and 5 MHz repetition rate. The damage threshold was determined by gradually increasing the laser pulse energy and measuring the transmitted laser power as well as inspecting the film integrity visually. Measured damage thresholds are shown in Fig. 6.18b, clearly indicating the strong effect of the distance to the heat sink on the damage threshold of a free-standing thin film. Models for aluminum thin films on TEM grids[17] with heat sink were designed and simulations of continuous laser heating were performed based on the finite element method[18]. The 100 mesh model is shown in Fig. 6.18a. The results of the simulation predict much larger damage thresholds than observed in the measurements but dividing the results by a factor of 30, the simulation clearly reproduces the trend of the measurement (see Fig. 6.18b). This is still a reasonable agreement with the data as the simulation is performed using a highly idealized model. First, the material properties of the nanometer thin film are not necessarily identical with those of the bulk material used in the simulation. Second,

---

[16] D. Frischke, Technological Laboratory of LMU, Germany.

[17] Constructed with the help of Klaus Wirgler, Munich-Centre for Advanced Photonics, Germany.

[18] COMSOL Multiphysics®, COMSOL Inc., United States of America, `http://www.comsol.com` (Accessed: 10 July 2014).

Sample	$\boldsymbol{\lambda_{\mathrm{ex}}}$ (nm)	$\boldsymbol{F_{\mathrm{ex}}^{\mathrm{abs}}}$ (mJ/cm^2)	$\boldsymbol{f_{\mathrm{rep}}^{\mathrm{max}}}$ (kHz)
Titanium, 40 nm, polycrystalline	800	6.8	100
InP, 30 nm, single-crystalline	800	1.2	100
InP, 30 nm, single-crystalline	400	2.0	400
K-TCNQ, nm, single-crystalline	400	0.9	200

Table 6.1: Various samples, excitation wavelength λ_{ex}, absorbed pump fluence $F_{\mathrm{ex}}^{\mathrm{abs}}$ per cycle and maximum feasible repetition rate $f_{\mathrm{rep}}^{\mathrm{max}}$ for a time-resolved single-electron diffraction study determined from damage threshold measurements. The measurements were performed together with A. André [156].

the model assumes perfect thermal conduction between thin film and grid which could easily be orders of magnitude worse due to the mechanical transfer process. Furthermore, in case of the fourth data point at 18 µm, a hexagonal mesh was used whereas a square one was simulated which might explain the individual deviation of the corresponding data point.

Summary

In summary, sample damage from accumulated excitation can occur at high repetition rates and is therefore particularly important in the case of single-electron diffraction. At high repetition rates, the thermal damage threshold depends on the average power absorbed by the sample and the ratio of distance to heat sink and beam diameter. As the pump pulse fluence is set by the process to be observed, to mitigate heating, the electron source must provide small beam diameter at the sample to reduce the required pump-probe area. Furthermore, sufficient heat sinks need to be provided by careful sample preparation. Both are essential to be able to work at high repetition rates without damaging the sample.

In preparation of actual time-resolved experiments, the thermal damage threshold must be determined experimentally to optimize UED excitation conditions. The microspectrometer with laser excitation of the the sample discussed in Section 6.2 has proven to be a versatile and reliable tool for systematic damage threshold measurements. Careful feasibility studies for different samples were performed together with Master student Alexander André [156]. The results are summarized in Table 6.1 and demonstrate the general applicability of single-electron diffraction to many different sample systems with different physics.

The upper limit on allowable repetition rates is a major challenge for single-electron diffraction. Nevertheless, there are some strategies to circumvent this problem. The first is to work with continuously replaceable samples, although the effort for the enormous number of pump-probe cycles required for single-electron diffraction is unreasonably high. A second and very promising approach is to drive the atomic motions of interest more efficiently, for example using far-infrared pump pulses [168–170].

Chapter 7

Pump-probe single-electron diffraction on graphite

Graphite's carrier and phonon relaxation dynamics are interesting from a fundamental as well as technological perspective. The population of phonon states strongly influences the carrier mobility in graphene-based organic electronics [20, 50, 171, 172]. Hence, ultrafast dynamics of graphite thin films have been extensively studied theoretically [20] and using different experimental techniques [48, 50, 171–174]. Excited electrons couple strongly to a small number of optical phonons which are only weakly coupled to the rest of the lattice system. Although many aspects of this process are understood, there is still significant disagreement in the literature on the rates associated with different relaxation pathways. For this reason, a graphite thin film was used for a single-electron proof-of-principle experiment. The following sections are based on the results published in Ref. [1] and partially reproductions.

7.1 Laser excitation of graphite — An overview

If graphite is exposed to ultrashort laser pulses interband excitation of electrons leads to a non-equilibrium distribution of carriers [172]. Due to the high carrier-carrier scattering rates, the distribution relaxes with a time constant around 15 fs to a quasi-equilibrium state [172] which is established after 20 fs to 30 fs. In graphite, the excited electronic subsystem strongly couples to a small subset of optical phonons [175]. The population of these strongly-coupled optical phonon (SCOP) modes are the dominant relaxation channels for the hot electronic system [171, 172, 176]. Typical time constants for the SCOP build-up were found to be on the order of hundreds of femtoseconds [172, 176, 177]. The decay of these modes is typically on the order of picoseconds and much longer than the build-up rate and represent the bottleneck for carrier thermalization. The resulting formation of a quasi-equilibrium between electronic subsystem and SCOPs leads to an excess population of the SCOP modes, limiting the ballistic electron transport and thereby the performance of graphite, graphene or nanotube based electronics [18, 176]. Understanding the underlying

Experimental method	**SCOP decay time**	**References**
Ultrafast THz-spectroscopy	5.5 ps	[171]
Incoherent Raman scattering	$\approx$ 2 ps	[178, 179]
Time-resolved transmissivity and reflectivity measurements	2 ps–5 ps	[177]
UED in reflection mode	7 ps	[72, 180]
UED in transmission mode	8 ps–12 ps	[50]

Table 7.1: Reported decay constants for SCOP in graphite. The results vary from 2 ps to 12 ps. These large differences can not be explained properly yet and demonstrate the experimental challenge to measure the SCOP decay with sufficient accuracy.

ultrafast physics of the SCOP decay mechanisms in detail is therefore of high relevance for targeted optimization of these devices.

Theoretical as well as experimental studies have investigated the SCOP decay so far. Maultzsch et al. [175] identified the E_{2g} mode at the Γ point and the A_1' mode at the K point as the most dominant SCOPs. The phonon-phonon decay channels and the time constants for relaxation of these modes and were calculated by Bonini et al. [20], also finding a preferential population of the A_1' mode. Whereas the decay channels of E_{2g} mainly lead to population of phonons with high energies, the A_1' mode has efficient decay channels toward low-energy acoustic modes which results in a significant temperature dependence of the calculated life-times. A comprehensive experimental study by Scheuch et al. [171] based on ultrafast THz-spectroscopy confirmed the temperature dependence and the predicted decay time of 5.5 ps at 300 K, but could not observe the predicted contributions from the E_{2g} mode. However, other studies reported a wide range of SCOP decay times which are summarized in Table 7.1. The large range of values obtained indicates the experimental difficulty in measuring the SCOP decay times.

The spread of values given in Table 7.1 is much larger than the reported precision of the individual experiments. The spread must therefore be due to systematic errors caused by differences in either experimental techniques, sample preparation, or data evaluation procedures. The sample temperature, for example, was calculated [20] and measured [171, 178, 179] to have a significant effect on the SCOP decay times. Although the effect is small for measurements above room temperature, different pumping fluence and sample mounting (see Section 6.4) will affect the measured decay constants. Note that long relaxation times observed at room temperature or above [50, 72, 180] are not consistent with theory. Another source of variation might be the actual sample thickness. A study of sample thicknesses in the range from 1 to 100 basal planes [177] clearly indicated longer SCOP decay constants with increasing sample thickness. Hence, working with different samples

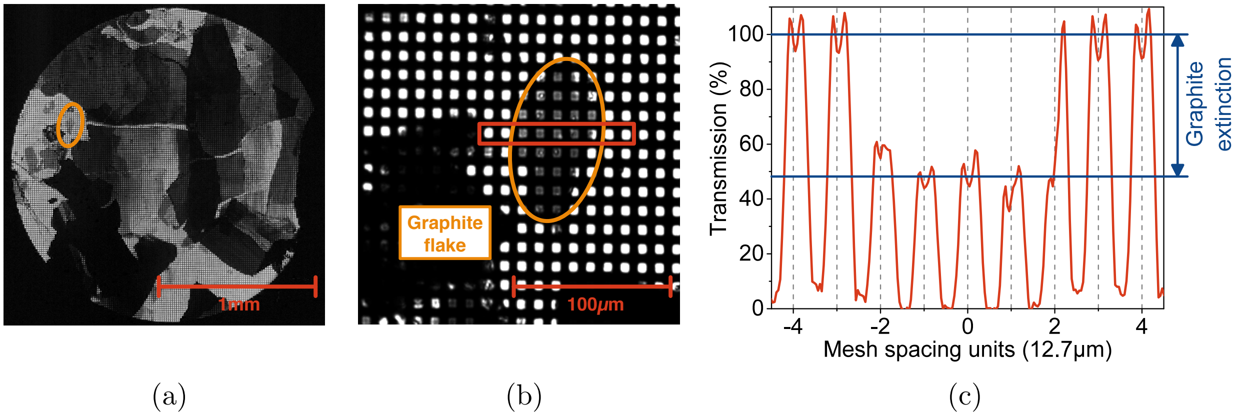

Figure 7.1: (a,b) Optical bright-field microscope images of free-standing graphite thin films produced by exfoliation and mounted on a TEM grid. Variations in transmission corresponds to different sample thicknesses. The orange ellipse marks a single flake. (c) Transmission profile along the red-marked area.

thicknesses (bulk material in the case of reflection measurements) can explain variations in measured decay constants as well.

In summary, all mentioned studies agree on the SCOP excitation mechanism, and the reported carrier relaxation times are in rough agreement. However, the reported values for the SCOP relaxation obtained in different studies vary by a factor of 5 and some of the observations do not agree with theoretical models. As the decay time of these phonon modes are assumed to represent a major limitation in graphene-based electronics, a better and detailed understanding of the underlying physics is desired. We therefore chose graphite as a sample to simultaneously illustrate the feasibility of ultrafast single-electron diffraction and improve knowledge of the relaxation dynamics in graphite.

7.2 Sample preparation and diffraction geometry

The extended exfoliation technique (see Section 6.1.2) was used to produce thin film samples of graphite from highly oriented pyrolytic graphite (HOPG). Copper TEM grids with 2000 mesh (spatial period of 12.7 µm) were used to provide mechanical support as well as a highly efficient heat sink. Figures 7.1a and 7.1b shows an optical bright-field microscope image of the TEM grid covered with graphite thin films and a closer view of a graphite flake. The overall transmission of the flake was measured along a horizontal slice (red rectangle in Fig. 7.1b) and was found to drop roughly to 50 % at holes covered with graphite as shown in Fig. 7.1c. This corresponds to a layer thickness of 25 nm on average [181]. Ultrafast dynamics in graphite are completely reversible and no damage is expected from an individual excitation cycle (see Section 6.3). The thermal damage threshold from accumulated excitation (see Section 6.4) corresponds to graphite's sublimation temperature of roughly 2000 K at 10^{-8} mbar [182] and was determined to be larger than 180 mW. Con-

Arc label	**A**	**B**	**C**	**D**
Corresponding lattice planes	$\{1\,0\,0\}$ $\{1\,\bar{1}\,0\}$	$\{1\,0\,\bar{1}\}$ $\{1\,\bar{1}\,1\}$	$\{1\,\bar{2}\,0\}$ $\{1\,1\,\bar{1}\}$ $\{1\,\bar{2}\,1\}$	$\{1\,0\,\bar{1}\}$ $\{1\,\bar{2}\,2\}$

Table 7.2: Corresponding lattice planes of observed arcs in Fig. 7.2d. The spacing for the listed planes is equal or beyond the resolution of the detection scheme.

sidering a pump fluence of $10\,\mathrm{mJ/cm^2}$ and a laser beam diameter of $50\,\mathrm{\mu m}$, the maximum repetition rate was estimated to roughly 0.9 MHz. Hence, the prepared graphite samples are feasible for single-electron diffraction.

HOPG is a modification of graphite (space group $P6_3$/mmc, $a = 2.464\,\text{Å}$, $c = 6.711\,\text{Å}$) consisting of grains that are well aligned with the c-axis, but azimuthally disordered [183], forming a fibrous polycrystal [184–186]. Although, the grain sizes can extend several millimeters, the mechanical stress from exfoliation causes significant reduction of the average grain size. At 0° sample tilt, the incident electron beam propagates perpendicularly to the cleavage plane and parallel to the c-axis (corresponding to the $[0\,0\,1]$ zone axis in a single crystal). In this geometry, only Bragg reflections with $(h\,k\,0)$ are provided, preventing observation of atomic motion along the c-axis [48, 50, 173]. To be sensitive to these dynamics as well, the sample was tilted by about 20° to achieve an electron beam incident along the $[0\,1\,1]$ zone axis. In case of the fibrous polycrystal, the tilt is expected to break the ring pattern into a series of arcs, where new arcs appear featuring reflections with c-axis contributions [184]. This concept is illustrated in Figs. 7.2a and 7.2b. Measured diffraction patterns for incident angles of 0° and 20° are shown in Figs. 7.2c and 7.2d. The inner four arcs are labeled A-D and correspond to the lattice planes listed in Table 7.2. In the case of the C-arc, lattice planes with slightly different spacings are listed together, because they cannot be clearly distinguished experimentally. Due to the superior beam quality in the single-electron regime, many individual Bragg reflections can be distinguished within each arc (Fig. 7.2e), indicating the limited number of grains probed by the electron beam. This transitional regime between single-crystal and powder diffraction provides a unique opportunity to study different grains simultaneously by spot-wise evaluation of pump-probe dynamics.

7.3 Temporal and spatial overlap

Spatial overlap of pump and probe beam at the sample as well as their temporal overlap are crucial for UED. In this work, both were determined simultaneously by observing deflection due to transient electric fields at the sample. This results in improved precision of the spatial and temporal overlap.

The pump laser was adjusted onto sample (graphite flake in Fig. 7.1b) using the close-up camera. Multi-photon photoemission leads to a local charge distribution in front of

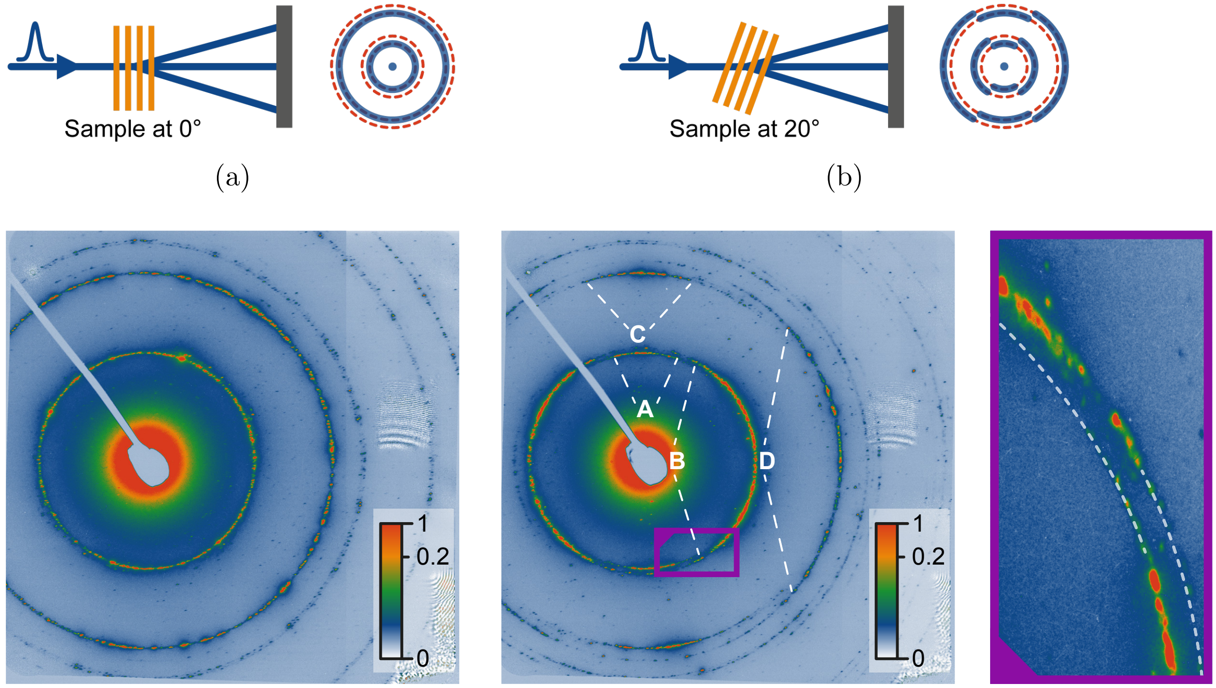

(a) (b)

(c) (d) (e)

Figure 7.2: Diffraction from tilted fibrous graphite thin films. (a) Diffraction geometry with a non-tilted sample (yellow) and c-axis parallel to the electron beam (blue). The expected ring pattern (blue) on the screen only consists of rings corresponding to $(h\,k\,0)$ while other rings are missing (red dotted lines). (b) Diffraction geometry with a sample tilted by 20° (yellow). The expected ring pattern breaks into arcs (blue) and additional features with c-axis contribution appear. (c,d) Experimental diffraction pattern taken at 0° and 20° with 360 fs few-electron pulses clearly showing the breaking into arcs. At 20°, several ring diameters are observable and the four smallest are labeled A-D, corresponding to the lattice planes listed in Table 7.2. (d) Details of rings A and B, revealing their different diameters and individual Bragg reflections.

the sample varying with time as it expands due to its inner space charge forces (see Section 3.3.3). The resulting transient electric fields deflect the electron beam, and the deflection can be observed on the camera. In contrast to previously reported approaches detecting shifts in position of the focused electron beam due to photoemission from a sharp structure of the sample mount [2], in this work an unfocused electron beam was used to record projected transmission images of the sample to directly measure time-zero (t_0) at the sample. For this, a series of transmission images for different time delays was recorded. The transient electric fields lead to a change of the intensity distribution of the unfocused electron beam while the overall beam intensity remains unchanged. Hence, the contrast of the signal is improved by subtracting a reference image recorded at $t \ll t_0$. Resulting

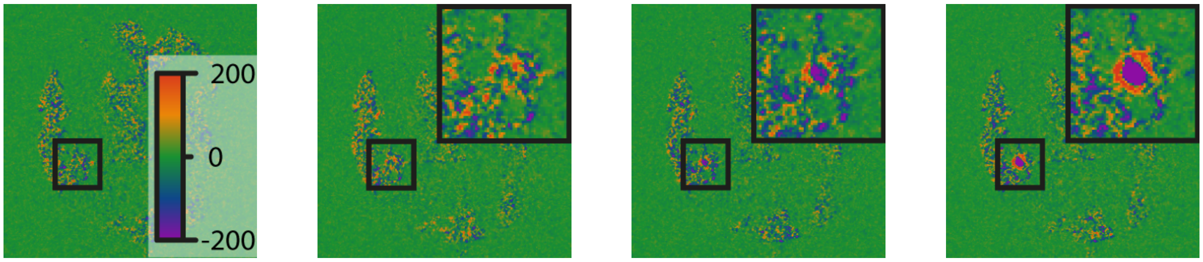

(a) −5 ps (b) 0 ps (c) 1 ps (d) 5 ps

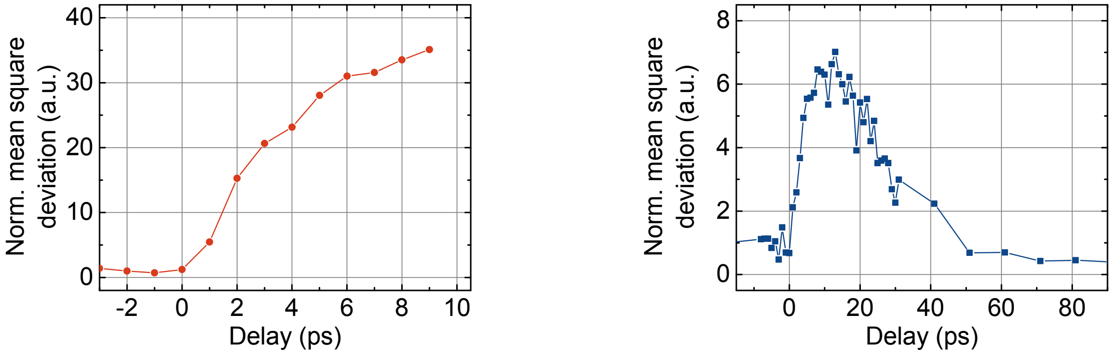

(e) (f)

Figure 7.3: (a-d) Differential projected transmission images at different time delays showing the expansion of the space charge cloud directly at the location of the sample. (e) Accurate determination of time-zero from transient electric fields dynamics with a precision of ±500 fs. (f) Long range transient electric fields dynamics that might influence Bragg spot positions.

differential images are shown in Figs. 7.3a to 7.3d for various time delays. The shape of the sample (see Fig. 7.1a) can be identified from the noise floor at permeable domains. The insets in Figs. 7.3b to 7.3d show magnifications of a region around the previously selected graphite flake (see Fig. 7.1b). The expansion of the space charge cloud for $t > 0\,\mathrm{ps}$ is clearly observed directly at the location of the graphite flake, confirming accurate spatial positioning of the pump beam. The normalized changes with time of the squared differential intensities integrated over a region around the graphite flake are shown in Fig. 7.3e. The achieved precision of ±500 fs is more than enough to set the range of delay times for an UED study but not sufficient to determine an absolute $t = 0$ for the dynamics of interest. In the measurement shown, the precision is mainly limited by the step size. Considering the significant change by a factor of 5 within the first step, sampling with smaller step sizes should improve the precision of this measurement.. However, due to the limited build-up time of transient electric fields, the accuracy of this method will probably not support the sub-100 fs regime.

It is worth noting that the laser fluence for pumping the sample in UED is comparable to that used here, and the time-dependent deflection of the electron beam must be taken into account when evaluating UED data. Qualitatively, the expected temporal characteristics of the transient electric fields can be observed from a long-range measurement shown in Fig. 7.3f. After a fast increase a slow decrease over tens of picosecond is observed. As the effect of transient electric fields is assumed to shift the incoming electron beam, an overall shift of the diffraction pattern is expected. In case of a single-crystalline sample, transient electric fields distortions can be deconvolved by observing the shifts in position of multiple Bragg reflections [180, 187]. In case of fibrous polycrystalline graphite however, in general this is not possible. Therefore, in the evaluation of transient structural dynamics of graphite only intensities were evaluated here.

7.4 Time-resolved electron diffraction

Time-resolved electron diffraction measurements were performed with electrons at 30 keV, corresponding to an acceleration field of approximately 4 kV/mm. The water-cooled magnetic lens was used to generate an electron beam focus between sample and detector. This special setting provided small beam diameter at the sample ($50\,\mu\mathrm{m}^2 \times 100\,\mu\mathrm{m}^2$) and at the detector ($150\,\mu\mathrm{m}^2 \times 300\,\mu\mathrm{m}^2$) at the same time. The sample was pumped by linearly polarized laser pulses of roughly 350 nJ energy focused to a diameter of 75 µm (FWHM), corresponding to an incident fluence of $\approx 8\,\mathrm{mJ/cm}^2$ under near-normal incidence, comparable to related studies [48, 72, 173]. Two different pump-probe data sets were recorded, one with $\sim 10\,e$/pulse on average at 128 kHz and one with $\sim 1\,e$/pulse on average at 256 kHz. The increase in temperature ΔT can be calculated from

$$E_\nu = \pi\, r_\nu^2\, d_\mathrm{s}\, \rho \int\limits_{T_\mathrm{min}}^{T_\mathrm{min}+\Delta T} C_p(T)\,\mathrm{d}T \tag{7.1}$$

with E_ν the laser pulse energy, r_ν the laser beam diameter, d_s the sample thickness, T_min the minimum temperature reached at relaxation and $C_p(T)$ the temperature-dependent specific heat capacity. The temperature dependence of d_s and ρ approximately compensate one another due to the fact that c-axis expansion dominates and are therefore neglected. Considering the measured damage threshold of approximately 180 mW and the corresponding sublimation temperature of roughly 2000 K (see Section 7.2), the relaxation temperature T_min was estimated from the applied average power ($P_\mathrm{avg} = f_\mathrm{rep} \cdot E_\nu$) to be less than 1000 K for the single-electron data set and less than 500 K for the ten-electron data set, respectively. By taking into account reflection and absorption for a 25 nm graphite layer [188], the laser beam dimensions, the density of $2260\,\mathrm{kg/m}^3$ [183] and the temperature-dependent specific heat capacity [189], the increase in temperature per pulse is estimated to be around 130 K for the measurement at $1\,e$/pulse and 240 K for the ten-electron data set. A slightly different sample alignment was used for the two data sets to access different grains. Both time-resolved measurements have been compiled from diffraction snapshots at 260 pump-probe delay times with an accumulation of $\sim 10^8$ incoming electrons per delay step corresponding to roughly 50 images acquired per step using correlated double

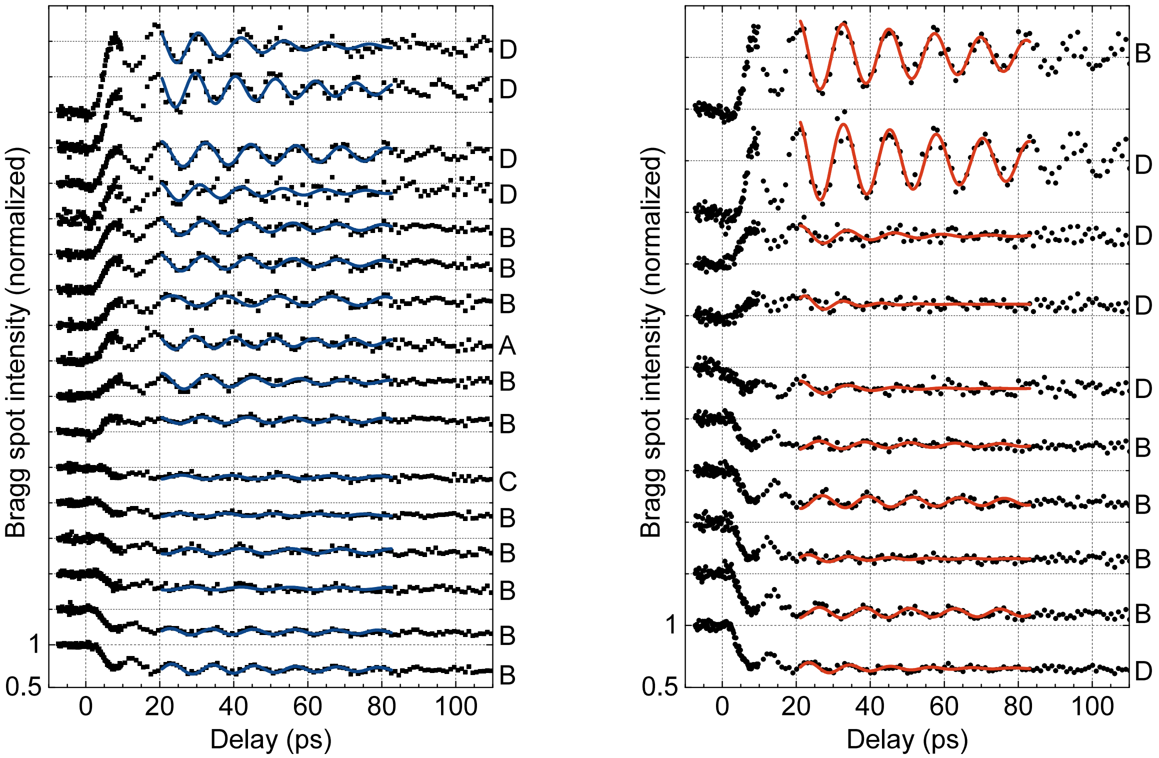

(a) (b)

Figure 7.4: Time-resolved intensity and fitting curves of investigated Bragg reflections for (a) ten-electron pulses and (b) single-electron pulses on different arcs (see Fig. 7.2d) as labeled on the right side on each plot. The individual traces were normalized and shifted for clarity; note the different intensity scales in (a) and (b). Error bars for each time step are not shown for convenience but were determined to be on the order of a few percent. Except one trace in (a), all traces correspond to lattice planes sensitive to c-axis dynamics.

sampling. During the entire measurement time of several tens of hours, no drifts of the photoemission yield were observed, demonstrating the enormous long term stability of the new source.

7.5 Results and discussion — The proof-of-principle

The time-dependent intensity of selected Bragg spots from the recorded data sets at 10 e/pulse and 1 e/pulse is shown in Figs. 7.4a and 7.4b, respectively. The measured data of both data sets clearly reveals a fast change with varying sign and amplitude (−40 % to 100 %) after laser excitation, followed by damped oscillations with slightly different periods. Additionally, most of the traces show previous minor dips or peaks in intensity previous to subsequent large scale dynamics. Oscillations were observed only in arcs B and

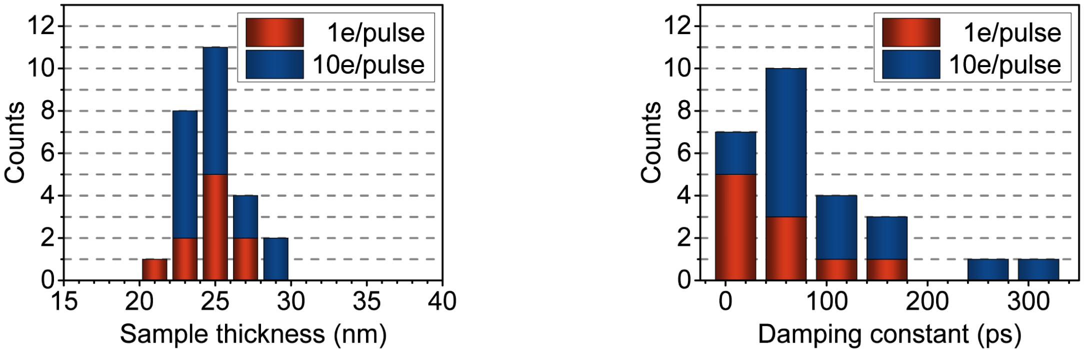

(a) (b)

Figure 7.5: Histograms of (a) the calculated sample thicknesses from Eq. (7.2) and (b) the damping constants. Both were obtained from the fits to the data shown in Fig. 7.4.

D, those sensitive to c-axis dynamics, with one exception from arc A. The non-normalized intensities before time-zero span the range of 1300 to 34 000 (a) and 1300 to 11 000 (b) total detected electrons. The quality of the data taken at 1 e/pulse on average is comparable to that taken at ten times higher electron fluence, demonstrating the feasibility of the genuine single-electron regime.

The following evaluations were performed for the combination of both data sets. The oscillations have been identified as coherent acoustic waves along the c-axis of the sample. Such breathing modes have been observed in various thin films of different materials [48, 49, 173, 190, 191]. Their periods and damping constants were evaluated by fitting a damped sine function for delays from 20 ps to 85 ps (solid lines in Fig. 7.4). A nice agreement with the data is achieved. The period τ_{osc} of the undamped breathing mode corresponds to the round trip time of the acoustic wave in the thin film [173] and is related to the the thickness of the sample

$$d_{\mathrm{s}} = \frac{v_{\mathrm{s}}\,\tau_{\mathrm{osc}}}{2} \tag{7.2}$$

with v_{s} the speed of sound along the c-axis. Taking into account $v_s = (4.14 \pm 0.04)\,\mathrm{km/s}$ [192], the sample thicknesses were calculated. Histograms of the determined values the sample thickness and damping constant are shown in Figs. 7.5a and 7.5b, respectively. The distribution of thicknesses is centered at 25.3 nm with a standard deviation of 2.3 nm. This is in good agreement with the optical measurement (see Section 7.2). The distribution of damping constants shows a large range from 25 ps to 300 ps, indicating different environmental conditions of each grain, such as inter-grain coupling and distance from the fixed supporting grid structure.

A proper explanation of the complex variations in Bragg spot intensity requires consideration of two different effects. First, the thermally induced change in orientation of the grain's zone axis with respect to its individual rocking curve can lead to increasing and decreasing diffraction intensities, which in general are non-linear. Second, further con-

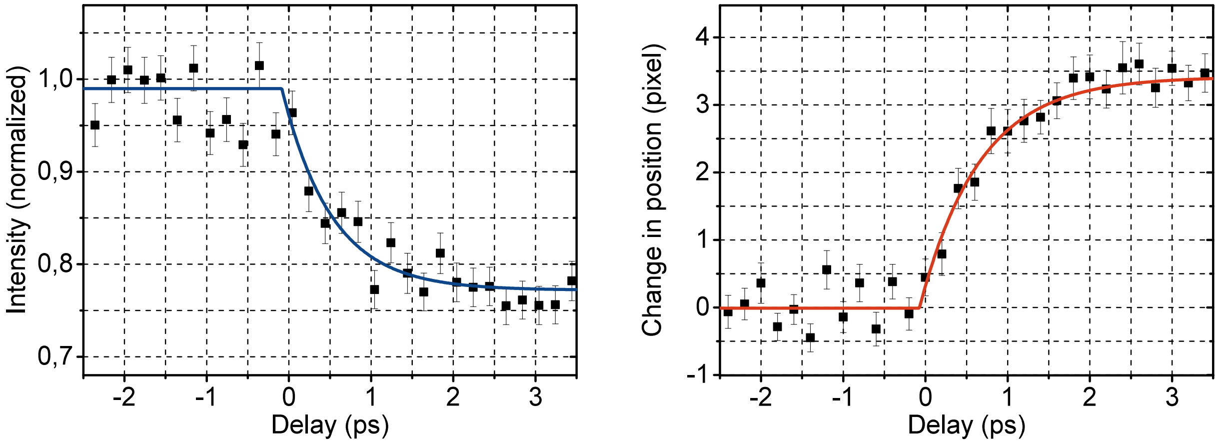

(a) (b)

Figure 7.6: Exponential fits (solid lines) to measured change in data (black squares) of different Bragg spots after laser excitation. Fitted time-constants of several hundred femtoseconds demonstrate femtosecond temporal resolution. (a) Change in intensity recorded with ten-electron pulses and (b) change in position recorded with single-electron pulses.

tributions from the Debye-Waller effect cannot be excluded. Hence, a proper extraction of graphite's phonon relaxation dynamics requires advanced data evaluation that will be discussed in Chapter 8.

However, the very fast initial changes in intensity and position observed in some of the Bragg spots can be used to characterize the temporal resolution of the setup. Figure 7.6 shows phenomenological exponential fits to intensity and position of two selected Bragg spots with time constants of (600 ± 170) fs and (700 ± 130) fs, respectively. In both cases, a significant change in signal within 500 fs clearly demonstrates femtosecond temporal resolution, which is in agreement with the pulse duration estimated in Section 5.2.5. The achieved temporal resolution of the single-electron setup is close to the state-of-the art of compressed multi-electron pulses (200 fs to 500 fs, FWHM) in UED [82, 101, 133, 134], although no pulse compression was applied here.

The signal-to-noise performance of the experiment can be determined from the variations of the measured Bragg spot intensities for negative pump-probe delays. Assuming that the diffraction pattern is identical for delays from -7 ps to -3 ps, the signal-to-noise ratio is calculated for each of the observed Bragg spots. Figure 7.7 shows the results, together with the shot noise limit as defined in Section 5.3.1. More intense Bragg spots are less noisy. The experiment approaches the shot noise limit within a factor of about two. The results shown in Fig. 7.7 in general follow the prediction of Eq. (5.10) but the signal-to-noise ratio found is significantly too low considering the averaging in this experiment. This indicates an additional noise source in the detection scheme of approximately 1.5 %, causing the signal-to-noise ratio to saturate around 60. Nevertheless, for many of the spots,

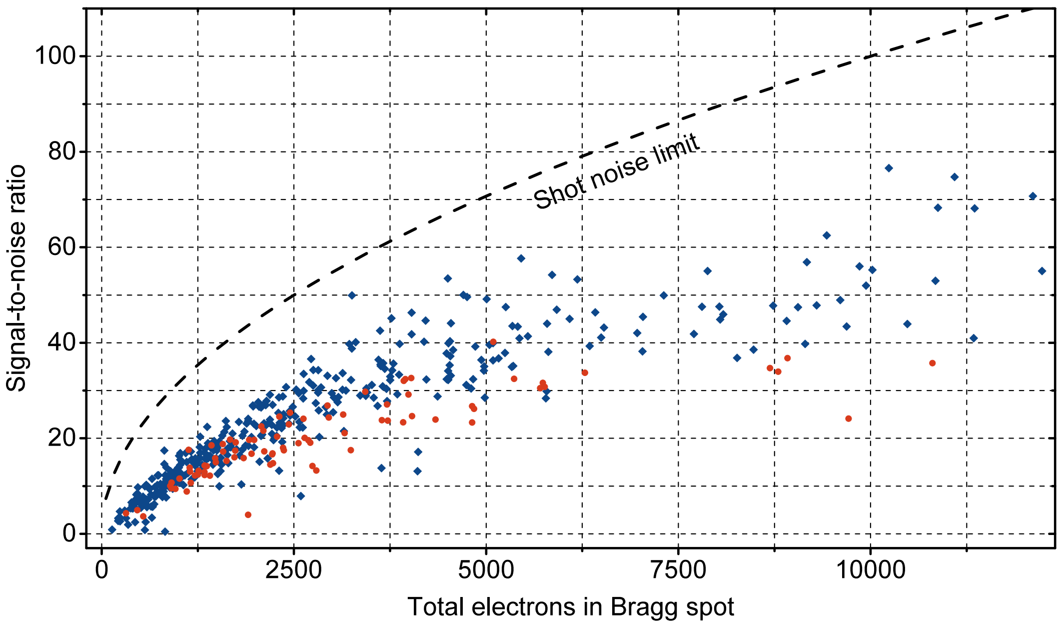

Figure 7.7: Experimental signal-to-noise ratio of pump-probe single-electron diffraction (red) and ten-electron diffraction (blue) in comparison to the shot noise limit (dashed).

the signal-to-noise ratio achieved allows observation of changes below 2 %, comparable to conventional multi-electron approaches [5, 51, 71].

In summary, measured time-resolved single-electron diffraction data is in agreement with intensity changes and coherent acoustic phonons obtained earlier on single-crystalline [48, 173] and polycrystalline [50] samples, but here for the regime of a fibrous polycrystal. The feasibility of time-resolved electron diffraction using single-electron pulses over their entire trajectory was demonstrated. The data quality was found to be comparable to multi-electron approaches. Although no pulse compression was applied, femtosecond temporal resolution was achieved with the single-electron setup which is promising for the 10 fs regime if combined with compression techniques [131, 141].

Chapter 8

Further investigation of structural dynamics in graphite

The analysis of UED data is often based on simplified physical models [50, 193] or pure phenomenological observations ("exponential plus sinusoidal") [48]. The fitted parameters are often directly related to physical quantities of the sample though. In some cases, this works out well, for example in the previously determined grain thicknesses from the observed breathing mode oscillations in Section 7.5. However, applying phenomenological data evaluation to more complex dynamics can be highly problematic as shown in the following.

8.1 Impact of different excitation steps on Bragg intensity

To extract information on the SCOP decay times from the measurement discussed in Chapter 7, a more comprehensive model considering the influence of the underlying physics on Bragg spot intensities is required. Hence, in the following, the impacts of different excitation steps on the intensity of a Bragg reflection are discussed.

Regarding the excitation mechanism discussed in Section 7.1, the build-up of the SCOPs represents the first process that potentially changes the Bragg spot intensities. However, the periods of the SCOP modes are around 20 fs [175] and below the temporal resolution of the single-electron setup without pulse compression. As the population of these modes occurs in a few hundreds of femtoseconds, contributions from the Debye-Waller effect (DWE, see Appendix A) should be observable. Due to their high frequencies and correspondingly small amplitudes, the DWE of the SCOPs can be estimated to be less than 1 % [50] which is smaller than the achieved signal-to-noise ratio of roughly 2 % (see Section 7.5). Therefore contributions from the SCOP build-up can be assumed to be negligible in this measurement.

Thermalization of the SCOPs occurs on the order of a few picoseconds and two different contributions to Bragg intensity have to be distinguished: Changes in the Debye-Waller

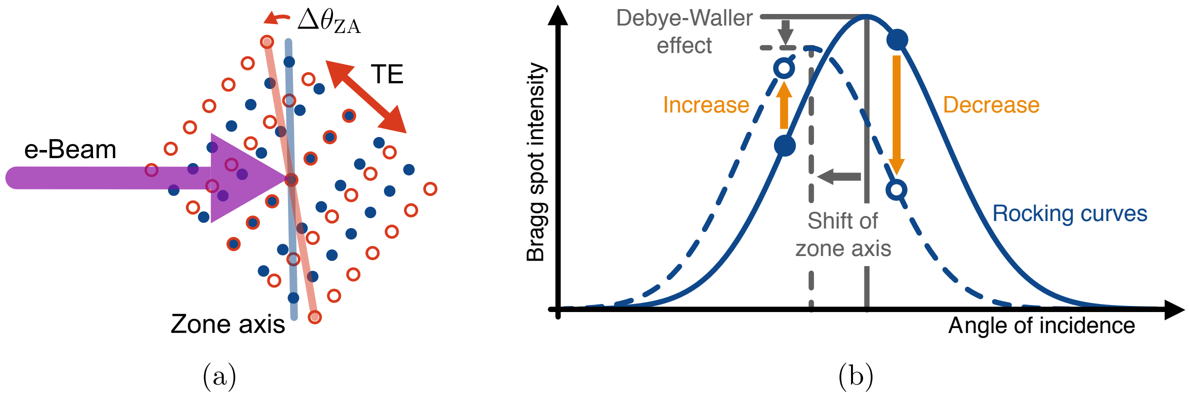

(a) (b)

Figure 8.1: (a) Tilt of the initial zone axis (blue line) from unidirectional thermal expansion (TE) of a crystal (blue dots). The zone axis (red line) of the heated crystal (red circles) is tilted by $\Delta\theta_{\mathrm{ZA}}$. (b) Mechanism of intensity change in Bragg spots due to thermal and expansion effects. Center and amplitude of the initial rocking curve (solid blue line) are shifted and reduced according to the shift in zone axis and the DWE, respectively. Depending on the initial incident angle, the initial Bragg spot intensity (blue solid circles) can increase or decrease (orange arrows).

factor and alignment changes of thermal expansion. The DWE can be estimated to several percent [50] for the laser fluences applied here The second contribution, a change in alignment, is caused by the highly anisotropic thermal expansion in graphite. Weak inter-plane bonding leads to a large expansion coefficient along the c-axis whereas expansion along the a-axis is negligible. As a result, zone axes that are not parallel to any of the principal axes change with temperature. Figure 8.1a illustrates the tilt of a zone axis $\Delta\theta_{\mathrm{ZA}}$ from thermal expansion (TE) for a two-dimensional lattice. As the electron beam pointing does not change during the experiment, a change of the zone axis corresponds to a shift of the crystal's rocking curve which describes the relation between incident beam angle and the resulting intensity of a Bragg reflection. Figure 8.1b illustrates the expected change of the initial rocking curve (solid blue line) at a constant incident angle for the electron beam. The rocking curve of the heated, expanded system (dashed blue line) is shifted in center position from the shift of the zone axis and lowered in amplitude from the Debye-Waller effect. The sign and amplitude of the observed change in diffraction signal (orange arrows) strongly depend on the initial incident angle with respect to the center of the rocking curve and the magnitude of the shift. Intensity changes caused by shifts of the rocking curve can compensate or even overcompensate decreases in diffraction intensity from the Debye-Waller effect.

In Section 7.5, the observed oscillations in intensity were identified as coherent breathing mode of the thin film. As this mode corresponds to a periodic expansion and compression of the sample, the impact on Bragg intensity is caused by a periodic shift of the zone axis. The phase of this oscillation and its build-up dynamics will depend on the SCOP relaxation rate.

To accurately extract the SCOP decay times from the measured data, the different contributions to the Bragg intensities must be considered for adequate data evaluation. An appropriate model is discussed in the next section.

8.2 Model for intensity modulations after laser excitation of graphite

According to the previously discussed two contributions, an approximation for the transient intensity is of a Bragg spot is

$$I_{hkl} = \underbrace{\frac{1}{1+w^2} \sin\left(\frac{\pi d_\mathrm{s}}{\xi}\sqrt{1+w^2}\right)^2}_{\substack{\text{Rocking}\\ \text{curve}}} \cdot \underbrace{\exp\left(-s\,\frac{k_\mathrm{B}T}{d_{hkl}^2}\right)}_{\substack{\text{Debye-Waller}\\ \text{effect}}} \tag{8.1}$$

with s an arbitrary scalar taking into account variations from the harmonic approximation of the Debye-Waller effect (see Eq. (A.9)) and d_{hkl} the lattice spacing as defined in Eq. (A.2). The rocking curve is defined by the the sample thickness d_s, the extinction length ξ and the deviation parameter w [114]. The extinction length can be interpreted as the effective sample thickness relevant for diffraction and is given by

$$\xi = \frac{\pi\, V_\mathrm{UC}}{|\mathcal{F}_{hkl}|}\,\sqrt{\frac{1}{\lambda^2} - \frac{1}{4\,d_{hkl}^2}} \tag{8.2}$$

with V_UC the volume of the unit cell, $\mathcal{F}_{hkl}$ the structure factor as defined in Eq. (A.4) and λ the de-Broglie wavelength of the electrons. The deviation parameter, w, describes the deviation from ideal diffraction alignment and is given as

$$w = \frac{\xi\,\Delta\theta}{d_{hkl}} \approx \frac{\xi}{d_{hkl}}\left(\delta\theta_0 + \Delta\theta_{[011]}\right) \tag{8.3}$$

with $\Delta\theta$ the deviation in angle of incidence. The latter is approximated as the sum of an initial offset $\delta\theta_0$ and the transient change of zone axis angle $\Delta\theta_{[011]}$ with respect to the electron beam. The consequences of this assumption will be discussed below. In the experiment, the sample tilt is defined as zero when the electron beam is incident along the [0 0 1] zone axis. The experiment was performed close to the [0 1 1] zone axis. Hence the angle between the electron beam and this zone axis is

$$\theta_{[011]} = \measuredangle\left(\begin{bmatrix}0 & 0 & 1\end{bmatrix} \cdot \begin{bmatrix}\vec{a}\\ \vec{b}\\ \vec{c}\end{bmatrix}, \begin{bmatrix}0 & 1 & 1\end{bmatrix} \cdot \begin{bmatrix}\vec{a}\\ \vec{b}\\ \vec{c}\end{bmatrix}\right) = \arccos\left[\left(1 + \frac{a^2}{c^2}\right)^{-\frac{1}{2}}\right] \tag{8.4}$$

with $\vec{a}, \vec{b}, \vec{c}$ the lattice vectors and a, b, c their lengths. At room temperature $\theta_{[011]}$ is calculated to 20.1° (see Section 7.2). The transient change of the zone axis $\Delta\theta_{[011]}$, however, depends on the actual dynamical expansion of the c-axis, $c(t)$.

Dynamics of the c-axis are caused by stress and thermal expansion. The major driving force for these dynamics is the build-up of lattice temperature $T(t)$ from SCOP thermalization. This build-up is described with a two-temperature model [194] for the temperature of the SCOPs and the temperature of the lattice, resulting in

$$T(t) = T_0 + H(t - t_0)\ \Delta T \left[1 - \exp\left(-\frac{t - t_0}{\tau_{\mathrm{SCOP}}}\right)\right] \ , \tag{8.5}$$

with T_0 the initial temperature (termed relaxation temperature in Section 6.4), ΔT the net temperature difference induced per pump pulse and τ_{SCOP} the thermalization constant reflecting the decay time of the SCOPs. The Heaviside step function $H(t - t_0)$ considers equilibrium of the system before t_0, i.e. before time-zero. From Eq. (8.5), $c(t)$ and thereby $I_{hkl}(t)$ can be calculated assuming some relation for the temperature dependence of c.

A simple approach for thermal expansion of the c-axis is given by

$$c(t) \approx c_0 \left[1 + \alpha_c \left(T(t) - T_0\right)\right] \tag{8.6}$$

with c_0 the lattice constant at T_0 and α_c the expansion coefficient along c. Linear expansion with temperature and a constant expansion coefficient over the temperature range from T_0 to $T_0 + \Delta T$ is assumed. Applying Eq. (8.6) to Eq. (8.1) and variables therein, the normalized transient intensity $I_{(01\bar{1})}(t) / I_{(01\bar{1})}(t < t_0)$ was calculated for different values of $\delta\theta_0$. Time-zero was assumed to be zero, the electron wavelength was determined by experimental conditions and values for sample thickness and induced temperature jump were taken from measurements and estimations discussed in Sections 7.2 and 7.4, respectively. The sample thickness is assumed to be constant for simplicity in this model. Lattice constants [183], expansion coefficient [189] and atomic form factors [195] at T_0 were taken from literature. For the remaining parameters, typical values were assumed, i.e. $\tau_{\mathrm{SCOP}} = 7\,\mathrm{ps}$ and $s = 3\,\mathrm{m}^2\,\mathrm{J}^{-1}$. The results are shown in Fig. 8.2a. The simple approach for lattice expansion approach from Eq. (8.6) of course does not reproduce the breathing mode. This could be fixed by introducing an additional, phenomenological sinusoidal term. However, taking a close look at the dynamics in the first few picoseconds the model fundamentally disagrees with most of the data shown in Fig. 7.4. Although the non-linearities of the rocking curve are taken into account, the (nearly) exponential change in intensity occurs too drastically and intensity dips seen in the data at early times are not reproduced.

The deficiencies of the simple lattice expansion in Eq. (8.6) are caused by the unphysical assumption of instantaneous response of the lattice, neglecting the lattice's inertia. Solving the equation of motion, a more accurate description of the dynamics of lattice expansion Δc is achieved. As expansion occurs mainly along the c-axis, a one-dimensional description is sufficient. Taking into account the restoring character of the inter-plane van-der-Waals interactions, the equation of motion is formulated in terms of a harmonic oscillator given as

$$\left(\frac{1}{\omega_0^2}\frac{\mathrm{d}^2}{\mathrm{d}t^2} + \frac{2\gamma}{\omega_0^2}\frac{\mathrm{d}}{\mathrm{d}t} + 1\right)\ \Delta c(t) = c_0\, \alpha_c \left(T(t) - T_0\right) \tag{8.7}$$

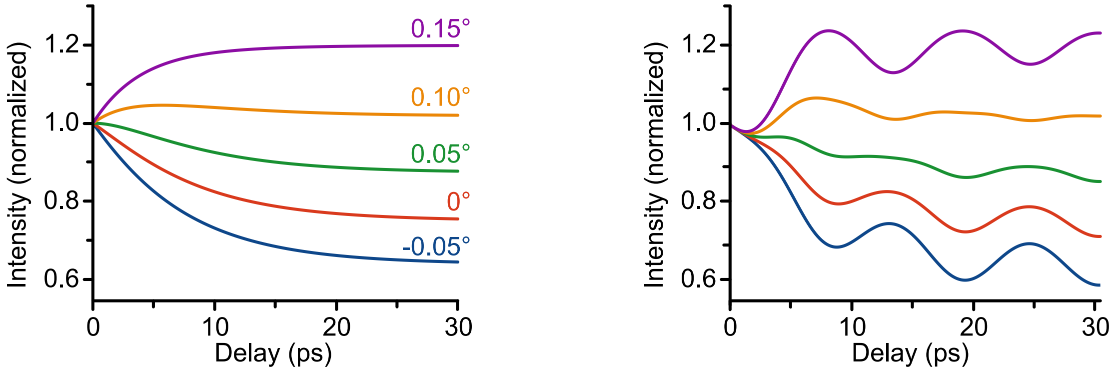

(a) (b)

Figure 8.2: Normalized calculated changes of Bragg spot intensity from DWE combined with different models of c-axis dynamics. (a) Considering instantaneous thermal expansion, initial features observed in the data cannot be reproduced. (b) Deriving the change in lattice constant from an equation of motion including inertia of the film, agreement with all observed features is achieved.

with $\omega_0 = 2\pi/\tau_{\text{osc}}$ the undamped frequency of the system and $\gamma = 1/\tau_{\text{damp}}$ the damping constant. The oscillation period τ_{osc} is related to the sample thickness via Eq. (7.2). Using Eq. (8.5), the solution for $\Delta c(t)$ was derived analytically with the help of Green's function [196] and applied to Eq. (8.1) and dependent variables. The normalized transient intensity $I_{(01\bar{1})}(t)\,/I_{(01\bar{1})}(t < t_0)$ was calculated for different values of $\delta\theta_0$ with the same parameters used before. Additionally the literature value of $v_s = (4.14 \pm 0.04)\,\text{km/s}$ for the speed of sound [192] was taken into account and a damping time of $\tau_{\text{damp}} = 80\,\text{ps}$ was assumed. The results are shown in Fig. 8.2b. Comparing this result with the measured data shown in Fig. 7.4, one can clearly see that the model much better reproduces initial changes in diffraction intensity. Especially some distinct experimental features like initial dips are reproduced well as an interplay of contrary contributions from the DWE and an accelerated shift of the rocking curve. Furthermore, the coherent breathing mode occurs naturally as a result of an underdamped oscillation of the lattice planes rather than a phenomenological sinusoid. Using literature values for the speed of sound in graphite, the sample thickness is inherently determined by the model.

In summary, the simple model of thermal expansion (Eq. (8.6)) was shown to not reproduce the data, whereas the one considering the inertia of the lattice does well. Nevertheless, the resulting model for $I_{hkl}(t)$ still contains some strong assumptions and simplifications. Some of these could be refined to further increase accuracy. For example, the rocking curve introduced in Eq. (8.1) does not take into account any absorption which should slightly change its slope [114]. Also, all rocking curves for different Bragg reflections are intrinsically interrelated by the angles of different lattice planes with respect to each other and the initial misalignment of the grain is defined by only two angles. Here, the deviation angle $\delta\theta_0$ is assumed as a free parameter for each fit and the change in angle considered in Eq. (8.3) is approximated to be equal for all reflections and is estimated from changes of the [0 1 1] zone axis. This leads to non-zero intensity changes for reflections that do not have any c-axis contributions. On the one hand, the affected Bragg reflections are usually not of interest anyway. On the other hand, in addition to the breathing mode, nonuniform surface deformation leading to shear components have been reported for free-standing thin films of silicon [49]. Locally, these deformations correspond to tilts of the corresponding zone axis. Hence, considering individual $\delta\theta_0$ for all reflections the model might be expanded to a zeroth-order approximation describing the mentioned deformations. Another simplification is the two-temperature model used (see Eq. (8.5)), which only takes into account the thermalization between two baths, i.e. the SCOPs and the lattice. Possible intermediate steps [20] that might have significant influence on the diffraction intensity [50] are not considered. Further simplifications are introduced by modeling the breathing mode as a direct result of inertia and force constants of bulk graphite. Although this seems reasonable because the van-der-Waals interaction forces between the basal planes act as restoring force, possible contributions from other mechanisms of exciting the breathing mode are neglected in this approach. Interpreting the breathing mode as a coherent acoustic phonon, direct pumping from SCOP decay at the K-point (see Section 7.1) is also conceivable. Furthermore the temperature dependence of some of the parameters, namely the speed of sound, the expansion coefficient and the atomic form factors are neglected.

Nevertheless, the nice agreement of features observed in the data with theoretical calculations is promising for a reliable evaluation of the measured data and indicate the importance of an accurate, physically motivated model.

8.3 Results and discussion — The SCOP decay time

As discussed in the previous section, the developed model contains a large number of parameters and material constants. Although most of them can be taken from literature, the remaining parameters – namely t_0, ΔT, τ_{SCOP}, d_{s}, τ_{damp}, (hkl), s and $\delta\theta_0$ – provide too many degrees of freedom to reliably determine all of them from a single Bragg reflection shown in Fig. 7.4. Considering a full set of Bragg reflections from a single grain however, the degrees of freedom are significantly reduced by the exact determination of the Miller indices and the additional constraints arising from shared parameters.

The fibrous polycrystalline sample used in this work provides access to multiple grains at the same time, but the assignment of the many observed Bragg spots to specific grains is challenging. In a first step, Bragg reflections with equal oscillation periods were selected from the $10\,e$/pulse data set. Subsequently crystallographic calculations[1] were used to identify those Bragg reflections belonging to the same grain and determine the Miller indices according to the [0 1 1] zone axis. This procedure allowed identification of six Bragg reflections covering three different lattice spacings and with high probability stemming from a single grain. These are shown in Fig. 8.3a. The fact that the Bragg spot intensities are

---

[1] CrystalMaker™ and SingleCrystal™, CrystalMaker Software Ltd., United Kingdom, `http://www.crystalmaker.com` (Accessed: 16 July 2014).

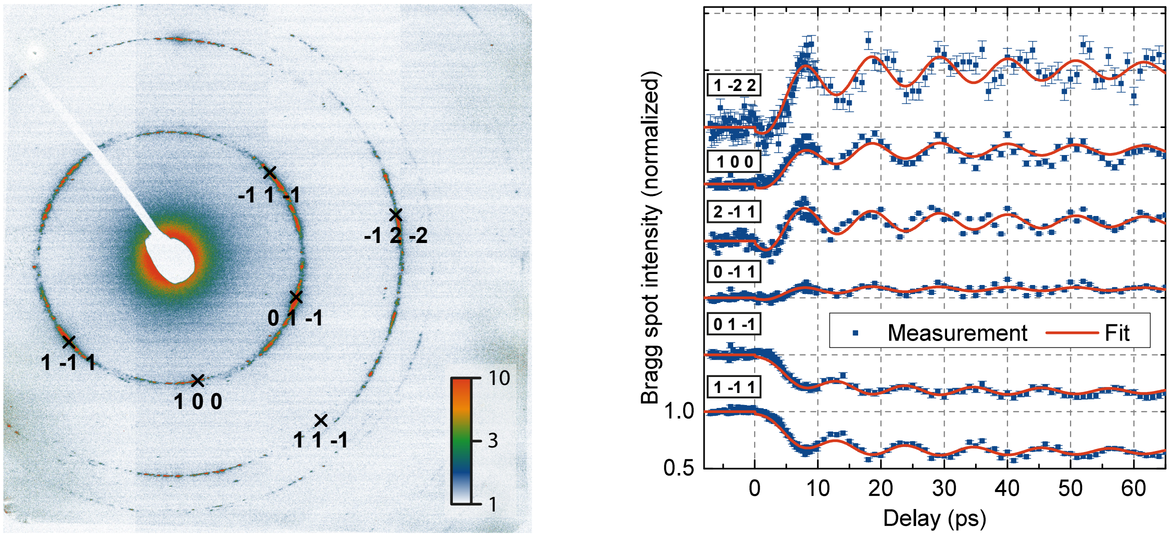

(a) (b)

Figure 8.3: (a) Identification of Bragg reflections belonging to a single grain in the fibrous graphite flake. The non-symmetric arrangements indicated a misalignment of the zone axis with respect to the incoming electron beam. (b) Time-resolved intensity (blue squares) and global fit (red lines) of identified Bragg reflections. The individual traces have been normalized and shifted for clarity. The main features of the data are reproduced by the fit. See text or further discussion.

not symmetric around the transmitted beam indicate an initial misalignment of the grain's zone axis with respect to the electron beam.

The normalized transient intensity $I_{hkl}(t)\,/I_{hkl}(t<t_0)$ was calculated analytically using Eq. (8.1) and the solution of Eq. (8.7). The electron wavelength was determined from the acceleration voltage of 30 kV. Equation (7.2) was used to determine the sample thickness d_s from the oscillation period τ_osc. The initial temperature T_0 was assumed to be constant ($\leq 500\,\text{K}$ as estimated in Section 7.2). Values for lattice constants [183], the expansion coefficients [189], atomic form factors [195] and the speed of sound [192] were taken from literature and assumed to be constant. The resulting expression for the normalized transient intensity was fitted to the measured data taking into account the determined Miller indices. Fitting parameters for time-zero, the temperature difference ΔT, the Debye-Waller scaling factor s the damping of the oscillation γ, the sample thickness d_s and the thermalization constant τ_SCOP were shared for all Bragg reflections. The initial angular deviation of the incident electron beam $\delta\theta_0$ remained the only individual parameter for each of the six Bragg reflections.

The data and fit result are shown in Fig. 8.3b. A nice agreement between the data and the advanced model is observed. Especially the initial dynamics of the Bragg spots, such as dips ($2\,\bar{1}\,1$, $1\,\bar{2}\,2$) and apparent delays ($1\,\bar{1}\,1$, $0\,1\,\bar{1}$) are well reproduced. The fitted time-zero of (100 ± 100) fs is in nice agreement with value determined from transient electric fields at the sample (see Section 7.3). The temperature increase per pulse was fitted to $(68 \pm 5)\,\mathrm{K}$, which is lower than the value estimated in Section 7.4. However, considering inhomogeneous pumping of the sample from the Gaussian laser beam, the fitted value is still reasonable. The fitted sample thickness of $(22.4 \pm 0.3)\,\mathrm{nm}$ is in good agreement with the optical transmission measurements. The damping constant of $(61 \pm 10)\,\mathrm{ps}$ is reasonable, given the speed of sound and distance to support structures. The Debye-Waller scaling factor was fitted to be $(2.8 \pm 0.3)\,\mathrm{m^2\,J^{-1}}$, corresponding to a few percent of change in intensity, similar to the results of Schäfer et al. [50]. Values obtained for $\delta\theta_0$ are in the range from $-0.24°$ to $0.31°$, which is reasonable concerning the expectable accuracy from the manual alignment of the sample. Considering the widths of corresponding rocking curves, non of the values for $\delta\theta_0$ exceeds the first minimum of the corresponding rocking curve, indicating meaningful results. The thermalization constant, identified in this model with the SCOP decay, was fitted to $(6.6 \pm 0.4)\,\mathrm{ps}$. This is the key result of this study.

A similar UED study on polycrystalline graphite thin films, reported a bi-exponential change of the transient intensity [50] with a fast component of 700 fs. In this work, the existence of a fast component could not be confirmed although the temporal resolution was demonstrated to be sufficient (see Section 7.5). This discrepancy might be caused by two fundamental differences in this study. First, in contrast to the simple bi-exponential model, contributions from both the DWE and rocking curve shifts were taken into account here. Neglect of the latter might lead to misinterpretation of the observed data, especially because the rocking curve acts as a non-linear transfer function between *c*-axis expansion and Bragg spot intensity. Only taking into account the exponential relation of the DWE, for example, an additional decrease in intensity from the rocking curve shift would be interpreted as a faster time constant. The observed fast changes in the data discussed in Section 7.5 that were used to characterize the temporal resolution of the setup are quoted as example. Second, the usage of a fibrous crystal granted access to single grains whereas in the case of a polycrystalline sample, averaging over multiple grains with different contributions from rocking curve shifts cannot be avoided and might lead to artifacts.

The fact that the 1 0 0 reflection in Fig. 8.3b shows similar behavior to the other reflections even though it is insensitive to *c*-axis dynamics indicates a more complex process. Hence, as discussed in the previous section, the assumption of individual rocking curves is reasonable.

In summary, the SCOP decay time was determined from a new comprehensive model, taking into account DWE and shifts of the rocking curve. The decay time found supports the results of Scheuch et al. [171], Newson et al. [177], but does not agree with theory [20]. Intermediate steps in the SCOP relaxation [50] could not be observed. To unambiguously clarify the underlying physics, the structural dynamics of the SCOPs should be measured directly. Such a study would require with single-crystalline thin films and sub-20 fs temporal resolution to resolve coherent oscillation of the SCOPs [19]. Thanks to the demonstration of ultrafast single-electron diffraction achieved in this work and the recent demonstration of $\sim 10\,\mathrm{fs}$ compressed single-electron pulses, the requisite time-resolution will soon be available. The model developed here can help to accurately distinguish different contributions to intensity changes in such experiments.

Chapter 9

Outlook

This work demonstrates the feasibility of time-resolved electron diffraction using single-electron pulses free of any space charge. Key innovations were a novel electron gun concept for high coherence and long-term stability, as discussed in Chapter 5, and novel strategies and methods for avoiding sample damage at the high repetition rates required for single-electron diffraction, as reported in Chapter 6. The proof-of-principle study performed on graphite discussed in Chapter 7 demonstrates the practical applicability of the single-electron approach as a versatile and working methodology for studying reversible transient atomic motions in the solid phase. A realistic model of changes in graphite's Bragg intensities from *c*-axis dynamics was developed in Chapter 8 and will help to deconvolve

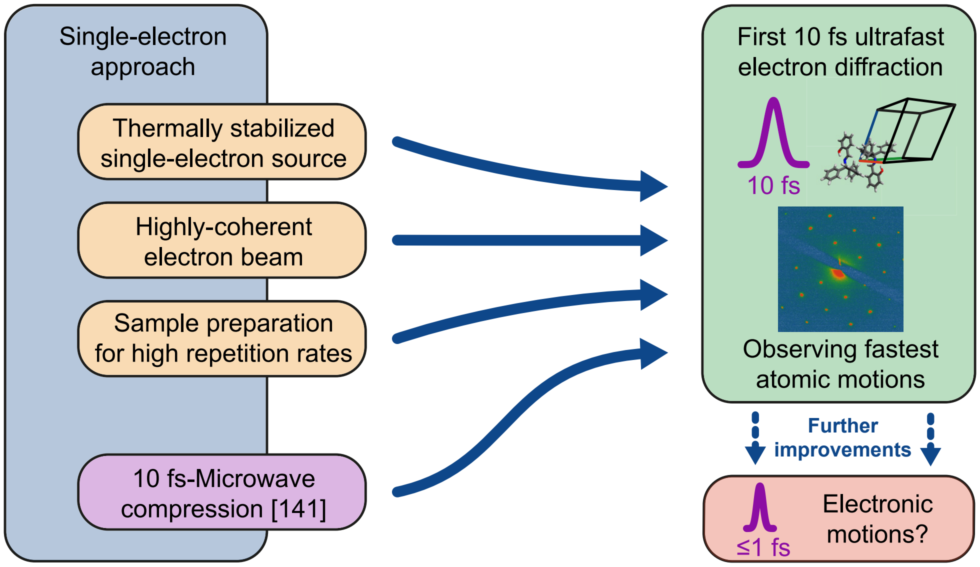

Figure 9.1: Providing high coherence, sufficient long-term stability and high compressibility at the same time, the single-electron regime is promising to achieve temporal resolutions in the 10 fs-regime and thereby gaining access to the fastest atomic motions in condensed matter.

different contributions to Bragg spot intensities in future UED studies of materials with non-isotropic dynamics.

Recent experiments on microwave compression of single-electron pulses have reported achievable temporal resolutions of roughly 20 fs (rms) [141], an order of magnitude smaller than temporal resolutions reported for compressed, space-charge-dominated electron pulses [101, 120]. The proof-of-principle work on graphite reported here shows that time-resolved experiments with such pulses are realistic with well-prepared sample systems. The single-electron regime now provides both highly-coherent electron beams and high compressibility. This opens up the possibility of studying many fundamental processes that have so far eluded structural dynamics, for example anharmonic coupling of coherent optical phonons in graphite [19, 20], molecular dimerization in spin-Peierls materials [7], phase transitions in correlated electron materials with the perovskite structure [57], and collapse of charge-density waves [16, 17]. The high stability of the photoelectron gun demonstrated in this work is an essential prerequisite for all such future UED studies with single-electron pulses. Advanced synchronization [197] of the microwave pulse compression method [141] and avoidance of temporal beam distortions [117, 123] will potentially push the temporal resolution of UED into the 1 fs-regime or even below, thereby directly accessing not only the fastest motion of atoms but also ultimately the dynamics of charge densities in condensed matter.

Appendix A

Diffraction physics

Basics

The basic physics of diffraction is the interference of particles that are elastically scattered from a periodic potential distribution [114]. In the case of electron diffraction, the relevant scattering potential is given by the periodic electron density of a crystalline sample. In general, crystals consist of a ensemble of atoms that is periodically repeated in all three spatial dimensions to build a lattice. The repeating unit is called the unit cell and the location and identities within this unit cell are called the basis. Hence, the basis causes a set of equal sub-lattices with the same lattice constants but shifted in position.

Constructive interference of electrons occurs only if the Laue equations are fulfilled, i.e. the difference between the wavevector of the incoming electron $\vec{k}$ and the wavevector of the scattered electron $\vec{k}'$ is equal to a reciprocal lattice vector $\vec{G}$.

$$\vec{k} - \vec{k}' = \vec{G} \tag{A.1}$$

A more visual explanation comes from considering reflection at sets of lattice planes with the inter-plane distance

$$d_{hkl} = \frac{2\pi}{|\vec{G}|} \tag{A.2}$$

with h, k and l the Miller indices for the lattice plane normal to $|\vec{G}|$. Defining the angle between incoming and diffracted electron as 2θ, Eq. (A.1) results in Bragg's law

$$\lambda = 2\, d_{hkl} \sin\theta \tag{A.3}$$

with λ the wavelength of the incoming electron.

From Eq. (A.1) it follows that the occurrence of a constructive interference for a specific $\vec{k}'$ only depends on the lattice because $\vec{G}$ is defined by the lattice of the crystal structure. Alternatively, in terms of Eq. (A.3), the angle at which constructive interference can occur is defined by the lattice plane spacing of the crystal structure. Because of this and the fact that all sub-lattices caused by the crystal's basis have the same lattice constants, the position of a Bragg reflection on the detector contain structural information about the crystal's lattice.

However, the relative positions of the sub-lattices lead to phase shifts, which are considered in the structure factor

$$\mathcal{F}_{hkl} = \iiint\limits_{V_{UC}} \rho\left(\vec{r}\right) \, \exp\left[i \, \vec{G} \, \vec{r}\right] = \sum_i f_i \, \exp\left[i \, \vec{G} \, \vec{r}_i\right] \tag{A.4}$$

with $\rho\left(\vec{r}\right)$ the potential and V_{UC} the volume of the unit cell [114].

The right hand side of Eq. (A.4) introduces the atomic scattering factor, reducing the integral to a sum over the different basis atoms with relative coordinates $\vec{r}_i$ [114]. Interference of the contributions from different sub-lattices leads to different intensities of the Bragg reflections:

$$I_{hkl} \propto \left|\mathcal{F}_{hkl}\right|^2 . \tag{A.5}$$

Thus, whereas the position of the Bragg reflections on the detector contain structural information about the crystal's lattice, their intensity contains information about the crystal's basis. Depending on the dynamics of interest, desired information can be concealed in the position of the Bragg spots, their intensity or both.

The Debye-Waller effect

Temperature is described as average kinetic energy of an ensemble of particle. In a crystal this movement is described with quantized vibrational modes of the crystal's lattice called phonons. The time-dependent atomic displacement $\vec{u}(t)$ from its equilibrium position $\vec{r}_i$ is described as the sum of displacements of different phonons [114]. According to Eqs. (A.4) and (A.5), a time-dependent atomic displacement leads to a time-dependent intensity $I_{hkl}(t)$. However, in general phonons are incoherent and averaging over multiple gives the temporal mean intensity

$$\begin{aligned} I_{hkl} = \left\langle I_{hkl}(t)\right\rangle &\overset{(A.5)}{\propto} \left\langle \left| \sum_i f_i \, \exp\left[i \, \vec{G} \, \left(\vec{r}_i + \vec{u}_i(t)\right)\right] \right|^2 \right\rangle \\ &\approx I^0_{hkl} \cdot \left| 1 + \underbrace{\left\langle i \, \vec{G} \, \vec{u}_i(t) \right\rangle}_{=0} + \left\langle \frac{1}{2} \left(\vec{G} \, \vec{u}_i(t)\right)^2 \right\rangle \right|^2 \end{aligned} \tag{A.6}$$

The temporal average of the displacement vanishes. Approximating the leftover summands can be interpreted as a first order series expansion of an exponential function and assuming isotropy of the phonon potential [58] gives

$$I_{hkl} \approx I^0_{hkl} \cdot \exp\left[-\frac{1}{3}|\vec{G}|^2 \, \left\langle |u|^2 \right\rangle\right] \; . \tag{A.7}$$

The exponential function in Eq. (A.7) is called Debye-Waller factor. The average elongation of the atoms $\langle |u|^2 \rangle$ strongly depends on the temperature of the sample. For an increase of temperature the diffraction intensity of a Bragg reflection is expected to decrease exponentially.

Assuming the mean energy $\langle U \rangle$ of a classical harmonic oscillator and its thermodynamic potential energy $\frac{3}{2} k_{\mathrm{B}} T$, $\langle |u|^2 \rangle$ can be derived from

$$\frac{1}{2}\, m\, \omega^2 \left\langle |u|^2 \right\rangle = \langle U \rangle \overset{!}{=} \frac{3}{2} k_{\mathrm{B}} T \tag{A.8}$$

with m and ω the mass and frequency of the oscillator, k_{B} the Boltzmann constant and T the temperature. Solving Eq. (A.8) for $\langle |u|^2 \rangle$ and using Eq. (A.2), the mean intensity follows as

$$I_{hkl} \approx I^0_{hkl} \cdot \exp\left[-\frac{4\, \pi^2\, k_{\mathrm{B}} T}{m\, \omega^2\, d^2_{hkl}} \right] \tag{A.9}$$

with I^0_{hkl} the Bragg intensity at $T = 0\,\mathrm{K}$. An increase in temperature leads to an exponential decrease in mean intensity of the Bragg reflections. Note that the DWE is more intense for larger diffraction orders, i.e. smaller values for d_{hkl}.

Appendix B

Data Archiving

The experimental raw data, evaluation files, and original figures can be found on the Data Archive Server of the Laboratory for Attosecond Physics at the Max Planck Institute of Quantum Optics: `/afs/rzg/mpq/lap/publication_archive`

In the `/figures` directory relative to the root folder of the data archive, the data of all figures in this thesis is organized in subfolders. The subfolders are named `fig_X.X` with `X.X` the same figure number as in the thesis. Each subfolder contains the data of that figure and a text file named `fig_X.X.txt` (where `X.X` is the figure number) which gives detailed information about the organization of the data and the processing performed to obtain the final figure. Final figures named corresponding to the figure numbers in the thesis can be found in the subfolders.

Bibliography

[1] S. Lahme, C. Kealhofer, F. Krausz, and P. Baum. “Femtosecond single-electron diffraction”. *Structural Dynamics* 1.3 (2014).

[2] F. O. Kirchner, S. Lahme, F. Krausz, and P. Baum. “Coherence of femtosecond single electrons exceeds biomolecular dimensions”. *New Journal of Physics* 15 (2013).

[3] F. O. Kirchner, A. Gliserin, F. Krausz, and P. Baum. “Laser streaking of free electrons at 25 keV”. *Nature Photonics* 8.1 (2014), pp. 52–57.

[4] C. Effertz et al. “Design of Novel Dielectric Surface Modifications for Perylene Thin-Film Transistors”. *Advanced Functional Materials* 22.2 (2012), pp. 415–420.

[5] P. Baum, D. S. Yang, and A. H. Zewail. “4D visualization of transitional structures in phase transformations by electron diffraction”. *Science* 318.5851 (2007), pp. 788–792.

[6] S. Wall et al. “Ultrafast changes in lattice symmetry probed by coherent phonons”. *Nature Communications* 3 (2012).

[7] H. Okamoto et al. “Ultrafast Photoinduced Melting of a Spin-Peierls Phase in an Organic Charge-Transfer Compound, K-Tetracyanoquinodimethane”. *Physical Review Letters* 96.3 (2006), p. 037405.

[8] K. Ikegami et al. “Ultrafast photoinduced melting of spin-Peierls phase in the organic charge-transfer compounds alkali-tetracyanoquinodimethane”. *Physical Review B* 76.8 (2007).

[9] J. Bardeen, L. N. Cooper, and J. R. Schrieffer. “Theory of Superconductivity”. *Physical Review* 108.5 (1957), pp. 1175–1204.

[10] M. K. Wu et al. “Superconductivity at 93 K in a new mixed-phase Y-Ba-Cu-O compound system at ambient pressure”. *Physical Review Letters* 58.9 (1987), pp. 908–910.

[11] A. Schilling, M. Cantoni, J. D. Guo, and H. R. Ott. “Superconductivity above 130 K in the Hg-Ba-Ca-Cu-O system”. *Nature* 363.6424 (1993), pp. 56–58.

[12] G. Grüner. “The dynamics of charge-density waves”. *Reviews of Modern Physics* 60.4 (1988), pp. 1129–1181.

[13] F. Schmitt et al. “Ultrafast electron dynamics in the charge density wave material TbTe3”. *New Journal of Physics* 13 (2011).

[14] N. Erasmus et al. “Ultrafast Dynamics of Charge Density Waves in 4H(b)-TaSe2 Probed by Femtosecond Electron Diffraction”. *Physical Review Letters* 109.16 (2012).

[15] S. Wall et al. “Atomistic Picture of Charge Density Wave Formation at Surfaces”. *Physical Review Letters* 109.18 (2012).

[16] T. Rohwer et al. “Collapse of long-range charge order tracked by time-resolved photoemission at high momenta”. *Nature* 471.7339 (2011), pp. 490–+.

[17] S. Hellmann et al. “Ultrafast Melting of a Charge-Density Wave in the Mott Insulator 1T-TaS2”. *Physical Review Letters* 105.18 (2010).

[18] M. Lazzeri and F. Mauri. “Coupled dynamics of electrons and phonons in metallic nanotubes: Current saturation from hot-phonon generation”. *Physical Review B* 73.16 (2006).

[19] Kunie Ishioka et al. “Ultrafast electron-phonon decoupling in graphite”. *Physical Review B* 77.12 (2008).

[20] Nicola Bonini, Michele Lazzeri, Nicola Marzari, and Francesco Mauri. “Phonon Anharmonicities in Graphite and Graphene”. *Physical Review Letters* 99.17 (2007).

[21] M. P. Oneil et al. “Picosecond Optical Switching Based on Biphotonic Excitation of an Electron Donor-Acceptor-Donor Molecule”. *Science* 257.5066 (1992), pp. 63–65.

[22] M. Andersson et al. “Bio-inspired optically controlled ultrafast molecular AND gate”. *Angewandte Chemie-International Edition* 42.27 (2003), pp. 3139–3143.

[23] Dominik B. Bucher, Bert M. Pilles, Thomas Carell, and Wolfgang Zinth. “Charge separation and charge delocalization identified in long-living states of photoexcited DNA”. *Proceedings of the National Academy of Sciences* 111.12 (2014), pp. 4369–4374.

[24] B. M. Pilles et al. “Mechanism of the Decay of Thymine Triplets in DNA Single Strands”. *Journal of Physical Chemistry Letters* 5.9 (2014), pp. 1616–1622.

[25] Sebastian Henke, Andreas Schneemann, and Roland A. Fischer. “Massive Anisotropic Thermal Expansion and Thermo-Responsive Breathing in Metal–Organic Frameworks Modulated by Linker Functionalization”. *Advanced Functional Materials* 23.48 (2013), pp. 5990–5996.

[26] Sebastian Henke, Wei Li, and Anthony K. Cheetham. “Guest-dependent mechanical anisotropy in pillared-layered soft porous crystals - a nanoindentation study”. *Chemical Science* 5.6 (2014), pp. 2392–2397.

[27] R.J. Dwayne Miller. “Mapping Atomic Motions with Ultrabright Electrons: The Chemists’ Gedanken Experiment Enters the Lab Frame”. *Annual Review of Physical Chemistry* 65.1 (2014), pp. 583–604.

[28] D. J. Flannigan and A. H. Zewail. “4D Electron Microscopy: Principles and Applications”. *Accounts of Chemical Research* 45.10 (2012), pp. 1828–1839.

[29] A. H. Zewail. “4D ultrafast electron diffraction, crystallography, and microscopy”. *Annual Review of Physical Chemistry* 57 (2006), pp. 65–103.

[30] Antoine Rousse, Christian Rischel, and Jean-Claude Gauthier. “Femtosecond x-ray crystallography”. *Reviews of Modern Physics* 73.1 (2001), pp. 17–31.

[31] M. Hada, K. Pichugin, and G. Sciaini. “Ultrafast structural dynamics with table top femtosecond hard X-ray and electron diffraction setups”. *European Physical Journal-Special Topics* 222.5 (2013), pp. 1093–1123.

[32] C. P. Ellington, C. vandenBerg, A. P. Willmott, and A. L. R. Thomas. “Leading-edge vortices in insect flight”. *Nature* 384.6610 (1996), pp. 626–630.

[33] C. Clanet, F. Hersen, and L. Bocquet. “Secrets of successful stone-skipping”. *Nature* 427.6969 (2004), pp. 29–29.

[34] C. Rischel et al. “Femtosecond time-resolved X-ray diffraction from laser-heated organic films”. *Nature* 390.6659 (1997), pp. 490–492.

[35] C. Rose-Petruck et al. “Picosecond-milliangstrom lattice dynamics measured by ultrafast X-ray diffraction”. *Nature* 398.6725 (1999), pp. 310–312.

[36] K. Sokolowski-Tinten et al. “Femtosecond X-ray measurement of coherent lattice vibrations near the Lindemann stability limit”. *Nature* 422.6929 (2003), pp. 287–289.

[37] P. Beaud et al. “Ultrafast Structural Phase Transition Driven by Photoinduced Melting of Charge and Orbital Order”. *Physical Review Letters* 103.15 (2009).

[38] T. Elsaesser and M. Woerner. “Photoinduced structural dynamics of polar solids studied by femtosecond X-ray diffraction”. *Acta Crystallographica Section A* 66 (2010), pp. 168–178.

[39] M. Harb et al. “Picosecond dynamics of laser-induced strain in graphite”. *Physical Review B* 84.4 (2011).

[40] S. L. Johnson et al. “Femtosecond Dynamics of the Collinear-to-Spiral Antiferromagnetic Phase Transition in CuO”. *Physical Review Letters* 108.3 (2012).

[41] G. Mourou and S. Williamson. “Picosecond Electron-Diffraction”. *Applied Physics Letters* 41.1 (1982), pp. 44–45.

[42] S. Williamson, G. Mourou, and J. C. M. Li. “Time-Resolved Laser-Induced Phase-Transformation in Aluminum”. *Physical Review Letters* 52.26 (1984), pp. 2364–2367.

[43] H. Ihee et al. “Direct imaging of transient molecular structures with ultrafast diffraction”. *Science* 291.5503 (2001), pp. 458–462.

[44] C. Y. Ruan et al. “Ultrafast electron crystallography: Transient structures of molecules, surfaces, and phase transitions”. *Proceedings of the National Academy of Sciences of the United States of America* 101.5 (2004), pp. 1123–1128.

[45] B. Krenzer et al. “Thermal boundary conductance in heterostructures studied by ultrafast electron diffraction”. *New Journal of Physics* 8 (2006).

[46] R. A. Murdick, R. K. Raman, Y. Murooka, and C. Y. Ruan. “Photovoltage dynamics of the hydroxylated Si(111) surface investigated by ultrafast electron diffraction”. *Physical Review B* 77.24 (2008).

[47] B. J. Siwick, J. R. Dwyer, R. E. Jordan, and R. J. D. Miller. “An atomic-level view of melting using femtosecond electron diffraction”. *Science* 302.5649 (2003), pp. 1382–1385.

[48] B. Barwick et al. “4D Imaging of Transient Structures and Morphologies in Ultrafast Electron Microscopy”. *Science* 322.5905 (2008), pp. 1227–1231.

[49] M. Harb et al. “Excitation of longitudinal and transverse coherent acoustic phonons in nanometer free-standing films of (001) Si”. *Physical Review B* 79.9 (2009).

[50] Sascha Schäfer, Wenxi Liang, and Ahmed H. Zewail. “Primary structural dynamics in graphite”. *New Journal of Physics* 13.6 (2011), p. 063030.

[51] H. Jean-Ruel et al. “Ring-Closing Reaction in Diarylethene Captured by Femtosecond Electron Crystallography”. *Journal of Physical Chemistry B* 117.49 (2013), pp. 15894–15902.

[52] T. R. T. Han et al. “Structural dynamics of two-dimensional charge-density waves in CeTe3 investigated by ultrafast electron crystallography”. *Physical Review B* 86.7 (2012).

[53] M. Gao et al. “Mapping molecular motions leading to charge delocalization with ultrabright electrons”. *Nature* 496.7445 (2013), pp. 343–346.

[54] A. H. Zewail. “Four-Dimensional Electron Microscopy”. *Science* 328.5975 (2010), pp. 187–193.

[55] R. Henderson. “The Potential and Limitations of Neutrons, Electrons and X-Rays for Atomic-Resolution Microscopy of Unstained Biological Molecules”. *Quarterly Reviews of Biophysics* 28.2 (1995), pp. 171–193.

[56] X. Zou, S. Hovmöller, and P. Oleynikov. *Electron Crystallography: Electron Microscopy and Electron Diffraction.* OUP Oxford, 2011.

[57] R. Singla et al. “Photoinduced melting of the orbital order in La0.5Sr1.5MnO4 measured with 4-fs laser pulses”. *Physical Review B* 88.7 (2013).

[58] C. Kittel. *Einführung in die Festkörperphysik.* Oldenbourg, 2006.

[59] Enrique J. Baran. “Mean Amplitudes of Vibration of the Halogen Molecules”. *Zeitschrift für Naturforschung A* 58.a (2003), pp. 36–38.

[60] A. R. T. Nugraha et al. “Excitonic effects on coherent phonon dynamics in single-wall carbon nanotubes”. *Physical Review B* 88.7 (2013), p. 075440.

[61] D.R. Lide. *CRC Handbook of Chemistry and Physics, 85th Edition.* Taylor & Francis, 2004.

[62] Merle E. Riley, Crawford J. MacCallum, and Frank Biggs. “Theoretical electron-atom elastic scattering cross sections: Selected elements, 1 keV to 256 keV”. *Atomic Data and Nuclear Data Tables* 15.5 (1975), pp. 443–476.

[63] D.B. Williams and C.B. Carter. *Transmission Electron Microscopy: A Textbook for Materials Science*. Springer, 2009.

[64] G. Sciaini and R. J. D. Miller. “Femtosecond electron diffraction: heralding the era of atomically resolved dynamics”. *Reports on Progress in Physics* 74.9 (2011).

[65] R. Karpicz et al. “Relaxation Pathways of Excited N-(Triphenylmethyl)salicylidenimine in Solutions”. *Journal of Physical Chemistry A* 115.10 (2011), pp. 1861–1868.

[66] S. Lochbrunner, K. Stock, and E. Riedle. “Direct observation of the nuclear motion during ultrafast intramolecular proton transfer”. *Journal of Molecular Structure* 700.1–3 (2004), pp. 13–18.

[67] M. Barbatti et al. “Ultrafast internal conversion pathway and mechanism in 2-(2 ’-hydroxyphenyl) benzothiazole: a case study for excited-state intramolecular proton transfer systems”. *Physical Chemistry Chemical Physics* 11.9 (2009), pp. 1406–1415.

[68] M. Hase, M. Katsuragawa, A. M. Constantinescu, and H. Petek. “Coherent phonon-induced optical modulation in semiconductors at terahertz frequencies”. *New Journal of Physics* 15 (2013).

[69] P. Baum and A. H. Zewail. “4D attosecond imaging with free electrons: Diffraction methods and potential applications”. *Chemical Physics* 366.1-3 (2009), pp. 2–8.

[70] F. Krausz and M. Ivanov. “Attosecond physics”. *Reviews of Modern Physics* 81.1 (2009), pp. 163–234.

[71] M. Ligges et al. “Observation of ultrafast lattice heating using time resolved electron diffraction”. *Applied Physics Letters* 94.10 (2009).

[72] Fabrizio Carbone, Peter Baum, Petra Rudolf, and Ahmed Zewail. “Structural Preablation Dynamics of Graphite Observed by Ultrafast Electron Crystallography”. *Physical Review Letters* 100.3 (2008).

[73] C. Y. Ruan et al. “The Development and Applications of Ultrafast Electron Nanocrystallography”. *Microscopy and Microanalysis* 15.4 (2009), pp. 323–337.

[74] W. E. King et al. “Ultrafast electron microscopy in materials science, biology, and chemistry”. *Journal of Applied Physics* 97.11 (2005).

[75] P. Kung, H. C. Lihn, H. Wiedemann, and D. Bocek. “Generation and Measurement of 50-Fs (Rms) Electron Pulses”. *Physical Review Letters* 73.7 (1994), pp. 967–970.

[76] S. Tokita et al. “Single-Shot Femtosecond Electron Diffraction with Laser-Accelerated Electrons: Experimental Demonstration of Electron Pulse Compression”. *Physical Review Letters* 105.21 (2010).

[77] A. Buck et al. “Real-time observation of laser-driven electron acceleration”. *Nature Physics* 7.7 (2011), pp. 543–548.

[78] J. B. Hastings et al. “Ultrafast time-resolved electron diffraction with megavolt electron beams”. *Applied Physics Letters* 89.18 (2006), pp. –.

[79] P. Musumeci et al. “Capturing ultrafast structural evolutions with a single pulse of MeV electrons: Radio frequency streak camera based electron diffraction”. *Journal of Applied Physics* 108.11 (2010), pp. –.

[80] Wenxi Liang, Sascha Schäfer, and Ahmed H. Zewail. “Ultrafast electron crystallography of heterogeneous structures: Gold-graphene bilayer and ligand-encapsulated nanogold on graphene”. *Chemical Physics Letters* 542 (2012), pp. 8–12.

[81] A. Janzen et al. “Ultrafast electron diffraction at surfaces after laser excitation”. *Surface Science* 600.18 (2006), pp. 4094–4098.

[82] M. Gao et al. “Full characterization of RF compressed femtosecond electron pulses using ponderomotive scattering”. *Optics Express* 20.11 (2012), pp. 12048–12058.

[83] A. Gahlmann, S. T. Park, and A. H. Zewail. “Ultrashort electron pulses for diffraction, crystallography and microscopy: theoretical and experimental resolutions”. *Physical Chemistry Chemical Physics* 10.20 (2008), pp. 2894–2909.

[84] A.H. Zewail. *4D Electron Microscopy: Imaging in Space and Time*. Imperial College Press, 2010.

[85] M. Aidelsburger, F. O. Kirchner, F. Krausz, and P. Baum. “Single-electron pulses for ultrafast diffraction”. *Proceedings of the National Academy of Sciences of the United States of America* 107.46 (2010), pp. 19714–19719.

[86] T. van Oudheusden et al. “Electron source concept for single-shot sub-100 fs electron diffraction in the 100 keV range”. *Journal of Applied Physics* 102.9 (2007).

[87] W. J. Engelen et al. “High-coherence electron bunches produced by femtosecond photoionization”. *Nature Communications* 4 (2013).

[88] W. J. Engelen et al. “Effective temperature of an ultracold electron source based on near-threshold photoionization”. *Ultramicroscopy* 136 (2014), pp. 73–80.

[89] A. J. McCulloch et al. “Arbitrarily shaped high-coherence electron bunches from cold atoms”. *Nat Phys* 7.10 (2011), pp. 785–788.

[90] B. Cho, T. Ichimura, R. Shimizu, and C. Oshima. “Quantitative Evaluation of Spatial Coherence of the Electron Beam from Low Temperature Field Emitters”. *Physical Review Letters* 92.24 (2004), p. 246103.

[91] B. Cho and C. Oshima. “Electron Beam Coherency Determined from Interferograms of Carbon Nanotubes”. *Bulletin of the Korean Chemical Society* 34.3 (2013), pp. 892–898.

[92] D. Ehberger et al. “Highly coherent electron beam from a laser-triggered tungsten needle tip”. *ArXiv e-prints* 1412.4584 (2014).

[93] J. Hoffrogge et al. “Tip-based source of femtosecond electron pulses at 30 keV”. *Journal of Applied Physics* 115.9 (2014).

[94] Peter Hommelhoff, Catherine Kealhofer, and Mark A. Kasevich. “Ultrafast Electron Pulses from a Tungsten Tip Triggered by Low-Power Femtosecond Laser Pulses”. *Physical Review Letters* 97.24 (2006), p. 247402.

[95] C. Kealhofer, S. M. Foreman, S. Gerlich, and M. A. Kasevich. “Ultrafast laser-triggered emission from hafnium carbide tips”. *Physical Review B* 86.3 (2012).

[96] Michael Kruger, Markus Schenk, and Peter Hommelhoff. “Attosecond control of electrons emitted from a nanoscale metal tip”. *Nature* 475.7354 (2011), pp. 78–81.

[97] E. A. Peralta et al. “Demonstration of electron acceleration in a laser-driven dielectric microstructure”. *Nature* 503.7474 (2013), pp. 91–94.

[98] John Breuer and Peter Hommelhoff. “Laser-Based Acceleration of Nonrelativistic Electrons at a Dielectric Structure”. *Physical Review Letters* 111.13 (2013), p. 134803.

[99] J. C. Williamson and A. H. Zewail. “Ultrafast Electron-Diffraction - Velocity Mismatch and Temporal Resolution in Crossed-Beam Experiments”. *Chemical Physics Letters* 209.1-2 (1993), pp. 10–16.

[100] D. S. Yang and A. H. Zewail. “Ordered water structure at hydrophobic graphite interfaces observed by 4D, ultrafast electron crystallography”. *Proc Natl Acad Sci U S A* 106.11 (2009), pp. 4122–6.

[101] M. Gao, Y. Jiang, G. H. Kassier, and R. J. D. Miller. “Single shot time stamping of ultrabright radio frequency compressed electron pulses”. *Applied Physics Letters* 103.3 (2013).

[102] D. Polli et al. “Effective temporal resolution in pump-probe spectroscopy with strongly chirped pulses”. *Physical Review A* 82.5 (2010).

[103] P. Baum. “On the physics of ultrashort single-electron pulses for time-resolved microscopy and diffraction”. *Chemical Physics* 423 (2013), pp. 55–61.

[104] E. Goulielmakis et al. “Attosecond control and measurement: Lightwave electronics”. *Science* 317.5839 (2007), pp. 769–775.

[105] Y. P. Deng et al. “Carrier-envelope-phase-stable, 1.2 mJ, 1.5 cycle laser pulses at 2.1 mu m”. *Optics Letters* 37.23 (2012), pp. 4973–4975.

[106] M. Schultze et al. “Delay in Photoemission”. *Science* 328.5986 (2010), pp. 1658–1662.

[107] A. L. Cavalieri et al. “Attosecond spectroscopy in condensed matter”. *Nature* 449.7165 (2007), pp. 1029–1032.

[108] H. Puff. “Zur Theorie der Sekundärelektronenemission Der Transportprozeß. I. Formulierung des Problems”. *physica status solidi (b)* 4.1 (1964), pp. 125–138.

[109] C. N. Berglund and W. E. Spicer. “Photoemission Studies of Copper and Silver: Theory”. *Physical Review* 136.4A (1964), A1030–A1044.

[110] D. H. Dowell and J. F. Schmerge. “Quantum efficiency and thermal emittance of metal photocathodes (vol 12, 074201, 2009)”. *Physical Review Special Topics-Accelerators and Beams* 12.11 (2009).

[111] A. Zangwill. *Physics at Surfaces*. Cambridge University Press, 1988.

[112] J. L. Wu, L. J. Guo, and Q. D. Wu. “Response-Time of Photoemission of Ultrafine Particle Thin-Film”. *Acta Physica Sinica-Overseas Edition* 3.7 (1994), pp. 528–538.

[113] O. J. Luiten et al. “How to realize uniform three-dimensional ellipsoidal electron bunches”. *Physical Review Letters* 93.9 (2004).

[114] J. M. Cowley. *Diffraction physics*. Amsterdam : New York: North-Holland Pub. Co. ; American Elsevier, 1975.

[115] D. K. Davies. “Initiation of Electrical Breakdown in Vacuum - Review”. *Journal of Vacuum Science & Technology* 10.1 (1973), pp. 115–121.

[116] Clemens Weninger. “Temporal and Spatial Focusing of Femtosecond Single-Electron Pulses”. Master’s thesis, LMU München. 2013.

[117] C. Weninger and P. Baum. “Temporal distortions in magnetic lenses”. *Ultramicroscopy* 113 (2012), pp. 145–151.

[118] D. Kreier and P. Baum. “Avoiding temporal distortions in tilted pulses”. *Optics Letters* 37.12 (2012), pp. 2373–2375.

[119] P. Baum and A. H. Zewail. “Breaking resolution limits in ultrafast electron diffraction and microscopy”. *Proceedings of the National Academy of Sciences of the United States of America* 103.44 (2006), pp. 16105–16110.

[120] T. van Oudheusden et al. “Compression of Subrelativistic Space-Charge-Dominated Electron Bunches for Single-Shot Femtosecond Electron Diffraction”. *Physical Review Letters* 105.26 (2010).

[121] G. H. Kassier et al. “Photo-triggered pulsed cavity compressor for bright electron bunches in ultrafast electron diffraction”. *Applied Physics B-Lasers and Optics* 109.2 (2012), pp. 249–257.

[122] B. J. Siwick, J. R. Dwyer, R. E. Jordan, and R. J. D. Miller. “Ultrafast electron optics: Propagation dynamics of femtosecond electron packets”. *Journal of Applied Physics* 92.3 (2002), pp. 1643–1648.

[123] Kreier Daniel, Sabonis Deividas, and Baum Peter. “Alignment of magnetic solenoid lenses for minimizing temporal distortions”. *Journal of Optics* 16.7 (2014), p. 075201.

[124] P. Musumeci et al. “Experimental Generation and Characterization of Uniformly Filled Ellipsoidal Electron-Beam Distributions”. *Physical Review Letters* 100.24 (2008), p. 244801.

[125] S. Rimjaem et al. “Femtosecond electron bunches from an RF-gun”. *Nuclear Instruments & Methods in Physics Research Section a-Accelerators Spectrometers Detectors and Associated Equipment* 533.3 (2004), pp. 258–269.

[126] G. H. Kassier et al. "Achromatic reflectron compressor design for bright pulses in femtosecond electron diffraction". *Journal of Applied Physics* 105.11 (2009).

[127] Y. H. Wang and N. Gedik. "Electron Pulse Compression With a Practical Reflectron Design for Ultrafast Electron Diffraction". *Ieee Journal of Selected Topics in Quantum Electronics* 18.1 (2012), pp. 140–147.

[128] P. Hansen, C. Baumgarten, H. Batelaan, and M. Centurion. "Dispersion compensation for attosecond electron pulses". *Applied Physics Letters* 101.8 (2012).

[129] R. Egerton. *Electron Energy-Loss Spectroscopy in the Electron Microscope.* Springer, 2011.

[130] L. Veisz et al. "Hybrid dc-ac electron gun for fs-electron pulse generation". *New Journal of Physics* 9 (2007).

[131] A. Gliserin, A. Apolonski, F. Krausz, and P. Baum. "Compression of single-electron pulses with a microwave cavity". *New Journal of Physics* 14 (2012).

[132] P. L. E. M. Pasmans et al. "Microwave TM010 cavities as versatile 4D electron optical elements". *Ultramicroscopy* 127 (2013), pp. 19–24.

[133] G. F. Mancini et al. "Design and implementation of a flexible beamline for fs electron diffraction experiments". *Nuclear Instruments & Methods in Physics Research Section a-Accelerators Spectrometers Detectors and Associated Equipment* 691 (2012), pp. 113–122.

[134] R. P. Chatelain, V. R. Morrison, C. Godbout, and B. J. Siwick. "Ultrafast electron diffraction with radio-frequency compressed electron pulses". *Applied Physics Letters* 101.8 (2012).

[135] H. C. Shao and A. F. Starace. "Detecting Electron Motion in Atoms and Molecules". *Physical Review Letters* 105.26 (2010).

[136] G. J. H. Brussaard et al. "Direct measurement of synchronization between femtosecond laser pulses and a 3 GHz radio frequency electric field inside a resonant cavity". *Applied Physics Letters* 103.14 (2013).

[137] K. Jung and J. Kim. "Subfemtosecond synchronization of microwave oscillators with mode-locked Er-fiber lasers". *Optics Letters* 37.14 (2012), pp. 2958–2960.

[138] Edgar Vredenbregt and Jom Luiten. "Electron diffraction: Cool beams in great shape". *Nat Phys* 7.10 (2011), pp. 747–748.

[139] V. A. Lobastov, R. Srinivasan, and A. H. Zewail. "Four-dimensional ultrafast electron microscopy". *Proceedings of the National Academy of Sciences of the United States of America* 102.20 (2005), pp. 7069–7073.

[140] B. Barwick, D. J. Flannigan, and A. H. Zewail. "Photon-induced near-field electron microscopy". *Nature* 462.7275 (2009), pp. 902–906.

[141] A. Gliserin. "Towards attosecond 4D imaging of atomic- scale dynamics by single-electron diffraction". Dissertation, LMU München. 2014.

[142] Friedrich Kirchner. "Ultrashort and coherent single-electron pulses for diffraction at ultimate resolutions". Dissertation, LMU München. 2013.

[143] F. Carbone, P. Musumeci, O. J. Luiten, and C. Hebert. "A perspective on novel sources of ultrashort electron and X-ray pulses". *Chemical Physics* 392.1 (2012), pp. 1–9.

[144] S. B. van der Geer, M. J. de Loos, E. J. D. Vredenbregt, and O. J. Luiten. "Ultracold Electron Source for Single-Shot, Ultrafast Electron Diffraction". *Microscopy and Microanalysis* 15.4 (2009), pp. 282–289.

[145] S. Gosavi et al. "Practical gold thin-film photocathodes for advanced electron beam lithography". *19th Annual Symposium on Photomask Technology, Pts 1 and 2* 3873 (1999), pp. 501–512.

[146] John H. Moore, Christopher C. Davis, Michael A. Coplan, and Sandra C. Greer. *Building Scientific Apparatus*. Cambridge University Press, 2009.

[147] S. Schnur and A. Gross. "Properties of metal-water interfaces studied from first principles". *New Journal of Physics* 11 (2009).

[148] Francesco Musumeci and Gerald H. Pollack. "Influence of water on the work function of certain metals". *Chemical Physics Letters* 536.0 (2012), pp. 65–67.

[149] W. Y. Lin, H. X. Han, and H. Frei. "CO_2 splitting by H_2O to CO and O_2 under UV light in TiMCM-41 silicate sieve". *Journal of Physical Chemistry B* 108.47 (2004), pp. 18269–18273.

[150] S. Gosavi et al. "Stability improvement at high emission densities for gold thin film photocathodes used in advanced electron beam lithography". *Journal of Vacuum Science & Technology B* 19.6 (2001), pp. 2591–2597.

[151] Aleksandar D. Rakić, Aleksandra B. Djurišić, Jovan M. Elazar, and Marian L. Majewski. "Optical properties of metallic films for vertical-cavity optoelectronic devices". *Applied Optics* 37.22 (1998), pp. 5271–5283.

[152] Theresa Urban. "Charakterisierung und Optimierung der Detektion von Einzelelektronen für die ultraschnelle Elektronenbeugung". Bachelor's thesis, TU München. 2014.

[153] S. U. Ay, M. Lesser, and E. R. Fossum. "CMOS Active Pixel Sensor (APS) imager for scientific applications". *Survey and Other Telescope Technologies and Discoveries* 4836 (2002), pp. 271–278.

[154] H. Tian. "Noise analysis in CMOS image sensors". PhD Thesis. 2000.

[155] H. Tian, B. Fowler, and A. F. Gamal. "Analysis of temporal noise in CMOS photodiode active pixel sensor". *Ieee Journal of Solid-State Circuits* 36.1 (2001), pp. 92–101.

[156] Alexander André. "Sample preparation and optimal excitation conditions for femtosecond single-electron diffraction". Master's thesis, LMU München. 2013.

[157] D. S. Acker et al. “7,7,8,8-Tetracyanoquinodimethane and its electrically conducting anion-radical derivatives”. *Journal of the American Chemical Society* 82.24 (1960), pp. 6408–6409.

[158] D. B. Tanner, C. S. Jacobsen, A. A. Bright, and A. J. Heeger. “Infrared studies of the energy gap and electron-phonon interaction in potassium-tetracyanoquinodimethane (K-TCNQ)”. *Physical Review B* 16.8 (1977), pp. 3283–3290.

[159] S. Tanuma, C. J. Powell, and D. R. Penn. “Calculations of electron inelastic mean free paths. IX. Data for 41 elemental solids over the 50 eV to 30 keV range”. *Surface and Interface Analysis* 43.3 (2011), pp. 689–713.

[160] D.M. Mattox. *Handbook of Physical Vapor Deposition (PVD) Processing*. Elsevier Science, 2010.

[161] H.O. Pierson. *Handbook of Chemical Vapor Deposition, 2nd Edition: Principles, Technology and Applications*. Elsevier Science, 1999.

[162] G.H. Michler and W. Lebek. *Ultramikrotomie in der Materialforschung*. Hanser, 2004.

[163] A. Lewanowicz, A. Olszowski, P. Dziekonski, and J. Leszczynski. “Spectroscopic characteristics of the micro-environmentally induced H-bond transformation in anil-type species: experimental and theoretical study”. *Journal of Molecular Modeling* 11.4-5 (2005), pp. 398–406.

[164] Marina Hoheneder. “Spektroskopie ultraschneller Protonenübergänge in molekularen Nanokristallen”. Bachelor’s thesis, TU München.

[165] K. S. Novoselov et al. “Electric Field Effect in Atomically Thin Carbon Films”. *Science* 306.5696 (2004), pp. 666–669.

[166] Friedrich O. Kirchner, Stefan Lahme, Eberhard Riedle, and Peter Baum. “All-reflective UV-VIS-NIR transmission and fluorescence spectrometer for Œºm-sized samples”. *AIP Advances* 4.7 (2014), pp. –.

[167] R. J. Dwayne Miller. “Femtosecond Crystallography with Ultrabright Electrons and X-rays: Capturing Chemistry in Action”. *Science* 343.6175 (2014), pp. 1108–1116.

[168] M. Rini et al. “Control of the electronic phase of a manganite by mode-selective vibrational excitation”. *Nature* 449.7158 (2007), pp. 72–74.

[169] T. Kampfrath, K. Tanaka, and K. A. Nelson. “Resonant and nonresonant control over matter and light by intense terahertz transients”. *Nature Photonics* 7.9 (2013), pp. 680–690.

[170] M. Forst et al. “Nonlinear phononics as an ultrafast route to lattice control”. *Nature Physics* 7.11 (2011), pp. 854–856.

[171] M. Scheuch et al. “Temperature dependence of ultrafast phonon dynamics in graphite”. *Applied Physics Letters* 99.21 (2011), p. 211908.

[172] Markus Breusing, Claus Ropers, and Thomas Elsaesser. “Ultrafast Carrier Dynamics in Graphite”. *Physical Review Letters* 102.8 (2009).

[173] H. S. Park et al. “4D ultrafast electron microscopy: Imaging of atomic motions, acoustic resonances, and moire fringe dynamics”. *Ultramicroscopy* 110.1 (2009), pp. 7–19.

[174] W. X. Liang, G. M. Vanacore, and A. H. Zewail. “Observing (non)linear lattice dynamics in graphite by ultrafast Kikuchi diffraction”. *Proceedings of the National Academy of Sciences of the United States of America* 111.15 (2014), pp. 5491–5496.

[175] J. Maultzsch et al. “Phonon Dispersion in Graphite”. *Physical Review Letters* 92.7 (2004), p. 075501.

[176] Tobias Kampfrath et al. “Strongly Coupled Optical Phonons in the Ultrafast Dynamics of the Electronic Energy and Current Relaxation in Graphite”. *Physical Review Letters* 95.18 (2005).

[177] R. W. Newson, J. Dean, B. Schmidt, and H. M. van Driel. “Ultrafast carrier kinetics in exfoliated graphene and thin graphite films”. *Optics Express* 17.4 (2009), pp. 2326–2333.

[178] I. Chatzakis et al. “Temperature dependence of the anharmonic decay of optical phonons in carbon nanotubes and graphite”. *Physical Review B* 83.20 (2011).

[179] Kwangu Kang, Daner Abdula, David G. Cahill, and Moonsub Shim. “Lifetimes of optical phonons in graphene and graphite by time-resolved incoherent anti-Stokes Raman scattering”. *Physical Review B* 81.16 (2010).

[180] R. K. Raman et al. “Direct observation of optically induced transient structures in graphite using ultrafast electron crystallography”. *Physical Review Letters* 101.7 (2008).

[181] Aleksandra B. Djurišić and E. Herbert Li. “Optical properties of graphite”. *Journal of Applied Physics* 85.10 (1999), p. 7404.

[182] Igor S. Grigoriev and Evgenii Z. Meilikhov. *Handbook of Physical Quantities*. Taylor & Francis, 1997.

[183] D. D. L. Chung. “Review graphite”. *Journal of Materials Science* 37.8 (2002), pp. 1475–1489.

[184] P.B. Hirsch and A. Howie. *Electron Microscopy of Thin Crystals*. Butterworths, 1965.

[185] L. Tang and D. E. Laughlin. “Electron diffraction patterns of fibrous and lamellar textured polycrystalline thin films .1. Theory”. *Journal of Applied Crystallography* 29 (1996), pp. 411–418.

[186] L. Tang, Y. C. Feng, L. L. Lee, and D. E. Laughlin. “Electron diffraction patterns of fibrous and lamellar textured polycrystalline thin films .2. Applications”. *Journal of Applied Crystallography* 29 (1996), pp. 419–426.

[187] R. K. Raman, Z. Tao, T. R. Han, and C. Y. Ruan. “Ultrafast imaging of photoelectron packets generated from graphite surface”. *Applied Physics Letters* 95.18 (2009).

[188] E.D. Palik. *Handbook of Optical Constants of Solids*. Academic Press, 1991.

[189] D. K. L. Tsang, B. J. Marsden, S. L. Fok, and G. Hall. “Graphite thermal expansion relationship for different temperature ranges”. *Carbon* 43.14 (2005), pp. 2902–2906.

[190] H. Park et al. “Optical control of coherent lattice motions probed by femtosecond electron diffraction”. *Journal of Physical Chemistry B* 109.29 (2005), pp. 13854–13856.

[191] H. Park et al. “Mechanism of coherent acoustic phonon generation under nonequilibrium conditions”. *Physical Review B* 72.10 (2005).

[192] Alexey Bosak et al. “Elasticity of single-crystalline graphite: Inelastic x-ray scattering study”. *Physical Review B* 75.15 (2007).

[193] Haihua Liu, Oh-Hoon Kwon, Jau Tang, and Ahmed H. Zewail. “4D Imaging and Diffraction Dynamics of Single-Particle Phase Transition in Heterogeneous Ensembles”. *Nano Letters* 14.2 (2014), pp. 946–954.

[194] N. Singh. “Two-Temperature Model of Nonequilibrium Electron Relaxation: A Review”. *International Journal of Modern Physics B* 24.9 (2010), pp. 1141–1158.

[195] L. M. Peng. “Electron atomic scattering factors and scattering potentials of crystals”. *Micron* 30.6 (1999), pp. 625–648.

[196] D.G. Duffy. *Green’s Functions with Applications*. Taylor & Francis, 2001.

[197] A. Gliserin, M. Walbran, and P. Baum. “Passive optical enhancement of laser-microwave synchronization”. *Applied Physics Letters* 103.3 (2013).

Acknowledgements

This work would not have been possible without the support of numerous people. First off all, I want to thank Prof. Dr. Ferenc Krausz for giving me the opportunity to work in his research group. Over the years I have benefited a lot from the remarkable accumulation of knowledge provided by Prof. Krausz and the members of his team. It was a pleasure and inspiring to work with such a group of motivated and talented people. I also would like to thank Prof. Peter Hommelhoff for kindly offering to review my thesis. I would like to thank my supervisor, Dr. Peter Baum, for his kind and competent supervision and his careful proof-reading of this manuscript, including many ideas for improvement. His visionary perspective combined with his broad knowledge of various fields of physics were a great help and a perpetual motivation to me at the same time. His unshakable belief in the feasibility of single-electron diffraction made me look beyond my own nose and stay the course. Last but not least, I want to thank him for his trust in my supervision of Bachelor and Master students, giving me the chance to develop my teaching and leadership skills.

My thanks also go to all the members of the UED group for the warm and pleasant working atmosphere as well as scientific support. In particular, I would like to thank Friedrich Kirchner, who introduced me to the first generation experimental setup and the laser system, Alexander Gliserin for endless LabVIEW support beyond the CLAD level and my students Alexander André, Marina Hoheneder and Theresa Urban for their great work in the lab which provided many pieces of the puzzle. Alex's chemical knowledge and his support in facing lab drudgery with a little insanity was highly appreciated.

Many thanks also go to Rolf Oehm and his team at the mechanical workshop. His thoughtful design advice and expert realization of custom parts for the experiment were highly appreciated. Siegfried Herbst and Johann Krapfl and his team at the electrical workshop were very helpful with electronics design. I wish to thank Dagmar Frischke for frequent support with sample preparation. Her uncomplicated and fast help was essential for our experiments. I would like to thank Katharina Adler for her support with MAP Zusatzbudget proposals.

I am deeply indebted to Dr. Catherine Kealhofer for her help with data analysis and valuable advice on the manuscript resulting in numerous improvements. In the short time we shared an office I benefited a lot from her knowledge and we shared many fun and intense physics discussions. I am very grateful to Martin Reininghaus for his continuous support in work and non-work related discussions about the most "schuselig" issues. Many thanks go to Dr. Marc Leßmann for his generous support with FEM simulations and genetic algorithms. Thanks are due to Dr. Marianne Hanzlik for countless TEM measurements, Simon Holzberger for support with bright-field microscopy, Olga Razskazovskaya for profilometry measurements and coatings, Lisa Koll for SEM and EDX measurements and Dr. Saskia Mimietz-Oeckler for ultramicrotomy instruction. I wish to thank Dr. Rudolf Diesel from ScienceMedia for kindly providing permission to reprint some of his amazing high-speed photography footage.

I am very grateful to all my friends for supporting me and my work with their nice and warm friendship, including Marisa (Pinky goes Caipirinha), Maylin and Mark (Abenteuer mit dem blauen Ross, Freundschaft), Christian, Christoph, Florian, Sindy, Sebastian (MOF meets UED) and Christopher. It is easy to face challenges having people like you around that I can lean on no matter what happens. I'd like to thank Miren and my former flatmates for lifting my spirits and putting up with me during my ups and downs.

Last but most important, thank you to my parents for their continuous support, love, and faith in me. You encouraged me to explore the world but you never stopped giving me a warm home to return to. Danke!